Interacting Rydberg atoms:

Coherent control at Förster resonances and polar homonuclear molecules

Von der Fakultät Mathematik und Physik der
Universität Stuttgart zur Erlangung der Würde eines
Doktors der Naturwissenschaften (Dr. rer. nat.)
genehmigte Abhandlung

vorgelegt von

Johannes Maximilian Nipper
aus Gießen

Hauptberichter:	Prof. Dr. Tilman Pfau
Mitberichter:	Prof. Dr. Jörg Wrachtrup
Prüfungsvorsitzender:	Prof. Dr. Günther Wunner
Tag der mündlichen Prüfung:	26.07.2012

5. Physikalisches Institut
Universität Stuttgart

2012

Abstract

Interactions between single atoms are fundamental to physics and to control them is an ultimate goal. The exaggerated properties of Rydberg atoms offer to met the technical challenges to isolate and control single interaction channels in ultracold gases. Here, I present experiments on two subjects related to interactions of Rydberg atoms in dense ultracold clouds. One subject concerns coherence in strongly interacting ensembles of atoms, where the interaction between Rydberg atoms is induced via Stark-tuned Förster resonances. Pulsed experiments, following the idea of Ramsey experiments, are used for high resolution spectroscopy of the Förster defect and phase sensitive detection. Coherent oscillations between pair states and an interaction-induced phase shift of Rydberg atoms are measured. These experiments are accompanied by calculations of the interaction strength and by simulations using the concept of a pair state interferometer. The simulations nicely reproduce the experimental findings and support the observation that the ensemble of atoms in the presence of interactions can be described and controlled coherently.
The second subject of this thesis is the measurement of a permanent dipole moment in a homonuclear diatomic molecule that arises by the interaction between a Rydberg atom and a ground state atom. Usually parity symmetry prohibits a permanent dipole moment in diatomic molecules, but here the strong asymmetry between the constituents of the ultralong-range Rydberg molecule allows breaking parity symmetry. These molecules consist of one ground state atom bound inside the Rydberg electron wavefunction of a highly excited atom. Calculations predict dipole moments on the order of 1 Debye. Experimental proof is reported on the measurement of a linear Stark effect of these molecules, in excellent agreement with the calculations.

Refereed papers

During this dissertation I participated in the preparation of the following papers:

- J. Nipper, J.B. Balewski, A.T. Krupp, S. Hofferberth, R. Löw and T. Pfau, *Atomic Pair-State Interferometer: Controlling and Measuring an Interaction-Induced Phase Shift in Rydberg-Atom Pairs,* Phys. Rev. X, **2**, 031011 (2012)

- J. Nipper, J.B. Balewski, A. Krupp, B. Butscher, R. Löw and T. Pfau, *Highly Resolved Measurements of Stark-Tuned Förster Resonances between Rydberg Atoms,* Phys. Rev. Lett., **108**, 113001 (2012)

- R. Löw, H. Weimer, J. Nipper, J.B. Balewski, B. Butscher, H.P. Büchler and T. Pfau, *An experimental and theoretical guide to strongly interacting Rydberg gases,* J. Phys. B: At. Mol. Opt. Phys., **45**, 113001 (2012)

- W. Li, T. Pohl, J.M. Rost, S.T. Rittenhouse, H.R. Sadeghpour, J. Nipper, B. Butscher, J.B. Balewski, V. Bendkowsky, R. Low and T. Pfau, *A Homonuclear Molecule with a Permanent Electric Dipole Moment,* Science, **334**, 1110-1114 (2011)

- B. Butscher, V. Bendkowsky, J. Nipper, J.B. Balewski, L. Kukota, R. Löw, T. Pfau, W. Li, T. Pohl and J.M. Rost, *Lifetimes of ultralong-range Rydberg molecules in vibrational ground and excited states,* Journal of Physics B: Atomic, Molecular and Optical Physics, **44**, 184004 (2011)

- B. Butscher, J. Nipper, J.B. Balewski, L. Kukota, V. Bendkowsky, R. Löw and T. Pfau, *Atom-molecule coherence for ultralong-range Rydberg dimers*, Nature Physics, **6**, 970-974 (2010)

- V. Bendkowsky, B. Butscher, J. Nipper, J. Balewski, J. Shaffer, R. Löw, T. Pfau, W. Li, J. Stanojevic, T. Pohl and J. Rost, *Rydberg Trimers and Excited Dimers Bound by Internal Quantum Reflection,* Physical Review Letters, *105*, 163201 (2010)

- V. Bendkowsky, B. Butscher, J. Nipper, J.P. Shaffer, R. Löw and T. Pfau, *Observation of ultralong-range Rydberg molecules,* Nature, *458*, 1005-1008 (2009)

Table of Contents

Zusammenfassung

Ultrakalte Physik stellt zur Zeit eines der heißesten Forschungsgebiete der Physik dar. Dabei bedeutet 'ultrakalt' Temperaturen nahe dem absoluten Temperatur-Nullpunkt, unter 1 mK, bei denen quantenmechanische Effekte auftreten. Auch wenn diese Temperaturen weit von alltäglichen Bedingungen entfernt sind, können viele offene Fragen der Physik unter diesen Umständen untersucht werden und sogar einige Anwendungen aus der ultrakalten Physik entstehen. Die fundamentale Idee ist, dass Atome sehr gut verstanden und kontrolliert werden können, wenn sie sich an einer bekannten Position befinden und aufgrund ihrer niedrigen Temperatur praktisch nicht bewegen.
Dabei ist die Kombination dieser ultrakalten Atome mit hochangeregten Atomen, sogenannten Rydbergatomen, sehr vielversprechend, weil Rydbergatome und ultrakalte Grundzustandsatome in vieler Hinsicht Gegensätze darstellen. Rydbergatome sind mehrere Größenordnungen größer als Grundzustandsatome und wechselwirken stark, wohingegen ultrakalte Atome im Grundzustand kleine Wechselwirkungen zeigen. Werden diese Extrema kombiniert bieten sich interessante Möglichkeiten, sowohl für neue Physik als auch für neue Anwendungen. Die meisten Experimente und theoretischen Vorschläge der ultrakalten Rydbergphysik basieren auf diesen Gegensätzen.
In dieser Arbeit stelle ich zwei Arten von Experimenten vor. Zum einen befasse ich mich mit Experimenten, bei denen Wechselwirkungen zwischen Rydbergatomen durch Förster-Resonanzen induziert werden und die Stärke durch externe elektrische Felder beeinflusst wird. Die starke Wechselwirkung zwischen den Rydbergatomen, verglichen mit der Wechselwirkung zwischen den Grundzustandsatomen, ermöglicht es, einzelne Wechselwirkungskanäle zu isolieren und kohärent zu kontrollieren. Zum anderen stelle ich Experimente vor, die ein permanentes elektrisches Dipolmoment in einem homonuklearen Rydbergmolekül nachweisen. Dieses Dipolmoment bildet sich aufgrund der Größenunterschiede zwischen Rydberg- und Grundzustandsatomen. Die physikalischen Hintergründe der Experimente sind sehr verschieden, trotzdem basieren beide auf Rydberganregungen in ultrakalten Atomen und zeigen damit die Vielseitigkeit der ultrakalten Physik.
Seit der Erfindung der Laserkühlung und des Fangens von Atomen mit Laserlicht [1], für die Steven Chu, Claude Cohen-Tannoudji und William D. Phillips 1997 mit dem Nobelpreis ausgezeichnet wurden [2], hat sich die ultrakalte Physik rasant entwickelt.

Laserkühlung ermöglicht es, gasförmige Atome im Vakuum zu kühlen, ohne dass die Atome zu einer Flüssigkeit oder einem Festkörper kondensieren. Dabei werden sie auf so geringe Geschwindigkeiten abgebremst, dass quantenmechanische Effekte aufgrund der geringen thermischen Energie autreten.
Aufgrund der guten Kontrolle von einzelnen Atomen oder von Atomwolken bei diesen Temperaturen können verschiedene Themen untersucht werden. Dies führt zu besserem Verständnis und besserer Kontrolle bekannter Bereiche der Physik als auch zu neuen Bereichen, die bisher nicht realisiert werden konnten oder sogar völlig unbekannt waren. Bisher ist in Hinsicht auf neue Bereiche der Physik die möglicherweise größte Errungenschaft der ultrakalten Physik die Erzeugung eines Bose-Einstein Kondensats, für das 2001 Eric A. Cornell, Wolfgang Ketterle und Carl E. Wieman mit dem Nobelpreis geehrt wurden [3].
Neben diesen Aspekten der Grundlagenforschung bietet die ultrakalte Physik auch vielfältige Anwendungsmöglicheiten. Eine bekannte Anwendung sind Atomuhren [4, 5], die seit vielen Jahren den Zeitstandart festlegen und auf lasergekühlten Atomen basieren. Ebenso können hochpräzise Messungen mit ultrakalten Atomen gemacht werden, sogenannte Quantenmetrologie [6]. Vielversprechend sind zum Beispiel hochpräzise Messungen der Gravitation [7]. Ein weiteres mögliches Anwendungsfeld, bereits 1982 von Richard Feynman theoretisch begründet [8], ist Quanteninformationsverarbeitung und Quantensimulation von komplexen quantenmechanischen Strukturen aus der Festkörperphysik oder Biophysik [9, 10]. Auch wenn noch große Schritte zu einer Anwendung außerhalb der Grundlagenforschung fehlen, so sind die ersten Ansätze vorhanden. Neueste aufsehenerregende experimentelle Ergebnisse sind Simulationen einer Ising-Kette in einem optischen Gitter als Modellsystem für ein magnetisches System [11].
In Quantensimulatoren wird das quantenmechanische System als quantenmechanisches Modellsystem, beispielsweise mithilfe von ultrakalten Atomen, Stück für Stück nachgebaut und die Eigenschaften des Modells bestimmt. Ein wichtiger Bestandteil sind kontrollierbare, langreichweitige Wechselwirkungen zwischen den Atomen, um das Modellsystem zu erzeugen, das dem realen System entspricht. Neben polaren Molekülen [12] sind hierzu auch Rydbergatome vorgeschlagen worden [10, 13].
In Rydbergatomen ist ein Elektron in einem hochangeregten Zustand, somit ist die Ausdehnung der Elektronenwellenfunktion sehr groß. Dadurch werden Rydbergatome einfach polarisiert und zeigen starke Van-der-Waals-Wechselwirkungen [14]. Die erste Beobachtung dieser Rydberg-Rydberg Wechselwirkung wurde bereits 1981 in einem Atomstrahlexperiment gemacht [15]. Unter bestimmten Bedingungen können Paarzustände, die aus den Energieniveaus zweier Atome bestehen, in externen Feldern resonant werden. An diesen sogenannten Förster-Resonanzen kann die Wechselwirkung einen dipolaren, langreichweitigen Charakter zeigen und die Stärke der Wechselwirkung kann über das externe Feld als Kontrollparameter variiert werden. Förster-Resonanzen

von Rydbergatomen sind das erste Mal in Atomstrahlexperimenten in Tom Gallaghers Gruppe beobachtet worden. Dabei wurde 1981 ein statisches elektrisches Feld genutzt [16], um die Resonanz zu erzeugen, und 1982 ein Mikrowellenfeld [17]. Insbesondere die Möglichkeit, die Stärke der Wechselwirkung durch das externe Feld zu kontrollieren, macht Förster-Resonanzen zwischen Rydbergatomen interessant. Sie wurden deshalb in vielen Gruppen studiert [18, 19, 20, 21, 22, 23, 24, 25].
Rydberganregungen ultrakalter Atome bieten die Möglichkeit kohärenter Kontrolle der Rydberganregung und der Wechselwirkungen zwischen den Atomen. Einzeln wurden sowohl die kohärente Rydberganregung in mehreren Experimenten nachgewiesen [26, 27] als auch die Kohärenz in der Kopplung zwischen Rydbergatomen an einer Förster-Resonanz [28]. Kohärente Kontrolle ist eine fundamentale Voraussetzung für Quanteninformation und Quantensimulation. Neben der Simulation von Gleichgewichtszuständen kann auch die Zeitentwicklung eines stark korrelierten Vielteilchensystems beobachtet werden. Solche dynamischen Quanteneffekte sind beispielsweise eine quantenmechanische Zufallsbewegung [29] oder auch kohärente Energieübertragung [18]. Diese Energieübertragung ist insbesondere in der Biophysik interessant, bei der sie in der Photosynthese und Photolumineszenz auftritt. Dieser sogenannte Förster-Resonanzenergietransport (FRET) wurde zum ersten Mal 1948 von Theodor Förster [30] als nicht-kohärenter, strahlungsfreier Energietransport zwischen zwei Molekülen beschrieben, deren angeregte Zustände resonant sind. Die bereits angesprochenen Förster-Resonanzen zwischen Rydbergatomen stellen ebenso eine resonante, strahlungsfreie Kopplung zweier Übergangsdipole dar [31] und sind deshalb nach dem FRET-Prozess benannt.
Entgegen der ursprünglichen Beschreibung als nicht-kohärenter Energietransport haben Experimente an Photosynthesekomplexen mittlerweile gezeigt, dass unerwaret langlebige Kohärenzen eine Rolle bei der Energieübertragung spielen [32, 33]. Dies ist überraschend, weil innerhalb dieser Komplexe die Freiheitsgrade der Moleküle stark aneinander gekoppelt sind und zusätzlich eine Kopplung an die Umgebung bei Raumtemperatur besteht. In diesem System wird eine schnelle Dephasierung erwartet, im Gegensatz zu einem System aus kontrollierten ultrakalten Atomen im Vakuum.
Ein intuitives Verständnis der Dephasierung in einem quantenmechanischen Netzwerk ist schwierig und ein solches System zeigt überraschende Eigenschaften. Rechnungen haben gezeigt, dass unter bestimmten Umständen eine Dephasierung den Energietransport unterstützen kann und zu einer schnelleren und effektiveren Übertragung führt [34]. Somit könnten beispielsweise thermische Fluktuationen in den Photosynthesekomplexen die Photosynthese unterstützen. Das theoretische Verständnis einzelner Prozesse ist bereits weit fortgeschritten [35], aber ein vollständiges Bild der komplexen Dynamik in der Photosynthese ist schwierig. Dabei könnten experimentelle Quantensimulationen mit ultrakalten Atomen und Rydberganregungen helfen [36, 37]. Die hohe Kontrollierbarkeit ultrakalter Atome bietet die Möglichkeit, Dephasierungsprozesse gezielt einzusetzen und

die Einflüsse zu studieren. Rydbergatome liefern die notwendigen Wechselwirkungen um den Energietransport zu simulieren.
Auch Quanteninformationsverarbeitung mit Rydberganregungen von neutralen Atomen ist möglich. Bisher wurden die besten Demonstrationen von Quantencomputern mit gefangenen Ionen gemacht. Diese geladenen Teile können einfach mit elektrischen Feldern gefangen werden und zeigen sehr große Kohärenzzeiten [38]. Aber auch auf dem Gebiet der ultrakalten, neutralen Atome wurden wichtige Fortschritte mithilfe von Wechselwirkungen zwischen Rydbergatomen in den letzten Jahren gemacht. Hierzu zählt die Erzeugung von verschränkten Zuständen zwischen zwei Atomen und die Realisation eines quantenmechanischen Gatters [39], das einen elementaren Rechenschritt eines Quantencomputers darstellt. Die Idee, Rydbergatome für Quanteninformationsverarbeitung zu verwenden, wurde bereits im Jahr 2000 für einzelne Atome formuliert [40] und 2001 auf Mehrteilchensysteme erweitert [41]. Das einfachste Gatter basiert auf der Rydbergblockade. Ein Atom im Rydbergzustand kann durch starke Rydbergatom-Rydbergatom-Wechselwirkungen umliegende Atome derart beeinflussen, dass sie nicht angeregt werden können. In dem Gatter fungiert ein Atom (oder eine Wolke von Atomen) als Kontroll-Quantenbit das bestimmt, ob das andere Atom angeregt werden kann oder nicht. Dadurch kann ein Zwei-Quantenbit-Gatter aufgebaut werden. Die Rydbergblockade zwischen zwei einzelnen Atomen wurde gleichzeitig von zwei Gruppen nachgewiesen [42, 43] und kurz darauf wurde auch das Zwei-Quantenbit-Gatter [44] realisiert.
Bereits in der ersten Veröffentlichung zu den Rydberg Gattern [40] wurde eine zweite Variante, die auch auf Rydberg-Wechselwirkungen zwischen zwei Gruppen von Atomen basiert, vorgeschlagen. Allerdings ist die Wechselwirkung zwischen Rydbergatomen in dieser Variante schwächer und unterdrückt nicht die Anregung eines zweiten Rydbergatoms, sondern beeinflusst nur dessen Zeitentwicklung. Dadurch erfährt das Rydbergatom eine Phasenveränderung, die als Gatter umgesetzt werden kann.

In dieser Arbeit stelle ich Experimente vor, die nicht nur die inneren Freiheitsgrade einzelner Atome, wie der elektronische Zustand und die Phase, sondern auch gleichzeitig die Wechselwirkung zwischen Rydbergatomen an einer Förster-Resonanz kohärent kontrollieren. Als externes Kontrollfeld wird ein statisches elektrisches Feld genutzt, um Paarzustände zweier Atome durch den Stark-Effekt in Resonanz zu schieben und die Förster-Resonanz zu erzeugen. Diese Resonanzen werden in einer ultrakalten, magnetisch gefangenen Atomwolke mithilfe von Ramsey-Spektroskopie untersucht und eine bisher unerreichte Auflösung des Energieunterschiedes der Paarzustände dieser Förster-Resonanz erreicht. Die Ramsey-Spektroskopie stellt eine neue Methode dar, induzierte Wechselwirkungen ultrakalter Rydbergatome zu studieren. Sie bietet den technischen Vorteil, dass nur die gesamte Rydbergatomzahl gemessen werden muss und keine zustandssensitive Detektion notwendig ist.

Diese interferometrische Methode ermöglicht auch, die Phase der Rydbergatome zu messen und somit Informationen über die kohärente Entwicklung des Systems zu gewinnen. Mithilfe eines Doppel-Ramsey-Experiments, bei dem das elektrische Feld gepulst wurde, um eine Ramsey-ähnliche Sequenz der Wechselwirkungsstärke zu erzeugen, konnten kohärente Oszillationen im wechselwirkenden Paarzustandssystem gemessen werden. Diese Messungen weisen direkt die kohärente Entwicklung der Paarzustände der wechselwirkenden Atome nach. Gleichzeitig wird aber auch eine reduzierte Sichtbarkeit des Ramsey-Interferenzmusters bei starken Wechselwirkungen während der Ramsey-Messungen beobachtet.
Berechnungen der Wechselwirkungsstärke und der Winkelabhängigkeit der Wechselwirkung zwischen zwei Rydbergatomen bei einer Förster-Resonanz ermöglichen eine Simulation der Experimente. Dazu habe ich das Konzept eines Paarzustandsinterferometers eingeführt. Die Ergebnisse der Simulationen stimmen sehr gut mit den Messungen überein und unterstützen die Beobachtung, dass sich das wechselwirkende Mehrteilchensystem kohärent verhält. Der gemessene Verlust an Sichtbarkeit wird auch in den vollständig kohärenten Simulationen beobachtet und kann auf Dephasierungen innerhalb des kohärenten Paarzustandssystems zurückgeführt werden. Die Kohärenz in einem solchen System ist eine grundlegende Voraussetzung für die Anwendungen im Bereich der Quanteninformationsverarbeitung und Quantensimulation. Weitere Messungen und Simulationen zeigen eine Phasenverschiebung der Rydbergatome, die durch die Rydberg-Wechselwirkung erzeugt wird. Die Stärke der wechselwirkungsinduzierten Phasenverschiebung folgt einem dispersiven Verlauf im elektrischen Feld nahe der Förster-Resonanz. Das zeigt, dass die Stärke der Wechselwirkung und das Vorzeichen, von attraktiver zu repulsiver Wechselwirkung, durch das externe Kontrollfeld kohärent variiert werden kann. Solche wechselwirkungsinduzierten Phasenverschiebungen können beispielsweise das Zwei-Quantenbit-Gatter realisieren [40].

Ein weiteres sehr neues Forschungsgebiet ist die ultrakalte Chemie. Dieses Gebiet zwischen ultrakalter Physik und Chemie mag irritierend wirken, weil bei ultrakalten Temperaturen, bei denen die Bewegung der Atome praktisch eingefroren ist, auf den ersten Blick keine chemischen Reaktionen auftreten. Doch aufgrund der quantenmechanischen Wellennatur der Teilchen können bei diesen Temperaturen durch Streuprozesse der Wellenfunktionen der Teilchen durchaus chemische Prozesse auftreten. Bisher gibt es nur wenige Experimente, die dem Feld der ultrakalten Chemie zugeordnet werden können, beispielsweise chemische Reaktionen ultrakalter Moleküle [45], Bose-Einstein Kondensation von Molekülen [46, 47], Efimov Resonanzen [48] und die Photoassoziation von langreichweitigen Rydbergmolekülen [49].
Diese Rydbergmoleküle zeigen einen neuen Bindungsmechanismus, der bisher in der Chemie nicht bekannt war und aufgrund der geringen Bindungsenergien nur bei ultrakalten Temperaturen möglich ist. Die Moleküle stellen einen gebundenen Zustand

zwischen einem Atom im Rydberg-Zustand und einem Grundzustandsatom, das sich innerhalb der Wellenfunktion des Rydbergelektrons befindet, dar. Das Rydbergelektron streut an dem Grundzustandsatom und erzeugt dadurch ein attraktives Potential, das zur Bindung führt.
Dieser Bindungsmechanismus stellt allerdings nicht die einzige überraschende Eigenschaft dieser Moleküle dar. Ich zeige in dieser Arbeit Messungen eines linearen Stark-Effekts der Moleküle bei kleinen elektrischen Feldern, ein eindeutiger Hinweis auf ein permanentes, räumlich ausgerichtetes Dipolmoment. Ein solches Dipolmoment ist aus verschiedenen Gründen üblicherweise in zweiatomigen, homonuklearen Molekülen nicht möglich.
Ein permanentes Dipolmoment erfordert eine Ladungstrennung innerhalb des Moleküls. Dies tritt normalerweise in heteronuklearen Molekülen, die aus verschiedenen Elementen bestehen, durch verschiedene Elektroaffinitäten auf. In homonuklearen Molekülen ist keines der beteiligten Atome ausgezeichnet und es entsteht keine polare Ladungsverteilung. Bei den hier untersuchten Molekülen ist eine Ladungstrennung trotzdem möglich, weil sich die Atome in deutlich verschiedenen Anregungszuständen befinden und sich deshalb unterschiedlich verhalten. Im Falle einer solchen Ladungstrennung tritt jedoch nicht immer ein Dipolmoment entlang der Molekülachse auf, weil die Zustände, bei denen die Ladungstrennung entgegengesetzt ist, ohne elektrisches Feld entartet sind. Aufgrund dieses Symmetrieargumentes ist der Eigenzustand des Moleküls eine Mischung beider Zustände, deren Effekt auf das Dipolmoment sich aufhebt. Bei den langreichweitigen Rydbergmolekülen unterscheiden sich die zwei beteiligten Atome aufgrund der Anregung des Rydbergatoms so deutlich in der Größe, dass ein Austausch des Ladungsschwerpunktes sehr unwahrscheinlich ist. Das Molekül wird direkt in einem Zustand, der eine Ladungstrennung aufweist, erzeugt und besitzt ein Dipolmoment entlang der Molekülachse.
Dieses Dipolmoment entlang der Molekülachse zeigt sich allerdings nur dann im räumlich festen Laborbezugssystem, wenn das Molekül sich nicht dreht und das Dipolmoment sich folglich nicht zu null mittelt. Die langreichweitigen Rydbergmoleküle rotieren aufgrund ihrer Größe sehr langsam. Innerhalb der Lebensdauer des Moleküls ist diese Bewegung vernachlässigbar und das Molekül zeigt eine räumliche Orientierung der Ladungstrennung, ein permanentes Dipolmoment.
Die experimentell bestimmten Dipolmomente der langreichweitigen Rydbergmoleküle stimmen exzellent mit Rechnungen überein [50], die in Kollaboration mit dem Max-Planck-Institut für Physik komplexer Systeme in Dresden und dem Harvard-Smithonian Center for Astrophysics in Cambridge, USA, durchgeführt wurden.

Introduction

Within the many areas of physics one of the hottest fields is ultracold physics. This regime can be defined as temperatures close to absolute zero, at 1 mK and below, where quantum-mechanical properties start to take over. Even though this is far from everyday life, this field can address many of the open challenges in physics and may even result in real-world applications based on quantum effects. The idea of this field, broken down to the simplest words, is that atoms can be understood and controlled brilliantly once they are brought to an almost perfect stop at a certain position in the laboratory.
Especially the combination of ultracold atoms with highly excited atoms, co-called Rydberg atoms, is very promising. Ultracold ground state atoms and Rydberg atoms are counterparts in many ways, for example in the size difference of three orders of magnitude and also in the interaction, which is very weak for ultracold ground state atoms but very strong between Rydberg atoms. Combining these contrasts can lead to interesting new physics and new applications and most of the interest in ultracold Rydberg atoms relies on these extremes.
Here I will report on two kinds of experiments. The first one is dedicated to coherent control of an ensemble of atoms in the presence of strong interactions, where the interactions are induced by Förster resonances between Rydberg atoms. The extremely strong interactions between Rydberg atoms, compared to ground state atoms, enable to isolate and coherently control a single interaction channel. The second kind of experiments concerns the electric properties of ultralong-range Rydberg molecules. Because of the vast differences of length scales in these homonuclear diatomic Rydberg molecules a permanent electric dipole moment forms, contradicting the standard beliefs in chemistry and physics. Both experiments, even though they are quite different, stem from the combination of the research fields of ultracold atoms and Rydberg atoms and give an idea of the versatility of this area of physics.
Ultracold atoms boosted since the achievement of cooling and trapping of atoms with laser light [1], that was awarded with the Nobel prize for Steven Chu, Claude Cohen-Tannoudji and William D. Phillips in 1997 [2]. This laser cooling technique enables to decelerate gaseous atoms in a vacuum to velocities that can be neglected on the timescale of the experiments, but without condensing them to a liquid or solid.
In these highly controllable systems, either single atoms or ensembles of atoms, a bunch

of interesting things can be done. The prospects are a better understanding and control of conventional physics subjects, but also fundamentally new physics that might have been impossible in other regimes or even totally unknown before. So far the probably biggest breakthrough was the achievement of Bose-Einstein condensation, honored with the Nobel prize for Eric A. Cornell, Wolfgang Ketterle and Carl E. Wieman in 2001 [3]. Besides basic understanding of atomic and optical physics, applications can be found in many other areas and I will only mention some of them. One well known example of a real-world application of ultracold atoms are atomic clocks [4, 5], that serve as frequency and time standards since years. Similar ultra-high-precision quantum metrology [6] can also be done of gravitation [7]. Another popular field is quantum simulation, envisioned by Richard Feynman already in 1982 [8], that potentially simulates vast fields like condensed matter physics or even complex biological structures [9, 10]. One recent breakthrough is the implementation of an Ising chain in an optical lattice [11].
In quantum simulators the quantum mechanical system of interest is modeled by an artificial system that shows the same characteristics. An important tool in the toolbox of quantum simulation is a tunable, long-range interaction to mimic the Hamiltonian of choice. Besides polar molecules [12] also strongly interacting Rydberg atoms were proposed to induce these interactions [10, 13].
In Rydberg atoms one electron is excited to a high principal quantum number, where the extent of the Rydberg electron wavefunction is large. These atoms show strong polarizabilities and usually interact via van der Waals interaction [14, 15]. Under certain conditions the interaction can further be tuned by external fields to long-range dipole-dipole interaction. These so-called Förster resonances in Rydberg atoms show many advantages. Besides the long-range character they offer tunability of the strength and the sign of the interaction, from attractive to repulsive, by external control fields. They were first observed in two seminal experiments in Tom Gallagher's group in atomic beam experiments: in 1981 [16] using an electric field as the control parameter and in 1982 [17] using a microwave field. Especially the possibility to tune the strength of the interaction attained much interest and Förster resonances have been studied in quite some experiments in many groups [18, 19, 20, 21, 22, 23, 24, 25], using various control parameters.
The extension of Rydberg excitation to ensembles of ultracold atoms offers the possibility of coherent Rydberg excitation [26, 27] and of coherent experiments in the energy transfer [28] between pairs on interacting Rydberg atoms. As coherence is fundamental for most applications of ultracold atoms, these experiments are a big step towards many proposed applications. Besides the simulation of ground states of strongly correlated many body systems also quantum dynamics in the time dependent development of the system are envisioned. This can be for example a simulation of the quantum random walk [29] or of coherent energy transport [18]. The latter is especially interesting in biophysics, where non-radiative exciton dynamics is relevant for fast and efficient energy

transport in photosynthesis and photoluminescence [51]. This Förster resonant energy transfer (FRET) was first described in a seminal contribution by Theodor Förster [30] in 1948 as an incoherent, non-radiative energy transfer between two molecules, if their excited states are in resonance. The Förster resonances between Rydberg atoms were named after this FRET process in biophysics due to strong similarities [31], as both arise by non-radiative coupling of oscillating dipole moments.

Despite the first description as an incoherent energy transport, recent experiments showed that surprisingly long-lived coherence plays an important role in the FRET process of photosynthetic complexes [32, 33]. This is remarkable as the internal degrees of freedom of the molecules in the photosynthetic complexes are strongly coupled and also a strong coupling to the environment at room temperature exists, a situation that is totally unfavorable to preserve coherence in contrast to the idealized situation of ultracold atoms surrounded by vacuum.

Counter intuitively, a certain degree of dephasing in a quantum network can assist transport phenomena, as shown in [34], and lead to faster and more efficient excitation transport. Hence thermal fluctuations in the photosynthetic complexes might assist efficient light harvesting. Even though the importance of coherence in biophysics has been shown and the individual energy transport processes can be well explained theoretically [35], a throughout understanding of the highly complex dynamics in these quantum aggregates might be obtained by modeling the system using well controlled ultracold atoms. Experimental realizations of these quantum dynamics are proposed using Rydberg atoms [36, 37].

Rydberg atoms are also promising for quantum information processing. These applications, e.g. encoding, communication and computation of information using quantum-mechanical states, necessitates a highly controlled system as any form of dissipation or dephasing degrades the quantum state that exhibits the information. The best demonstrations of quantum computers are realized with trapped ions [38] because of easy single-ion trapping with immense coherence times. However, important progress has been made in neutral atom computing, especially by using Rydberg interactions to create entanglement and gates [39]. The idea of using Rydberg atoms for quantum gates was first formulated in 2000 [40] for single atoms and extended to ensembles of atoms in 2001 [41]. The basic idea of the two-qubit gate relies on the Rydberg blockade. One atom (or atoms in one ensemble) in the Rydberg state can influence (due to Rydberg-Rydberg interaction) the excitation of a second atom. Thereby one atom serves as a control qubit that defines if the second atom (target) is exited or not, realizing a two-qubit gate. This blockade effect between spatially separated single atoms was independently realized by two groups [42, 43], quickly followed by the realization of the two-qubit blockade gate [44].

Already in the first proposal of a Rydberg gate [40] a second type of gate protocol was described. This two-qubit gate also relies on Rydberg-Rydberg interaction between the

control and the target atom(s), but in contrast to the blockade gate here the interaction is weaker and only influences the phase of the target. An accumulated phase shift of π of the target atom realizes a gate operation.
Quantum communication and cryptography [52] need single photon sources. Besides many other approaches [53], Rydberg excitations in ultracold atoms are proposed [54, 55] and realized [56] as single photon sources.

Here, I present experiments that not only control the internal degrees of freedom of the Rydberg atoms, the electronic state and the phase of single atoms, but also coherently control the relative phase of the electronic states of two Rydberg atoms via controllable interactions close to a Förster resonance. This preservation of coherence in strongly interacting ensembles of atoms provides an essential step for applications of ultracold atoms in quantum simulation and quantum computing. For example, I realize an interaction-induced phase shift of Rydberg atoms, necessary for the proposed two-qubit phase gate [40].
It should be noted that ultracold atoms are not the only promising foundation for coherent applications like quantum computing and simulation [57]. For example the already mentioned trapped ions [38] or quantum dots in solid state materials [58] also offer long coherence times. Every approach has its advantages and disadvantages concerning interactions, coherent control and scalability.

Another new topic is ultracold chemistry on the borderline of chemistry and ultracold physics, that can be specified as the regime where chemical processes are dominated by single partial-wave scattering. This field developed fast in the last years as visible in the number of citations of papers including 'ultracold chemistry' in the topic (Figure 0.1). Ultracold chemistry may appear strange since the atoms basically rest at ultracold temperatures and no chemical reactions are expected. But due to the quantum mechanical wave nature of the particles at these temperatures s- and p-wave scattering can have effects on chemical reactions. Experimental regimes where ultracold chemistry is relevant are hard to reach and only recently progress in the production of ultracold molecules [59, 12] enabled to study chemical reactions on the quantum level as it has been done in [45].
However, only a limited number of experiments have been performed to date that can be attributed to the field of ultracold chemistry. Besides the photoassociation of ultracold molecules other examples are Bose-Einstein condensation of molecules [46, 47] and Efimov resonances [48]. Among these few the photoassociation of ultralong-range Rydberg molecules is exceptional [49]. It is not so much the chemical dynamics in the production of the molecular state, but the binding mechanism itself that justifies this statement [60]. This bound state between one Rydberg atom and one ground state atom binds due to low energy scattering of the Rydberg electron off the ground state

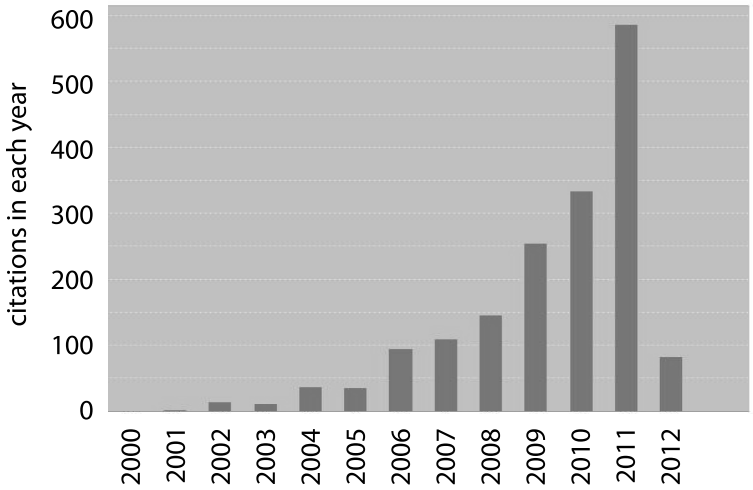

Figure 0.1: Number of citations per year of papers including 'ultracold chemistry' in the topic. Data downloaded from 'ISI web of knowledge' April 23, 2012.

atom, a binding mechanism not known to chemistry before and due to the small binding energy only possible at ultracold temperatures. Besides this astonishing binding these molecules also feature an unexpected permanent dipole moment, usually forbidden in diatomic molecules due to symmetry arguments. I will present experimental proof for this polar character, contradicting the long held belief that homonuclear diatomic molecules cannot have permanent dipole moments. The experimental results are in perfect agreement with calculations of the dipole moment [50], that were done in collaboration with the Max-Planck-Institut für Physik komplexer Systeme in Dresden, Germany, and the Harvard-Smithonian Center for Astrophysics in Cambridge, USA.
This outstanding example of ultracold chemistry is also a fine prototype of fundamentally new and unexpected physics that emerge from the field of ultracold atoms. Like most presented experiments on ultracold Rydberg atoms it relies on the extremes of this field, as the size difference between the ground state atom and the Rydberg atom, defining the binding length, permits the permanent dipole moment in the first place. This shows that combining these counterparts may lead to many expected but also unexpected results, in this thesis and in the future.

This thesis is structured as follows:

After a theoretical introduction to Rydberg atom physics and Ramsey experiments, binary Rydberg-Rydberg interactions are calculated and the origin of the permanent dipole moments in ultralong-range Rydberg molecules is described in chapter 1. Following this introduction, chapter 2 summarizes the experimental setup, including the preparation of ultracold atoms and the narrowband laser excitation to Rydberg states.

Experimental results are presented in chapter 3 and 4, where first Förster resonant Rydberg-Rydberg interactions are studied using Ramsey experiments, starting from highly resolved measurements of splittings of Stark-tuned Förster resonances in the electric field over dephasing mechanisms at the resonances to the measurement of an interaction-induced phase shift. Fully coherent simulations of these experiments using the concept of a pair state interferometer complete the understanding of the coherent dynamics of the interacting ensemble of ultracold atoms. Subsequently, in chapter 4, the Stark effect of the ultralong-range Rydberg molecules is measured and the permanent dipole moment is obtained.

1 Theoretical foundations

This chapter focuses on a theoretical analysis of pairwise interactions between a pair of Rydberg atoms, so-called binary interactions. I will establish the basics to understand atom-light interaction in Ramsey experiments for two-level and many-level systems and I will introduce the theoretical treatment of alkali Rydberg atoms, their behavior in external electric and magnetic fields and especially their binary interactions.
The second part of this chapter describes the properties of ultralong-range Rydberg molecules with a focus on the origin of their permanent electric dipole moment.

1.1 Atom-light interaction

All experiments in this thesis base upon optical excitation to Rydberg or Rydberg-molecule states, which have to be described by near-resonant atom-light interaction. An exact description of the interaction between light and atoms is often impossible, but with reasonable approximations good results can be obtained. The major approximations that are used in this thesis are a monochromatic, classical light field that nearly coincides in frequency with a transition frequency in the atoms (rotating wave approximation). The latter assumption is justified as the transition frequency to the Rydberg states is about 1000 THz whereas the usual detunings in the spectroscopy experiments are on the order of MHz, nine orders of magnitude smaller and clearly near-resonant. The approximation of monochromatic excitation is not fully justified for every performed experiment, even for the used narrowband laser system. Deviations are especially visible in the pair state interferometer experiments in chapter 3.2.5. Effects beyond this approximation will be discussed throughout the thesis whenever necessary.
Using these approximations the Hamiltonian that describes the atom-light system can be written as

$$H = H_A + H_{AL}, \tag{1.1}$$

where

$$H_A = \frac{\hat{p}^2}{2m} + \sum_k \hbar\Omega_k \left|\Psi_k\right\rangle \left\langle\Psi_k\right| \tag{1.2}$$

describes the unperturbed atom with the eigenfunctions $|\Psi_k\rangle$ and eigenenergies $\hbar\Omega_k$.

The interaction with the classical light field

$$\vec{E}(\vec{r},t) = \vec{E}_0(\vec{r})\cos(\omega_L t + \phi)$$

with amplitude $|\vec{E}_0(\vec{r})|$, phase ϕ, polarization $\frac{\vec{E}_0(\vec{r})}{|\vec{E}_0(\vec{r})|}$ and frequency ω_L is described by the atom-light interaction Hamiltonian

$$H_{AL} = -\sum_{i\neq k} \hat{d}\cdot\vec{E}(\vec{r},t)\cdot|\Psi_k\rangle\langle\Psi_i|. \tag{1.3}$$

$\hat{d} = -e\hat{r}$ is the dipole moment operator of the atom. Calculations of the dipole matrix elements are explained in chapter 1.2.2.
The eigenfunctions $|\Psi_k\rangle$ of H_0 are no eigenfunctions in the presence of the light field. That leads to a mixing of the eigenstates of H_0 [61]. Diagonalization of the full Hamiltonian H gives the new eigenfunctions and eigenenergies. The time evolution of an arbitrary wavefunction $|\psi\rangle$ can be calculated by using the Schrödinger equation [62]

$$i\hbar\frac{\partial}{\partial t}\psi(\vec{r},t) = H\psi(\vec{r},t). \tag{1.4}$$

In the case of additional static or oscillating fields or interatomic interactions additional terms in the total Hamiltonian might contribute. In any case, by defining the correct Hamiltonian describing the system of interest and the initial state $|\psi\rangle$ the complete dynamics can be derived. This will be used in the concept of the pair-state interferometer in chapter 3.2.3.

1.1.1 Two-level system and optical Bloch equations

For an ideal two-level atom with the states $|g\rangle$ and $|e\rangle$ with the relative energy difference $\hbar\omega_{eg}$ the time evolution under the influence of a near-resonant driving field can be conveniently described by the optical Bloch equations (OBE). To derive the OBE the density matrix $\rho = |\Psi_i\rangle\langle\Psi_k|$ is introduced; details of this derivation can be found in [63]. The diagonal elements ρ_{ii} are the populations in the state i (either $|g\rangle$ or $|e\rangle$) and the off-diagonal elements, so-called coherences, describe the response of the system to the driving light field. The time evolution of the system in the density matrix formalism can be calculated from the von-Neumann equation

$$\frac{\partial}{\partial t}\rho = -\frac{i}{\hbar}[H,\rho]. \tag{1.5}$$

The three components of the Bloch vector $\vec{\rho}$ can be defined as

$$\begin{aligned} u &= \rho_{ge} + \rho_{eg} \\ v &= i(\rho_{eg} - \rho_{ge}) \\ w &= \rho_{ee} - \rho_{gg}, \end{aligned} \tag{1.6}$$

where w describes the inversion, i.e. the population difference in the ground and excited state, and u, v describe the coherences. One can obtain the time evolution of the Bloch vector from equation (1.5) and get the OBE in the rotating wave approximation [63]

$$\begin{aligned} \dot{u} &= -\delta v \\ \dot{v} &= \delta u + \Omega_0 w \\ \dot{w} &= -\Omega_0 v. \end{aligned} \tag{1.7}$$

$\delta = \omega_L - \omega_{eg}$ is the detuning of the light relative to the atomic resonance frequency in angular frequencies and $\Omega_0 = \frac{\langle g|\hat{d}\cdot\vec{E}|e\rangle}{\hbar} = \frac{d_{ge}|\vec{E}|}{\hbar}$ is the Rabi frequency, describing the strength of the coupling of the light field to the atom, with the dipole matrix element $d_{ge} = \langle g|\,\hat{d}\,|e\rangle$. If the OBE is written as

$$\frac{d}{dt}\begin{pmatrix} u \\ v \\ w \end{pmatrix} = \begin{pmatrix} -\Omega_0 \\ 0 \\ \delta \end{pmatrix} \times \begin{pmatrix} u \\ v \\ w \end{pmatrix} \tag{1.8}$$

the time evolution of the two-level system is described by a rotation of the Bloch vector around $\Omega_0\vec{e}_1 + \delta\vec{e}_3$. For the fundamental properties, and for the basic understanding of Ramsey experiments in this thesis, two cases are most relevant. In the case of resonant light ($\delta = 0$) the OBE describe a rotation around the u-axis with the oscillation frequency Ω_0. Thereby the population inversion w is changed periodically. This describes well-known Rabi oscillations in a coherent system. For example, a resonant pulse of duration $t = \pi/\Omega_0$, called a π-pulse, induces a rotation by π and inverses the population. The absolute change of the inversion depends on v, hence it is called the absorptive component of the Bloch vector.
In the case of a finite detuning but no light field ($\Omega_0 = 0$) the Bloch vector oscillates around w with the oscillation frequency given by the detuning δ. The inversion does not change, but the components u and v. Generally, if the system is driven with near resonant light, $\Omega_0 \neq 0$ and $\delta \neq 0$, the Bloch vector oscillates around $\Omega_0\vec{e}_1 + \delta\vec{e}_3$. The oscillation frequency is then enhanced to the effective Rabi frequency $\Omega_{eff} = \sqrt{\Omega_0^2 + \delta^2}$, but the amplitude of the oscillation in w is reduced.
The optical Bloch equations fully describe the coherent evolution of an isolated two-level atom in the presence of a near resonant light field, within the rotating wave approximation. In chapter 3.1.1 the OBE are used to explain the Rydberg Ramsey interferometer. In real systems, a coupling to the environment usually generates dephasing and decoherence processes that damp the coherent oscillations. To include these processes the OBE can be extended, analog to the nuclear spin equations first proposed by F. Bloch

in 1946 [64], by introducing the excited state lifetime T_1 and the coherence time T_2:

$$\begin{aligned} \dot{u} =& -\delta v - \frac{u}{T_2} \\ \dot{v} =& \delta u + \Omega_0 w - \frac{v}{T_2} \\ \dot{w} =& -\Omega_0 v - \frac{w+1}{T_1} \end{aligned} \tag{1.9}$$

T_1 describes the decay of the inversion, i.e. the excited state lifetime. T_2 describes a decay of the coherent oscillations without changing the inversion. These are energy conserving processes that lead to a loss of coherence in the system. There are numerous possible processes as scattering of radiation or inhomogeneous broadening due to, e.g., Doppler effects and magnetic or electric field gradients and so forth.
These optical Bloch equations including phenomenological decay constants (1.9) are used in chapter 3.2.2 to obtain quantitative values for dephasing processes.

1.1.2 Ramsey experiments

Ramsey experiments are advantageous in many aspects to study the coherent evolution of atoms. For a two-level system $|g\rangle$ and $|e\rangle$ with an energy difference of $\hbar\omega_0$ Ramsey experiments can nicely be calculated and understood. Extensions to many-level systems will be discussed in chapter 3.2.3.
In Ramsey experiments two short oscillatory field pulses couple the two-level system, separated by a delay time during which no coupling occurs. The Ramsey pulse sequence is shown in Figure 1.1 (d). Here, the coupling field is monochromatic and a fully coherent system is assumed. In an experimental realization these assumptions are justified if the Fourier width of the finite coupling pulse is considerably broader than the linewidth of the coupling field and if the coherence length is longer than the experimental sequence. Furthermore, here the system is only treated in the limit of small excitations to give a good understanding of the fundamental processes. Beyond this limit the OBE (1.7) or the Schrödinger equation (1.4) can numerically be solved for the Ramsey sequence, as it is done for the simulations in chapter 3.
In the presence of a coupling field the wavefunction can be expressed as

$$|\psi\rangle = c_g(t)e^{-i\omega_g t}|g\rangle + c_e(t)e^{-i\omega_e t}|e\rangle\,. \tag{1.10}$$

For weak excitations $(\omega_0 - \omega_L)\tau \ll 1$ and near resonant light (rotating wave approximation) the time evolution of (1.10) is calculated from the Schrödinger equation (1.4) and one obtains for the excited state coefficient [61]

$$c_e = \Omega^* \frac{\sin(\delta\tau/2)}{\delta} = \frac{\Omega^*\tau}{2}\mathrm{sinc}(\delta\frac{\tau}{2}). \tag{1.11}$$

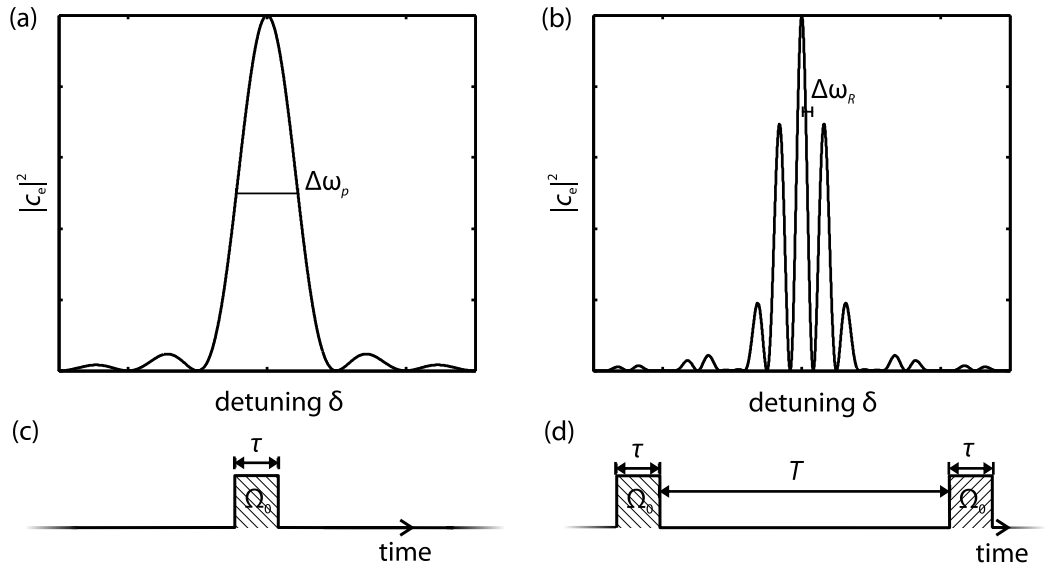

Figure 1.1: (a) Excitation spectra for a single light pulse of length τ and (b) for a Ramsey sequence with two equally long pulses. The Fourier width $\Delta\omega_p$ of the single pulse and the width of the Ramsey fringes $\Delta\omega_R$ are indicated. (c,d) show the pulse sequences of the single pulse and Ramsey sequence.

The population $|c_e|^2$ hence shows a sinc^2-function spectrum in the detuning of the coupling field (see Figure 1.1 (a)). The full width at half maximum (FWHM) is

$$\Delta\omega_p = 5.29 \cdot \frac{1}{\tau} \tag{1.12}$$

where τ is the pulse length of the excitation pulses. In the experiments in chapter 3 0.15 μs excitation light pulses are used, which corresponds to a FWHM of $2\pi \times 5.61$ MHz. For resonant light, $\delta = 0$, the time dependence reduces to $|c_e|^2 = \frac{\Omega^2\tau^2}{4}$ and shows a quadratic increase in time. This is, of course, only true in the approximation of small excitations. For longer excitation pulses this quadratic increase crosses over to oscillations, the so-called Rabi oscillations.
In the case of two separated pulses, as shown in Figure 1.1 (d), interference effects arise and one obtains

$$c_e(t) = \frac{\Omega^*}{2}\left(\frac{1-e^{i\delta\tau}}{\delta} + e^{i\delta(T+\tau)}\frac{1-e^{i\delta\tau}}{\delta}\right), \tag{1.13}$$

similar to equation (1.11). The two terms of this expression can easily be understood. The first term, identical to equation (1.11), describes the amplitude of the excited state after the first pulse. The second term describes the second light pulse. Only the phase of the second term is changed depending on the delay time T and the detuning δ. This phase defines if the second pulse increases or decreases the population $|c_2(t)|^2$, that corresponds to constructive and destructive interference.

The population in the excited state yields

$$\begin{aligned} |c_e(t)|^2 = & \frac{\Omega^2}{4}\left|\frac{1-e^{i\delta\tau}}{\delta}\right|^2 \cdot \left|1+e^{i\delta(T+\tau)}\right|^2 \\ = & \left|\frac{\Omega\tau}{2}\right|^2 \mathrm{sinc}^2(\delta\tau/2)\cos^2\left(\delta(T+\tau)/2\right) \end{aligned} \tag{1.14}$$

and is plotted in Figure 1.1 (b). The envelope of this Ramsey spectrum shows the same sinc-function as for the single pulse (1.11). The additional cosine term describes the interference and leads to a modulation of the spectrum, the so-called Ramsey fringes. The width of the fringes in frequency space is $\Delta\omega_R = \frac{1}{2(T+\tau)}$. The fringe pattern in Ramsey experiments is inversely depending on the delay time between the pulses, whereas the width of the envelope is inversely depending on the pulse length. This offers the advantage that the spectral resolution of the Ramsey experiment can be considerably better than the resolution of a single pulse experiment. For example, in the case of equally long sequences of time T_S, the Ramsey method with two short light pulses in the beginning and the end of the sequence offers a resolution of $0.5 \cdot \frac{1}{T_S}$, a factor of 1.7 better than in the case of one long excitation pulse with a resolution of $0.84 \cdot \frac{1}{T_S}$. However, this increase in resolution is only relevant if the phase is not disturbed between the light pulses. The treatment so far has been done for a fully coherent system. A loss of coherence due to dephasing and decoherence processes during the delay time, as discussed in chapter 1.1.1, leads to less effective coupling of the second light pulse in equation (1.13). The exact dependence of the Ramsey spectrum on the loss of coherence depends on the involved processes. Phenomenological, the modulation in the Ramsey fringes is reduced. To describe this effect the visibility V

$$V = \frac{P_{\max} - P_{\min}}{P_{\max} + P_{\min}} \tag{1.15}$$

is introduced, where $P_{\max}$ ($P_{\min}$) describe the maximal (minimal) populations in the excited state, as shown in Figure 1.2. The population in the excited state can then be described by

$$P = |c_e(t)|^2 = \left|\frac{\Omega\tau}{2}\right|^2 \mathrm{sinc}^2(\frac{\delta\tau}{2}) \cdot \left(\frac{2V}{1+V} \cdot \cos^2(\frac{\delta(T+\tau)}{2}) + \frac{1-V}{1+V}\right). \tag{1.16}$$

This function is the basis for the fit function (3.3) that is used to characterize the measured Ramsey spectra in this thesis.

1.2 Rydberg atoms

Rydberg atoms are highly excited atoms, where (at least) one electron is excited to a high principal quantum number. They show exaggerated properties in many aspects. Even so, they can be well described theoretically as they behave hydrogen-like.

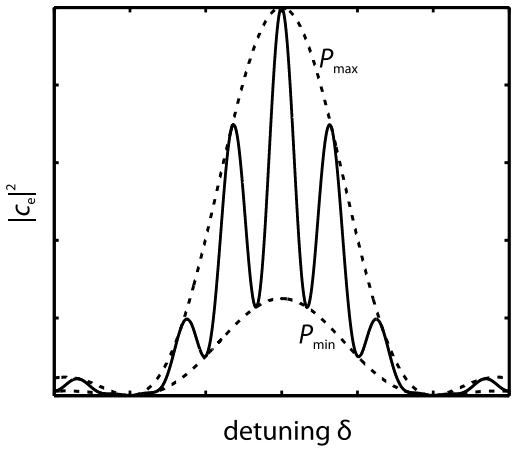

Figure 1.2: Ramsey spectrum for a reduced visibility of $V = 0.5$ (solid line). The dashed lines show the maximal and minimal populations in the excited state

The study of highly excited atoms reaches back to 1885, when an expression for the energy levels of the Balmer-series in hydrogen was found [65]. This series could be linked to the binding energy of the hydrogen electron in the Bohr atom model [66] and can be expressed by fundamental constants as

$$E_n = -hc\frac{Ry}{n^2}, \tag{1.17}$$

where n is the principal quantum number and

$$Ry = \frac{e^4 m_e}{2(4\pi\epsilon_0\hbar)} = 13.6\text{eV} \tag{1.18}$$

is the Rydberg constant, e the electron charge, m_e is the electron mass, ϵ_0 the vacuum permittivity and $\hbar$ the reduced Planck constant.
Quantum mechanics offers nowadays the exact calculation of the energy levels of hydrogen and superseded the Bohr model. However, heavier atoms cannot be solved analytically in quantum mechanics, but the Balmer-series still provides the correct scaling of the energies.

In the following subsections I will introduce the basic formalism to describe energy levels, wavefunctions and dipole matrix elements of alkali Rydberg atoms. A detailed and comprehensive description can be found in [14].

1.2.1 Alkali Rydberg states

Alkali atoms are the workhorses in atomic physics and especially favorable for Rydberg experiments as they have only one electron in the outermost shell. Even though divalent

state	$n^2s_{1/2}$	$n^2p_{1/2}$	$n^2p_{3/2}$	$n^2d_{3/2}$	$n^2d_{5/2}$	$n^2f_{5/2}$	$n^2f_{7/2}$
δ_0	3.1311804	2.6548849	2.6416737	1.34809171	1.34646572	0.0165192	0.0165437
δ_2	0.1784	0.2900	0.2950	-0.60286	-0.59600	-0.085	-0.086

Table 1.1: Quantum defect parameters for ^{85}Rb

atoms, like strontium [67], might possess some advantages that open new opportunities in the field of Rydberg physics, for most Rydberg experiments the advantages of alkali atoms prevail. Multiple excitations of Rydberg electrons are not possible under usual conditions and autoionization by two-electron excitation does not appear. Furthermore, alkali Rydberg atoms behave very much like hydrogen. The inner, closed shells screen the nucleus charge, resulting in a hydrogen-like net charge $Z = 1$ (in units of the electron charge e) if the valence electron is located far outside the inner shells. This is thoroughly the case for high angular momentum (quantum number l) Rydberg states, but electrons in low angular momentum states still penetrate and polarize the inner shells. As a result, the electron binding potential is angular momentum dependent and lower than the Coulomb potential in hydrogen. This leads to a lifting of the l-degeneracy and to a slightly stronger binding energy compared to hydrogen (cp. equation (1.17)).
These differences can be accounted for by quantum defect theory [68] that describes the stronger binding energy by introducing an effective principal quantum number $n^\star = n - \delta_{nlj}$. The Balmer formula (1.17) is extended to

$$E'_n = -hc\frac{Ry}{(n-\delta_{nlj})^2} = -hc\frac{Ry}{(n^\star)^2}. \tag{1.19}$$

The positive quantum defects δ_{nlj}, depending on the quantum numbers n, l, j, increase the binding energy of the Rydberg states compared to hydrogen. They are calculated from the Rydberg-Ritz formula

$$\delta_{nlj} = \delta_0 + \frac{\delta_2}{(n-\delta_0)^2} + \ldots, \tag{1.20}$$

where higher order terms are usually omitted as they contribute only insignificantly. The coefficients δ_0 and δ_2 for rubidium can be found in table 1.1. They are obtained from microwave spectroscopy in ^{85}Rb for the s,p and d states [69] and the f states [70]. For the g state a quantum defect was measured from resonant energy transfer [71] to be $\delta_g = 0.00405$. The fine structure splitting between $g_{7/2}$ and $g_{9/2}$ could not be resolved in these measurements and the quantum defect was only obtained for $n = 30$, therefore no extrapolation to higher quantum numbers using the Rydberg-Ritz formula in equation (1.20) was possible. However, at high principal quantum numbers the variations of the quantum defects with n are small and for the relevant Rydberg states here the $n = 30$ quantum defect is expected to give a reasonable estimate.

The hyperfine structure (HFS) in Rydberg states is very weak as the coupling of the total angular momentum to the nuclear magnetic dipole moment is suppressed by the large extend of the Rydberg electron wavefunction. The HFS scales as $1/n^3$ [69, 72] for s and p states. For angular moments $l > 1$ no hyperfine structure was measured. Usually this small hyperfine structure is neglected and n, l, j, m_j are good quantum numbers to define quantum defects and to describe the Rydberg states.
As the electron probability density shifts to bigger distances from the nucleus with higher angular momentum, the quantum defects decrease. For Rydberg states with $l > 4$ no quantum defects exist and the energy levels of the alkali Rydberg states coincide with the hydrogen model in equation (1.17). Since the quantum defect of the ns Rydberg states is about 3.13 the closest degenerate high-l Rydberg states are of principal quantum number n-3. This can also be seen in Figure 1.3.

1.2.2 Calculation of wavefunctions and dipole matrix elements

To calculate wavefunctions and dipole matrix elements I use the program *rydLib*, that is documented in the thesis of Björn Butscher [73]. Here, I will only illustrate the major challenges for calculating wavefunctions and dipole matrix elements for alkali Rydberg atoms and motivate the essential steps in *rydLib*.
In hydrogen, the non-relativistic wave functions ψ of the electron can be calculated analytically in the absence of fine structure as solutions to the Schrödinger equation [62]

$$\left(-\frac{\hbar^2}{2m_e}\nabla^2 + V(r)\right)|\psi\rangle = E_\psi\,|\psi\rangle \tag{1.21}$$

with the radially symmetric coulomb potential $V(r)$ and the energy E_ψ of the state ψ. Using the ansatz

$$\psi(r,\Theta,\phi) = \frac{1}{r}U(r)Y_{lm}(\Theta,\phi) \tag{1.22}$$

the wavefunction $\psi(r,\Theta,\phi)$ can be separated into a radial part ($\frac{1}{r}U(r)$) and an angular part of the well-known spherical harmonics $Y_{lm}(\Theta,\phi)$. Equation (1.21) reduces to

$$\left[-\frac{\hbar^2}{2m_e}\left(\frac{\mathrm{d}^2}{\mathrm{d}r^2} + \frac{l(l+1)}{r^2}\right) + V(r)\right]U(r) = E_\psi U(r). \tag{1.23}$$

In the case of the hydrogen atom ($V(r) = -\frac{e^2}{4\pi\epsilon_0 r}$ and $E_\psi = -hc\frac{Ry}{n^2}$) this equation can be solved analytically.
For alkali Rydberg atoms the energies are $E_\psi = -hc\frac{Ry}{(n-\delta_{nlj})^2}$ (1.19) and an effective potential must be employed for $V(r)$ in equation (1.23). This potential is perturbed compared to the Coulomb potential by the core polarization, the screening of the nucleus with $Z \neq 1$ and the spin-orbit interaction of the electron [74]. Taking into account the new effective potential the radial equation (1.23) cannot be solved analytically anymore

to obtain $U(r)$. It has to be integrated numerically from the classically forbidden range at large r to 0 by using the Numerov method [75] or, as it is done by the program *rydLib*, using a Runge-Kutta method [73].
From these wavefunctions transition dipole matrix elements between Rydberg states can be calculated. The dipole operator

$$\hat{d} = -e\hat{r}. \tag{1.24}$$

with the vector components d_x, d_y, d_z in Cartesian coordinates can be expressed in a spherical basis as

$$\begin{aligned} d_+ =& \frac{1}{\sqrt{2}}(d_x + id_y) \\ d_- =& \frac{1}{\sqrt{2}}(d_x - id_y) \\ d_z =& d_z. \end{aligned} \tag{1.25}$$

This representation is more convenient for the description of light-matter interaction. Given the quantization axis z, a photon can have linear or circular polarizations and the interaction with atoms is hence described by d_z or $d_\pm$, respectively.
The dipole matrix elements can be obtained by integration

$$\langle n'l'j'm'_j|\, d_i \,|nljm_j\rangle = 2\pi \int_0^\pi \int_0^r \psi^*_{n',l',j',m'_j}(r,\Theta,\phi) d_i \psi_{n,l,j,m_j}(r,\Theta,\phi) r^2 \sin(\Theta) \mathrm{d}r\mathrm{d}\Theta. \tag{1.26}$$

The wavefunctions are described by quantum numbers n, l, j, m_j and n', l', j', m'_j for the initial and final state, respectively. The integration over ϕ is already carried out as d_i is not depending on ϕ.
Magnetic dipole moments can be calculated similarly from the operator

$$\hat{\mu} = \mu_B \hat{J}, \tag{1.27}$$

where $\hat{J} = \hat{L} + 2\hat{S}$ is the total angular momentum operator.
The calculation of the electric and magnetic dipole matrix elements is performed in the program *rydLib* once and the matrix elements are stored in a database. For calculations of Stark shifts and interaction strength, for example, this database is used in the following. Note that this approach of numerically calculating wavefunctions becomes inaccurate for low-n and ground states. Here only dipole matrix elements between $n > 10$ Rydberg states are calculated.

1.2.3 Characteristics in electric and magnetic fields

To present the influence of electric and magnetic fields on Rydberg atoms I will first treat both fields independently. This gives the best picture to understand the characteristics of Rydberg atoms in weak external fields.
Subsequently I will present the situation in simultaneous electric and magnetic fields, as it can be found in the experiment.

The Stark effect

Rydberg atoms, having a spatially large Rydberg electron wave function, are very sensitive to electric fields and show strong Stark effects. As explained previously, from quantum defect theory follows a lifting of the l-degeneracy for small angular moments. Selection rules for the dipole operator prohibit a coupling between states with the same angular momentum l because of equal parities and second order non-degenerate perturbation theory can be employed for Rydberg states with $l < 4$ for small electric fields. That results in a quadratic Stark effect

$$\Delta E_{Stark} = \sum_{k \neq i} \frac{|\langle \psi_k | \hat{d} \cdot \vec{E} | \psi_i \rangle|^2}{E_k - E_i} = -\frac{1}{2}\alpha |\vec{E}|^2, \tag{1.28}$$

where the subscript i denotes the initial state and the sum ranges over all other states k. As the contribution of every state depends on the difference of the final state energy E_k to the unperturbed initial state energy E_i as $\frac{1}{E_k - E_i}$, usually only some states close by contribute significantly. This second order effect is quadratic in the electric field $\vec{E}$ and can be described by the polarizability α. The polarizability depends on the absolute value of the projection of the total angular momentum on the quantization axis $|m_j|$. In Table 1.2 polarizabilities of the relevant Rydberg and for comparison of the ground state are displayed.
In the case of high angular moments, $l > 4$, no quantum defects exist and degenerate states of opposite parity appear. These states can mix and form eigenstates with a permanent electric dipole moment. There, a linear Stark effect arises in first order perturbation theory.
For electric fields where ΔE_{Stark} is on the order of the energy difference to the next dipole coupled state, the Stark effect cannot be treated perturbatively. Instead, the Stark shifts are determined by diagonalizing the Hamiltonian

$$H = H_0 + H_E \tag{1.29}$$

for different electric fields, where H_0 denotes the eigenenergies of the zero-field Rydberg states and $H_E = \hat{d} \cdot \vec{E}$ is the electric field Hamiltonian. The matrix elements of H_E can be obtained from (1.26). They decrease rapidly as the energy difference between the

state	α ($B = 0\,\mathrm{G}$)	α ($B = 13.55\,\mathrm{G}$)
44 $d_{5/2}$	$85.0(1.6)\,\mathrm{MHz/(V/cm)^2}$	$85.557(1)\,\mathrm{MHz/(V/cm)^2}$
43 $s_{1/2}$	$17.70(13)\,\mathrm{MHz/(V/cm)^2}$	$17.613(3)\,\mathrm{MHz/(V/cm)^2}$
35 $s_{1/2}$	$4.202(36)\,\mathrm{MHz/(V/cm)^2}$	$4.196(6)\,\mathrm{MHz/(V/cm)^2}$
5 $s_{1/2}$	$0.0794(16)\,\mathrm{Hz/(V/cm)^2}$	

Table 1.2: Polarizabilities of the relevant states for this work. The values at the magnetic offset field of 13.55 G originate in fits to calculated Stark effects up to 0.3 V/cm, obtained by diagonalization of the Hamiltonian (1.32). This corresponds to the experimental situation in this work. The polarizabilities for $B = 13.55\,\mathrm{G}$ agree within the error margins with measurements at $B = 0$ [76, 77]. The polarizability of the $5s_{1/2}$ ground state is taken from [78]

initial and final state increases and thus the principal quantum number can be restricted to $n \pm 5$ [73], where n is the state of interest. Furthermore, the dipole operator only couples states with $|\Delta m_j| \leq 1$ and only a limited set of basis states has to be considered. Figure 1.3 shows the dependence of the eigenenergies on the electric field, a so-called Stark-map, in the vicinity of the 44d state. The splitting of the states $l < 5$ is due to the quantum defects. States with $l \geq 5$ are degenerate and show a strong linear Stark effect, resulting in the fan-like Stark structure. In Figure 1.3 (c) the splitting of the 44d states is visible. The absolute value of the magnetic quantum number $|m_j|$ is a good quantum number and the splitted states can be uniquely described.

The Zeeman effect

In a weak magnetic field the Zeeman effect can be treated perturbatively, which leads to the shift

$$\Delta E_Z = g_j m_j \mu_B B, \tag{1.30}$$

with the Landé-factor g_j

$$g_j \approx \frac{3}{2} + \frac{s(s+1) - l(l+1)}{2j(j+1)} \tag{1.31}$$

and the Bohr magneton μ_B. The energy shift is linear in the magnetic field and depending on the projection of the total angular momentum on the quantization axis m_j. Note that the Stark effect is only depending on $|m_j|$.
Rydberg $d_{5/2}$ $m_j = 5/2$ states with $g_j = 6/5$ show a Zeeman shift of $\Delta E_B = 3\,\mu_B B$, which is about 57 MHz at the maximum magnetic field of 13.55 G in this work. This is still smaller than the fine structure splitting between $d_{5/2}$ and $d_{3/2}$ of 137.5 MHz (see Figure 1.3 (c)) and perturbation theory is valid.
Table 1.3 shows the Zeeman shifts of the relevant states in this thesis. Note that in the $5s_{1/2}$ ground state the hyperfine coupling is relevant and f is a good quantum number,

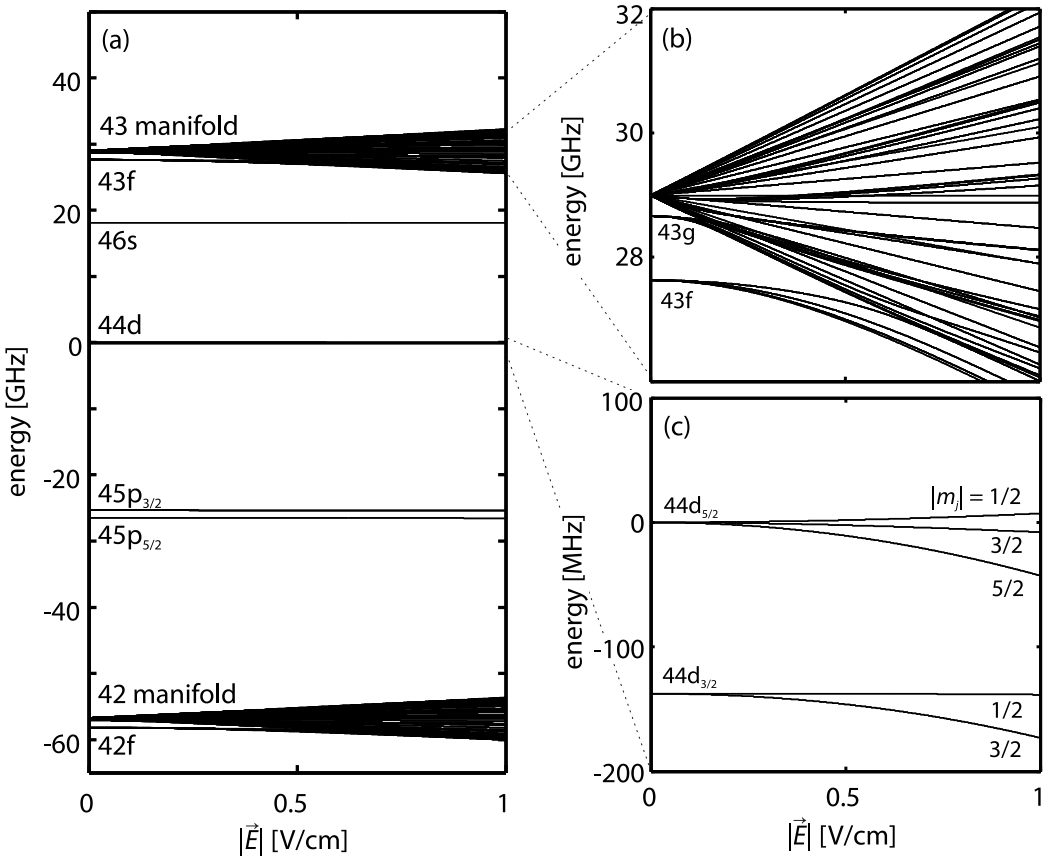

Figure 1.3: Calculated Stark maps in the vicinity of 44d in a pure electric field ($B = 0\,\mathrm{G}$). (a) shows an overview of the Rydberg states. The magnification around the $n = 43$ manifold at 29 GHz (b) shows the linear Stark effect for high-l states. The f and g states with small quantum defects show quadratic shifts for small electric fields and linear shifts for bigger fields. The 44d states (c) show pure quadratic Stark effects. All energies are plotted relative to the energy of the $44\mathrm{d}_{5/2}$ state at $|\vec{E}| = 0$.

whereas in the Rydberg states j is used. The ground state shows the same Zeeman effect as the Rydberg s state and the transition between these states is not magnetic field dependent. In contrast to that, the transition from the ground state to the Rydberg $n\mathrm{d}_{5/2}$ state shows a differential Zeeman effect of $2\,\mu_B B$. That leads to a magnetic field dependent line shift in spectroscopy and to a broadening of the spectroscopy line in an inhomogeneous magnetic field, discussed in chapter 3.
So far, the Zeeman effect was treated perturbatively, valid for the magnetic fields used here. However, in stronger magnetic fields or in combination with electric fields, perturbation theory is not valid. There an exact solution can be obtained by a diagonalization if the magnetic Hamiltonian $H_B = \hat{\mu} \cdot \vec{B}$ with the magnetic dipole operator $\hat{\mu}$ (1.27) is considered. The diagonal elements coincide with the energy shifts from equation (1.30) in the limit of small magnetic fields.

state	m	$g_{j,f}$	ΔE_B
$n\,\mathrm{d}_{5/2}$	$m_j = 5/2$	6/5	$3\,\mu_B B$
$n\,\mathrm{d}_{3/2}$	$m_j = 3/2$	4/5	$6/5\,\mu_B B$
$n\,\mathrm{s}_{1/2}$	$m_j = 1/2$	2	$1\,\mu_B B$
$5\,\mathrm{s}_{1/2}$	$m_f = 2$	1/2	$1\,\mu_B B$

Table 1.3: Zeeman effects for the Rydberg states $n\mathrm{s}_{1/2}$, $n\mathrm{d}_{3/2}$ and $n\mathrm{d}_{5/2}$ (in the basis (n,l,j,m_j)) and for the ground state $5\mathrm{s}_{1/2}$ (basis (n,l,f,m_f)). $1\,\mu_B B$ is approximately $2\pi \times 1.38\,\mathrm{MHz/G}$.

Combined electric and magnetic fields

The situation in combined electric and magnetic fields becomes more complicated and can best be calculated by diagonalizing the full Hamiltonian

$$H = H_0 + H_E + H_B, \tag{1.32}$$

where H_0 is the unperturbed atomic Hamiltonian and H_E and H_B account for the influence of the electric and magnetic field, respectively.
Figure 1.4 shows the eigenenergies obtained at 13.55 G magnetic field, as in the experiments in chapter 3, and a varying electric field. In a pure magnetic field ($|\vec{E}| = 0$) the $44\mathrm{d}_{5/2}$ state splits six fold in m_j (upper six states in Figure 1.4 (a)), the $44\mathrm{d}_{3/2}$ fourfold (lower four states). In a combined electric and magnetic field no generally good quantum numbers exist. Therefore the states in Figure 1.4 are labeled by the quantum numbers of the states they adiabatically connect to in zero electric field.
From a quadratic fit to the numerically obtained Stark shift of the Rydberg state $44\mathrm{d}_{5/2}$, $m_j = 5/2$ between 0 V/cm and 0.3 V/cm a polarizability of $\alpha = 85.557(1)\,\mathrm{MHz/(V/cm)^2}$ is determined. This perfectly agrees with the measured polarizability of $85.0(1.6)\,\mathrm{MHz/(V/cm)^2}$ [77] at $B = 0\,\mathrm{V/cm}$. The small electric fields can be treated as a perturbation even in the presence of a magnetic field as long as the Zeeman shift exeeds the Stark shift. Hence the polarizabilities at 13.55 G and 0 G are the same.
However, in stronger electric fields, when the Zeeman shifts are no longer considerably bigger than the Stark shifts, the situation becomes more complicated. The Stark and Zeeman shifts can have different directions and level crossings between Zeeman split magnetic substates occur at electric fields of about 0.8 V/cm. The electric and magnetic dipole operators do not couple states of different m_j if the quantization axis is collinear to both fields. However, for a finite angle θ_{EB} between the electric field direction and the magnetic field direction the eigenstates of both fields mix. If the quantization axis is chosen to be the magnetic field axis the electric dipole operator has to be expressed

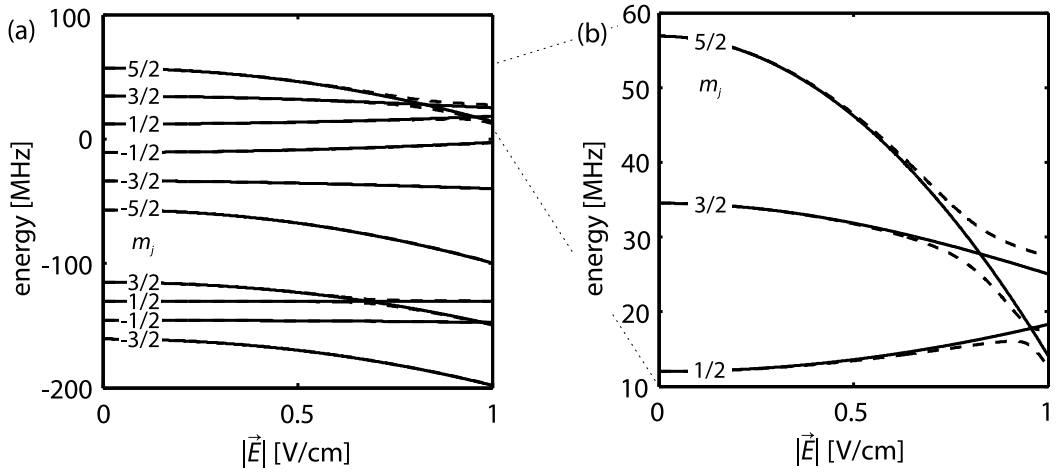

Figure 1.4: (a) Stark map of the $44d_{5/2}$ (upper six states) and $44d_{3/2}$ states (lower four states) at a magnetic offset field of 13.55 G, normalized to the unperturbed $44d_{5/2}$ state at $|\vec{E}| = 0\,\mathrm{V/cm}$ and $B = 0\,\mathrm{G}$. (b) Magnification of the avoided crossings between the $44d_{5/2}$ $m_j = 5/2, 3/2$ and $1/2$ states. The solid lines are calculations for parallel electric and magnetic fields, the dashed lines are under an angle of $\Theta_{EB} = 15°$.

as

$$\hat{d} = d_z \cos\Theta_{EB} + \frac{1}{\sqrt{2}}(d_- - d_+)\sin\Theta_{EB}. \tag{1.33}$$

Additional couplings arise and induce avoided energy level crossings and slightly different Stark effects. The strength of the avoided crossings depend on the angle θ_{EB}.
This effect can be seen in Figure 1.4, where the dashed lines show calculations taking a 15°-angle between the electric and magnetic field into account, and also in the experimental Stark spectra in Figure 3.3. The influence of the misalignment between the electric and magnetic field axis is considerable at the electric field where the Zeeman split states mix. For smaller electric fields almost no effect is visible.

1.3 Binary interactions between Rydberg atoms

Interactions are at the heart of physics, to understand and control them is an ultimate goal in any field of physics. This is especially true for Rydberg atoms, as most proposals including Rydberg atoms are based on their strong interactions. In this chapter I will explain the origin and character of the electric-dipole interaction between two neutral Rydberg atoms and the difference to induced permanent dipole interactions. I will first present a simplified model system, which already reproduces all relevant features and provides an easy understanding of the origin and the character of the Rydberg-Rydberg interaction.
Subsequently I will present more advanced calculations in real many-level systems, tak-

ing angular dependencies into account. These calculations are rather time consuming, therefore I will finally close the circle by introducing again a simplified system that takes a reduced number of states into account and also disregards the angular dependence.

1.3.1 Permanent-dipole interactions

Neutral Rydberg atoms can possess permanent electric dipole moments, given by the slope of the energy of the Rydberg state in an electric field [79], as shown in Figure 1.3. Such a dipole moment generates anisotropic long-range $1/r^3$ dipole-dipole interactions. As noted previously, Rydberg states with angular momentum $l > 4$ are degenerate and can have dipole moments as large as $n^2 e a_0$, where e is the electron charge and a_0 is the Bohr length [80]. This corresponds to huge dipole moments of 4900 Debye[1] for $n = 44$. The dipoles align along the applied electric field and the angular dependence of the interaction U_{perm} is identical to the angular dependence of classical interacting dipoles

$$U_{\text{perm}} = \frac{p_1 p_2}{4\pi\epsilon_0 r^3}(1 - 3\cos^2\Theta), \tag{1.34}$$

where $p_{1,2}$ are the permanent dipole moments of the two interacting atoms and Θ is the angle between the interatomic axis and the direction of the electric field. Even though these interactions can be huge, these high-l states are experimentally difficult to access and not well suited to induce and study interactions.
Low-l Rydberg states do not show a permanent dipole moment in zero electric field. But in an external field additional states of different parity are admixed, inducing the Stark effect and also a electric dipole moment [81]. However, these dipole moments are usually small. In large electric fields the low-l states intersect with the high-l manifold states; for Rydberg states in the vicinity of $n = 44$ this happens at electric fields on the order of 10 V/cm. Near this intersection, states with large electric dipole moments and low angular momentum can be found, that can be excited from the ground state.
Still, several disadvantages appear. The necessary electric fields have to be well controlled, as the atoms are very sensitive to electric field noise or inhomogeneities due to their dipole moments. Especially electric field noise influences the coupling to the manifold states. That leads to a fast distribution of the population over all coupled states and creates unwanted dephasing in coherent experiments. Furthermore, the necessary mixing with the manifold states limits the oscillator strength from the ground state. Due to these reasons, these induced strong dipole moments seem unpractical for coherent experiments.

[1] 1 Debye $= 3.34 \times 10^{-30}$ Cm in SI units

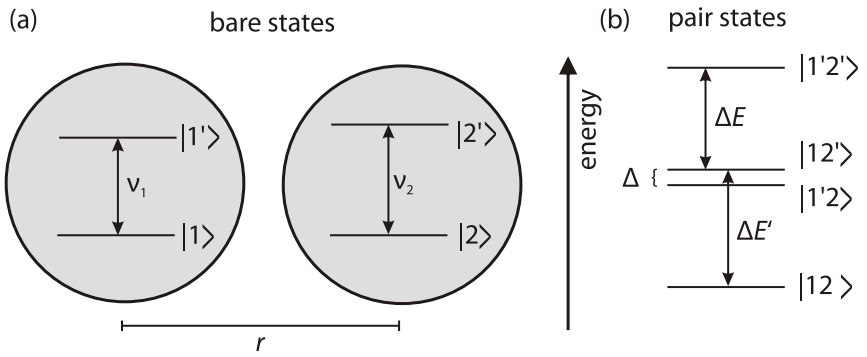

Figure 1.5: (a) Simplified system of two two-level atoms with transition frequencies $\nu_{1,2}$ in a distance r. In the pair state basis four states appear (b). Only two pair states ($|12'\rangle$ and $|1'2\rangle$) are nearly degenerate and show a small energy defect Δ. Atoms in these pair states experience interactions.

1.3.2 The single interaction channel model

Electric dipole interactions are possible even in the absence of an electric field that mixes states of different parity, if a degeneracy in the energy spectrum of dipole-dipole coupled pair states exists. Dipole-dipole coupled means, that the two atoms can be transferred between the pair states by the exchange of photons. Atoms in the near field, where the interatomic distance is smaller than the transition wavelength, exchange no real photons but virtual photon. Because of energy conservation this exchange to first order can only appear in a degenerate pair state system.
Classically speaking, the transition in each atom corresponds to an oscillating electric dipole. This dipole radiates an electric field and the oscillating dipole of the neighboring atom couples to it, resulting in an interaction. This interaction shows many analogies to classical dipole-dipole interaction between permanent dipoles, as explained in the previous chapter. However, it is important to see that here two oscillating dipoles interact. This changes especially the angular dependency of the interaction, as discussed in chapter 1.3.5.
In order to describe binary interactions, i.e. interactions between only two atoms at a time, I consider pair states as a direct product of the single-atom wavefunctions and write $|12'\rangle$ for the pair state, where the first (second) number denotes the state of the first (second) atom. Hence, $|12'\rangle$ is the pair state, where the first atom is in the state 1 and the second atom in the state 2'. The energy of the pair state is the sum of the single-atom energies, $E_{|12'\rangle} = E_{|1\rangle} + E_{|2'\rangle}$. Interactions arise if a second pair state is nearly degenerate, $E_{|12'\rangle} \approx E_{|1'2\rangle}$. These pair states must be dipole-dipole coupled, which means that both transitions, between $|1\rangle \rightarrow |1'\rangle$ and $|2'\rangle \rightarrow |2\rangle$, must be dipole allowed.
In the very simplified system of two two-level atoms, as depicted in Figure 1.5, only two dipole coupled pair states $|12'\rangle$ and $|1'2\rangle$ exist that are nearly degenerate. The

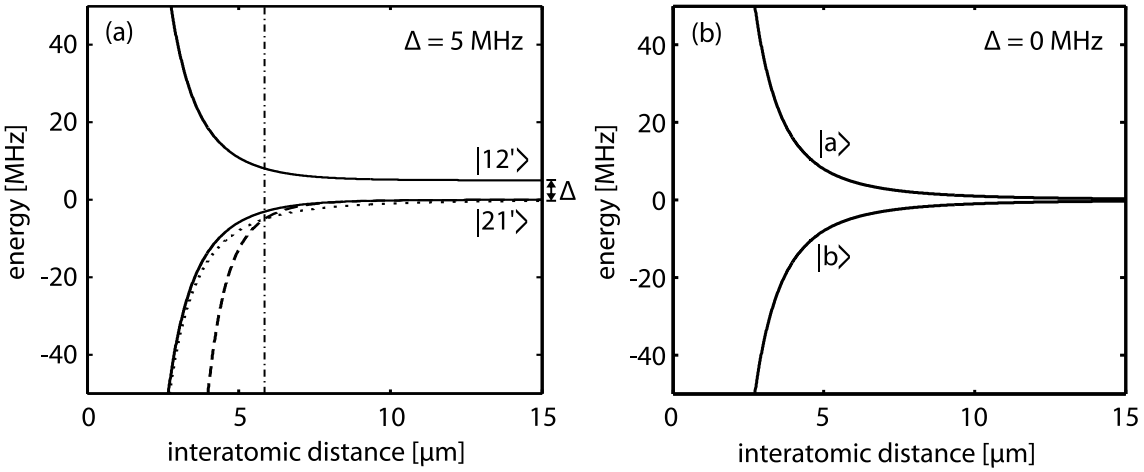

Figure 1.6: Eigenenergies (solid lines) of the two pair states system as a function of the interatomic distance for a finite energy defect $\Delta = 5\,\mathrm{MHz}$ (a) and degenerate pair states $\Delta = 0\,\mathrm{MHz}$ (b) with $C_3 = 1000\,\mathrm{MHz}\mu\mathrm{m}^3$. The dotted line shows a $1/r^3$, the dashed line a $1/r^6$ dependence and the dashed-dotted line indicates the cross over distance r_c. Strictly speaking, the notation in terms of $|12'\rangle$ and $|1'2\rangle$ is only valid in the case of a finite energy defect and infinite interatomic distance.

other two pair states show a large energy difference of $\Delta E, \Delta E' \gg \Delta$ to the initial pair state $|12'\rangle$. Transitions to these pair states are energetically forbidden and only one interaction channel significantly contributes.
In this approximation the system can be described in the basis $(|1'2\rangle, |12'\rangle)$ by the Hamiltonian

$$H = \begin{pmatrix} 0 & U(r) \\ U(r) & \Delta \end{pmatrix}, \tag{1.35}$$

with the coupling strength $U(r) = \frac{C_3}{r^3}$ between $|12'\rangle$ and $|1'2\rangle$ that scales as $1/r^3$. The coefficient C_3 depends on the dipole matrix elements between the pair states and will be described and calculated in detail later in chapter 1.3.5. $\Delta = E_{|12'\rangle} - E_{|1'2\rangle}$ is the energy defect of the pair states.
This Hamiltonian can analytically be diagonalized to obtain the eigenenergies

$$\lambda_{1,2} = \frac{1}{2}(\Delta \pm \sqrt{\Delta^2 + 4U^2}). \tag{1.36}$$

Figure 1.6 shows the distance dependent potential curves between the atoms. Two branches are visible, where the interaction-induced energy shift differs in its sign. The energy of one branch increases with decreasing interatomic distance (blue). The force, as the derivative of the potential curve, points towards bigger interatomic distances in this case, resulting in a repulsive interaction between the atoms. The other branch (red) shows an attractive interaction. From equation (1.36) two limits are especially interesting and will be inspected in the following.

- $\boldsymbol{\Delta \ll U}$ In the case of nearly degenerate states the eigenenergies are $\lambda_{1,2} = \pm U$. This results in resonant $1/r^3$-dipole-dipole interaction that is expressed in the distance dependent energy shift. The attractive and repulsive interacting eigenstates in this limit are $|a\rangle = \frac{1}{\sqrt{2}}(|12'\rangle + |21'\rangle)$ and $|b\rangle = \frac{1}{\sqrt{2}}(|12'\rangle - |21'\rangle)$. In Figure 1.6 (b) these states are plotted as a function of the interatomic distance in the case of $\Delta = 0$, when the approximation of resonant dipole-dipole interaction is valid for all distances.

- $\boldsymbol{\Delta \gg U}$ In the limit of large defects Δ the eigenstates remain almost unperturbed and the eigenenergies are $\lambda_1 = \Delta + \frac{U^2}{\Delta}$ and $\lambda_2 = -\frac{U^2}{\Delta}$. Both states scale as $1/r^6$ with the interatomic distance. This is the limit of van der Waals interaction or induced dipole interaction that can also be calculated from second order perturbation theory when the interaction is treated as a small perturbation.

In Figure 1.6 (a) both limits are indicated by the dashed and the dotted lines. For a finite energy defect the states show a van der Waals interaction at large internuclear distances, when $\Delta \gg U$ is fulfilled. With smaller distances the coupling strength $U(r) = C_3/r^3$ rises and the system eventually reaches the limit of resonant dipole-dipole interaction ($U(r) \gg \Delta$).
The transition from van der Waals to dipole-dipole interaction appears when the coupling strength equals the energy defect, $U \approx \Delta$. The crossover distance r_c can thereby be defined as

$$r_c = \sqrt[3]{\frac{C_3}{\Delta}}. \tag{1.37}$$

The dashed-dotted line in Figure 1.6 (a) indicates this distance. For $\Delta = 0$ (Figure 1.6 (b)) the interaction is entirely of dipole-dipole character and no transition appears.

1.3.3 Förster resonances

Previously we saw that strong interactions can arise if dipole coupled pair states are degenerate. That can happen whenever two degenerate dipole transitions couple non-radiatively in atoms, molecules or even more complex biological objects and is called a Förster resonance. In biological systems this leads to the Förster resonant energy transfer (FRET), responsible for the efficient and fast energy transport in photosynthesis.
Similar Förster resonances can also be found in atoms. As radiation less couplings, Förster resonances appear only in the near field when the wavelength of the transition λ is longer than the interparticle distance r. At typical length scales of up to some tens of μm in ultra-cold atoms this corresponds to transition frequencies below 10 THz to fulfill the near field approximation. Transitions from the atomic ground state can typically not realize non-radiative dipole couplings. In Rydberg states, however, the

transition frequencies are in the microwave range, deep in the near field limit, and Förster resonances can occur.
In the simplest case consider one atom in a Rydberg ns state and the other atom in a np state. Then, dipole-dipole transitions can exchange the energy between the atoms

$$n\mathrm{p} + n\mathrm{s} \leftrightarrow n\mathrm{s} + n\mathrm{p}. \tag{1.38}$$

The two oscillating dipoles between ns and np couple and induce an interaction. This transition is always, independent of external fields, exactly resonant.
However, experimentally this situation is difficult to realize as the atoms have to be prepared in different states. Similar resonances can also appear between different atomic states, if the corresponding pair states are degenerate. In this case, the oscillating transition dipoles of the two interacting atoms are in general different in the polarization, in contrast to usual Förster resonances, but still induce interactions between the atoms. Despite the typographical error in their paper [31], we follow Walker and Saffman and also call these resonances Förster resonances in analogy to the FRET processes.
Due to the lifting of the l-degeneracy by the quantum defects in low-l Rydberg states accidental pair degeneracies are unlikely. But several possibilities exist to tune the pair states into resonance. That can happen by radio-frequency fields [25], microwave fields [17] or AC-Stark effects [82]. In these approaches an oscillating field realizes the control parameter for tuning the resonances and they require an additional radio-frequency or microwave source. Spatially resolved control of these fields to control the interaction is challenging.
DC-Stark shifts [16] by small electric fields can also tune pair states into degeneracy. The use of Stark-tuned Förster resonances offers many advantages, such as easy tunability and small technical effort to generate the static electric field that serves as a control parameter. They are widely used and have been studied in many laboratories for more than 30 years. They are also used in the experiments of this thesis and I will concentrate on them in the following.
The pronounced Stark shift of Rydberg states and its dependence on the internal state allows tuning the energy defect between pair states, in the context of Förster resonances called Förster defect, by static electric fields. Many possible pair states can be used, but outstanding is the Förster resonance

$$44\mathrm{d}_{5/2} + 44\mathrm{d}_{5/2} \rightarrow 46\mathrm{p}_{3/2} + 42\mathrm{f} \tag{1.39}$$

in ^{87}Rb. First of all, ^{87}Rb is well known in ultra-cold physics and easily controllable. This particular Förster resonance is furthermore advantageous as it appears at small electric fields, it is well separated from other resonances and it allows preparing the atoms in one single state that is accessible by two-photon excitation.
Figure 1.7 shows the Stark map and an energy level diagram of the relevant states at 13.55 G magnetic offset field, as it is used in the experiment. The $44\mathrm{d}_{5/2}$ state lies

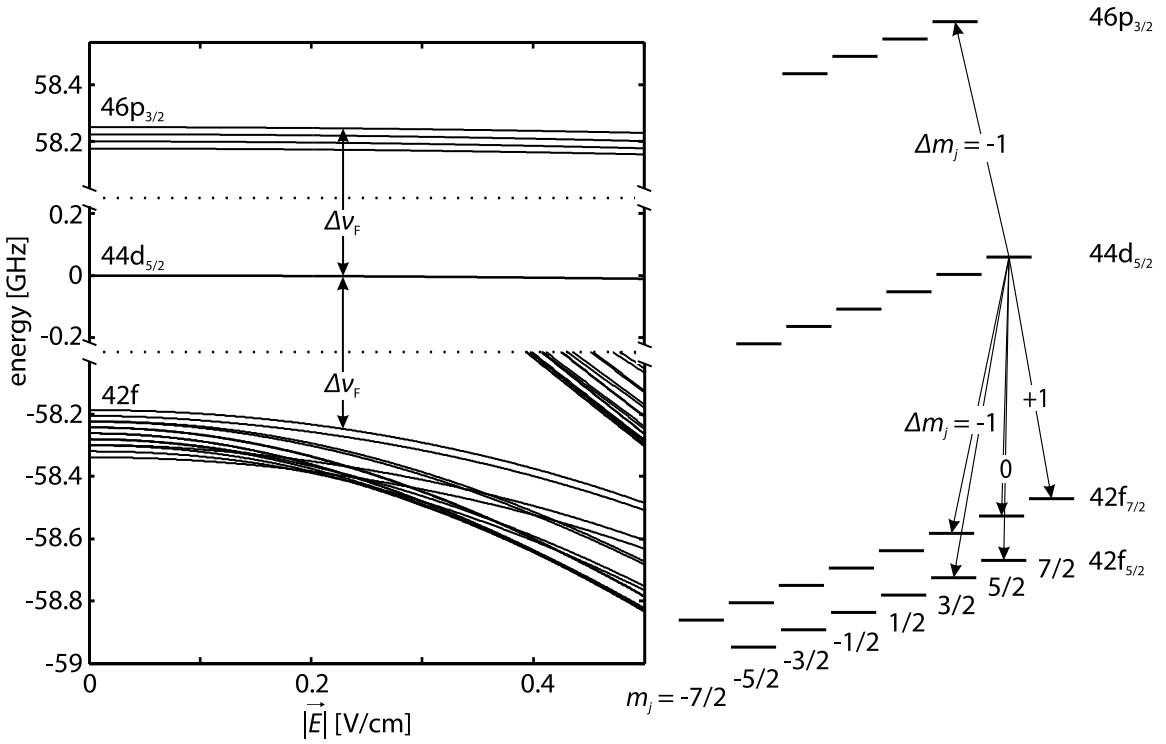

Figure 1.7: Stark map of the relevant single-atom states for the discussed Förster resonance at 13.55 G magnetic offset field, aligned parallel to the electric field. The 44d states are approximately midway between the dipole coupled 42f and 46p states. The transition frequencies at 0.231 V/cm, marked by the vertical arrows, are $\Delta\nu_{\mathrm{F}} = 58.248\,\mathrm{GHz}$. The right side shows an energy level diagram of the Zeeman split states and the possible transitions from the $44\mathrm{d}_{5/2}$, $m_j = 5/2$ state. Note that the shown Zeeman split states are no eigenstates in combined magnetic and electric fields.

approximately midway between the 42f and the 46p states. Especially due to the 42f Stark effect of about $2\,\mathrm{GHz/(V/cm)^2}$, that clearly exceeds all other Stark effects, the transition frequencies $\Delta\nu_{\mathrm{F}}$ shift in the electric field. The frequency of about 58.2 GHz corresponds to a wavelength of 5 mm that exceeds all other length scales in a typical ultra-cold atom experiment and allows for non-radiative coupling.

Due to the magnetic offset field the magnetic substates split. The energy level diagram in Figure 1.7 shows this splitting. Starting from the $44\mathrm{d}_{5/2}$, $m_j = 5/2$ state, as it is done in the experiments in this thesis, only one of the 46p states is coupled, namely $46\mathrm{p}_{3/2}$, $m_j = 3/2$. However, dipole coupling to several 42f states is allowed. The transition dipoles to these magnetic substates differ in the polarization. Different angular dependencies arise, which will be discussed in chapter 1.3.5. The description in the energy level diagram in Figure 1.7 is only valid in a pure magnetic field. In combined electric and magnetic fields the energy levels shown will be mixed.

Figure 1.8 shows the energy levels of the pair states from equation (1.39), using the

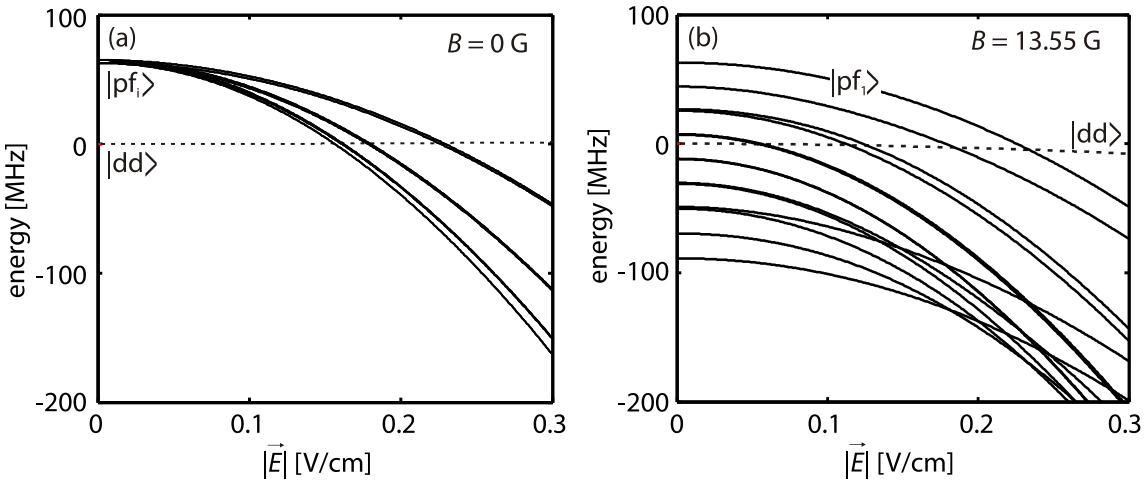

Figure 1.8: (a) Stark map for the relevant pair states (see text) in zero magnetic field. (b) shows the Stark map at a magnetic offset field of 13.55 G aligned parallel to the electric field. The dashed line is the $2{\cdot}(44\mathrm{d}_{5/2}, m_j = 5/2)$ pair state, the solid lines are the $(46\mathrm{p}_{3/2}, m_j = 3/2)$ + 42f pair states.

notation $|dd\rangle$ for two atoms in the $44\mathrm{d}_{5/2}$, $m_j = 5/2$ state and $|pf_i\rangle$ for the state $(46\mathrm{p}_{3/2}$, $m_j = 3/2)$ + 42f. Different Stark and Zeeman effects of the involved single-atom 42f states induce a splitting into several $|pf_i\rangle$ pair states, indicated by the subscript i. In zero magnetic and electric field the Förster defect $\Delta_i = E_{|pf_i\rangle} - E_{|dd\rangle}$, the energy difference between the pair states, is 65 MHz (see Figure 1.8 (a)). At certain electric fields the $|dd\rangle$ state becomes degenerate with a $|pf_i\rangle$ state and a Förster resonance arises.
In an additional magnetic field, shown in Figure 1.8 (b), the Zeeman effect shifts the pair states in zero electric field. As the Stark effect is unidirectional, some pair states cannot be shifted into resonance by the additional electric field. However, different magnetic substates $|pf_1\rangle$ - $|pf_6\rangle$ are tuned into resonance at different electric fields (0.234, 0.184, 0.127, 0.115, 0.058, 0.055 V/cm), leading to several distinct resonances. The involved single-atom f states are no eigenstates of $\hat{J}_z$ in the combined magnetic and electric fields and cannot be uniquely described by the quantum numbers l,j and m_j. Figure 1.9 shows the fractional composition of the states in the respective fields of the Förster resonances. The resonance in the highest electric field at 0.234 V/cm, $|pf_1\rangle$, is an almost pure $(46\mathrm{p}_{3/2}, m_j = 3/2) + (42\mathrm{f}_{7/2}, m_j = 7/2)$ state, as it is the stretched configuration where all spins are aligned in parallel. The other states are widely mixed. However, I will denote these states by $|pf_i\rangle$ in the following even though they are no eigenstates in l,j and m_j. The involved p and d states remain almost pure states and do not change their character.
The magnetic field dependence of the electric fields necessary to tune the pair states into resonance is shown in detail in Figure 1.10 by the solid lines. The dots indicate the interaction strength of the resonances, that will be calculated in chapter 1.3.5. The color

and the diameter of the dots, that linearly increases with the strength of the resonance, show the angular maximum of the interaction strength U_{max}. Some pair states can be tuned into resonance by a certain electric field, but as the involved states are not dipole coupled they do not induce interactions. This can be seen by the solid lines that have no additional dots.
In zero magnetic field four resonances appear. This can be understood if the fine structure splitting of the f state is omitted [79]. In a basis formed of magnetic quantum numbers for electron spin and orbital angular momentum of the f state ($|m_s, m_l\rangle$) the pair states that couple to $|dd\rangle$ at $B = 0\,\mathrm{G}$ can be identified as $|\frac{1}{2}, 3\rangle$,$|\frac{1}{2}, 2\rangle$ and $|\frac{1}{2}, 1\rangle$ for the resonances at $|\vec{E}| = 0.234\,\mathrm{V/cm}$, $|\vec{E}| = 0.182\,\mathrm{V/cm}$ and $|\vec{E}| = 0.164\,\mathrm{V/cm}$, respectively. The state $|\frac{1}{2}, 0\rangle$ at $|\vec{E}| = 0.159\,\mathrm{V/cm}$ is not coupled to $|dd\rangle$ and hence does not induce interactions. This is visible in Figure 1.10 by the lacking dot, describing the strength of the interaction. Differences to [79] arise due to slightly different quantum defects used, predominantly by the g quantum defect that was not considered before.
The magnetic field leads to shifts of the resonant electric fields and to additional and stronger splitting of the resonance, advantageous to resolve and individually address the resonances. The resonance at $0.234\,\mathrm{V/cm}$ is not shifted by the magnetic field. It is an almost pure, maximally aligned state consisting of ($46\mathrm{p}_{3/2}$, $m_j = 3/2$) and ($42\mathrm{f}_{7/2}$, $m_j = 7/2$). Upon inserting $m_j = j$ into equations (1.30) and (1.31) the Zeeman shift can be calculated for maximally aligned states to be $\Delta E_B = (l + 2s) \cdot \mu_B B$. Hence Förster resonances of the type

$$n, l + n, l \rightarrow n'(l + 1) + n''(l - 1) \tag{1.40}$$

do show magnetic field independent resonances between the maximally aligned states. Not maximally aligned states show complicated shifts in combined electric and magnetic fields and accidental magnetic field independent resonances are unlikely. In the case of resonances like

$$n, l + n, l \rightarrow n'(l \pm 1) + n''(l \pm 1), \tag{1.41}$$

e.g. between $37\mathrm{p}_{3/2}$+$37\mathrm{p}_{3/2}$ and $37\mathrm{s}_{1/2}$+$38\mathrm{s}_{1/2}$ [24], the maximally aligned states do not show magnetic field independent resonances.
The predominant source of inaccuracy in these calculations is the g quantum defect, which is not precisely known for the 42g state relevant here. The only measured value is the g quantum defect for ^{85}Rb $n = 30$ [71]. In table 1.4 the dependence of the calculated Förster resonance positions on the g quantum defect is shown. The difference of about 15% is notable and a precise knowledge of the correct quantum defect would be necessary for accurate predictions of the Förster resonance positions.
Comparing the electric fields of the Förster resonances to the single-atom level crossings in Figure 1.4, where single-atom diabatic losses may occur, one can see that at $13.55\,\mathrm{G}$ these crossings at $0.8\,\mathrm{V/cm}$ are far outside the experimentally relevant electric field range

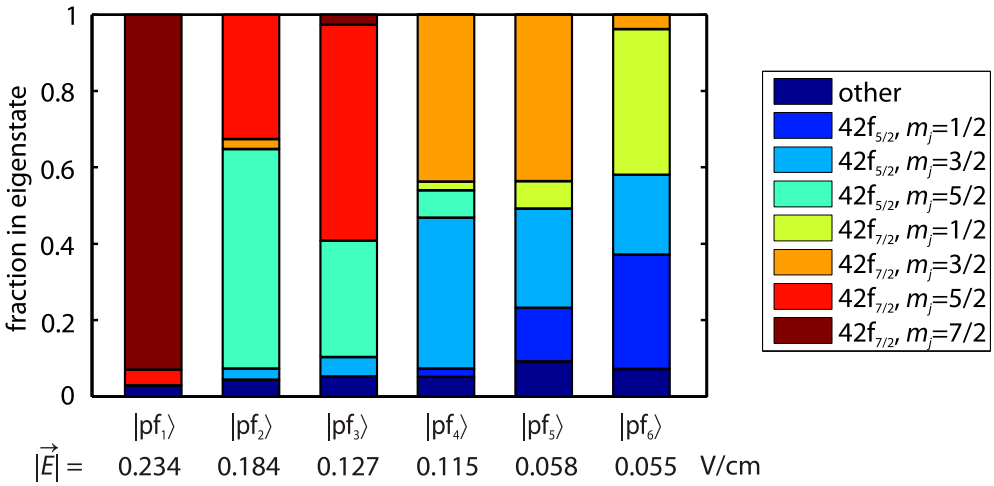

Figure 1.9: Fractional composition of the involved f state in the pair states at the respective electric fields where they are tuned into resonance.

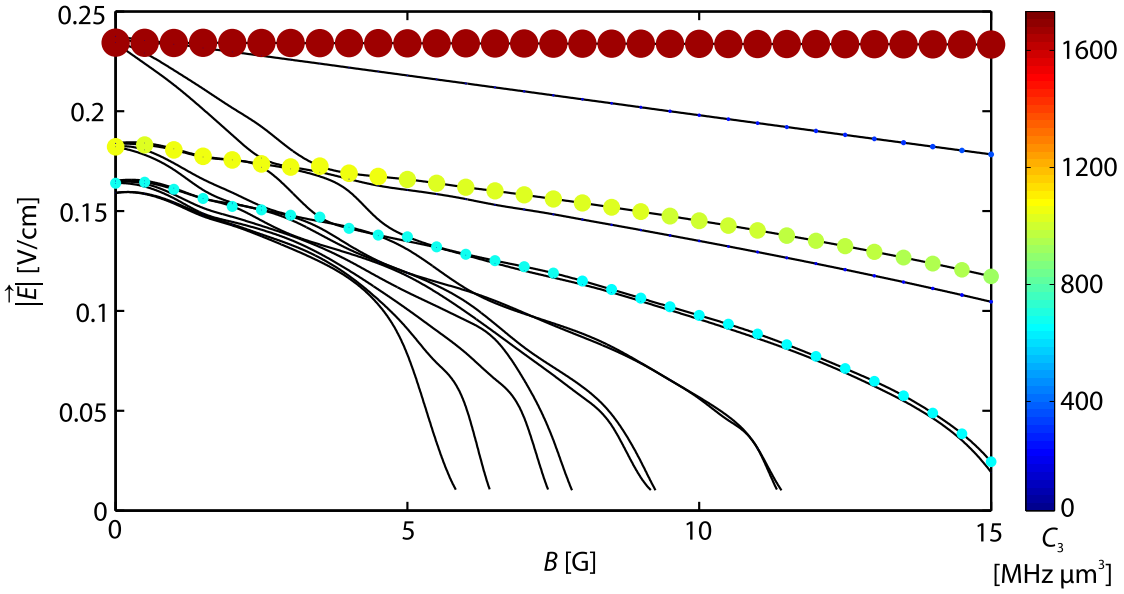

Figure 1.10: Magnetic field dependence of the electric fields $|\vec{E}|$ required to tune the pair states into Förster resonance for parallel magnetic and electric field (dots and lines). The angular maximum of the interaction strength U_{max} of the resonances is indicated by the color and the diameter of the dots, that linearly increases with the strength of the resonance. The strongest resonance is at $|\vec{B}| = 0\,\mathrm{G}$ and $|\vec{E}| = 0.234\,\mathrm{V/cm}$ with a strength of $1556\,\mathrm{MHz}{\cdot}\mu\mathrm{m}^3$.

	electric fields [V/cm]					
$\delta_g = 0.00405$ [71]	0.234	0.184	0.127	0.115	0.058	0.055
$\delta_g = 0$	0.266	0.210	0.146	0.132	0.066	0.062

Table 1.4: Comparison of the calculated electric fields to tune pair states into Förster resonance with and without a quantum defect of the g states.

for the Förster resonances of below 0.3 V/cm. However, at smaller offset magnetic fields below 4 G both effects arise at similar electric fields. Therefore this particular Förster resonance has to be studied either in absence of a magnetic field or at strong enough magnetic offset fields.

1.3.4 The dipole-dipole interaction operator

The strength of the interaction between two neutral atoms, having oscillating electric dipole moments, can be calculated as a coupling between the radiated field of one atom and the dipole moment of the second atom. Atom 1 with an oscillating transition dipole moment $\vec{d_1}(t) = \vec{d_1}e^{-i\omega t}$, where $\hbar\omega$ is the transition energy, radiates an electric dipole field $\vec{E_1}(\vec{r}, t)$. This fields interacts with the electric dipole moment of atom 2 to give the interaction energy $\vec{E_1}(\vec{r}) \cdot \vec{d_2}(t)$. The energy can be expressed in multipole expansion, in leading order as the dipole-dipole interaction [83, 84]

$$U(r) = \frac{1}{4\pi\epsilon_0} \frac{\vec{d_1} \cdot \vec{d_2} - 3(\vec{n} \cdot \vec{d_1})(\vec{n} \cdot \vec{d_2})}{r^3}, \tag{1.42}$$

where r is the internuclear distance and $\vec{n}$ the unit vector connecting the atoms (see Figure 1.11). This approximation is valid in the near field of the oscillating dipole where the internuclear distance is considerably smaller than the wavelength of the transition and when the electron wavefunctions of the two atoms do not overlap. The dipolar interaction resembles the classical dipole-dipole interaction between permanent dipole moments, which leads to the interaction (1.34) if aligned along the electric field.
In a quantum mechanical analog the dipole moment $\vec{d}$ is exchanged by the dipole operator $\hat{d}$ to obtain the quantum mechanical dipole-dipole interaction, following the calculations from Reinhard et al. [79]. For the geometry depicted in Figure 1.11, the dipole operator can be expressed in the spherical basis d_+, d_-, d_z (equations (1.25)), using

$$\vec{n} = \sin\Theta\vec{e}_x + \cos\Theta\vec{e}_z \tag{1.43}$$

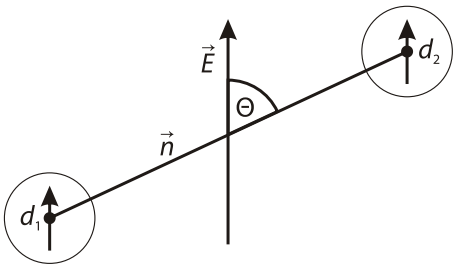

Figure 1.11: Geometry of the considered two-atom system with dipole moments $d_{1,2}$ and the quantization axis along the electric field $\vec{E}$.

with the unit vectors $\vec{e}_{x,z}$. One obtains for the dipole-dipole interaction operator V_{dd}

$$\begin{aligned} V_{\mathrm{dd}} =& \frac{1}{4\pi\epsilon_0}\frac{\hat{d}_1\cdot\hat{d}_2 - 3(\vec{n}\cdot\hat{d}_1)(\vec{n}\cdot\hat{d}_2)}{r^3} \\ =& \frac{1}{4\pi\epsilon_0}\frac{d_{1+}d_{2-} + d_{1-}d_{2+} + d_{1z}d_{2z}(1-3\cos^2\Theta)}{r^3} \\ &- \frac{\frac{3}{2}\sin^2\Theta(d_{1+}d_{2+} + d_{1+}d_{2-} + d_{1-}d_{2+} + d_{1-}d_{2-})}{r^3} \\ &- \frac{\frac{3}{\sqrt{2}}\sin\Theta\cos\Theta(d_{1+}d_{2z} + d_{1-}d_{2z} + d_{1z}d_{2+} + d_{1z}d_{2-})}{r^3}. \end{aligned} \tag{1.44}$$

The first subscript $k = 1, 2$ indicates the atom, the second subscript indicates the polarization of the oscillating dipole moment that can be circular $(+, -)$ or linear (z) polarized. The operator V_{dd} acts on pair states $|12\rangle$ and the coupling strength in dipole-dipole approximation between two pair states can be expressed by the corresponding matrix element of the dipole-dipole interaction operator.
These matrix elements are also relevant for the calculation of binary interactions, as will be explained in the following sections. Each term

$$\langle 1'2|\, d_{1i}d_{2j}\, |12'\rangle = \langle 1'|\, d_{1i}\, |1\rangle\, \langle 2|\, d_{2j}\, |2'\rangle \tag{1.45}$$

of the matrix elements of V_{dd}, involving products of single-atom matrix elements $\langle k'|\, d_{ki}\, |k\rangle$ (1.26), describes the coupling between two oscillating dipoles of polarization i and j $(i, j = +, -, z)$. This polarization is given by the polarization of the corresponding transitions, depending on the magnetic quantum numbers involved as shown in the energy level diagram in Figure 1.7. However, the good quantization axis for the polarization of the oscillating dipoles is the interatomic axis and not necessarily the quantization axis of the atoms, given by the external field.
In the case of $\Theta = 0$ the interatomic axis and the external field axis are parallel. Then a unique correspondence between the magnetic quantum numbers and the polarization of the transition exists. Transitions with $\Delta m_j = +1, -1, 0$ show non-zero matrix elements only of d_+, d_-, d_z, respectively. In the case of a finite angle Θ this correspondence is not fulfilled and the interpretation of the coupling becomes more involved.

1.3.5 Resonant dipole-dipole interaction

In the case of degenerate dipole-dipole coupled pair states, resonant dipole-dipole interaction occurs. That can be seen as resulting from first order perturbation theory, leading to the interaction strength

$$U_{\mathrm{dd}} = \pm \langle 1'2 | \, V_{\mathrm{dd}} \, | 12' \rangle \,, \tag{1.46}$$

with the dipole-dipole interaction operator V_{dd} (1.44). Diagonalization of the Hamiltonian of the single interaction channel model (1.35) results in the same interaction strength.

Resonant dipole-dipole interaction due to the Förster resonance (1.39) occurs only when the pair states are shifted into exact resonance, for example by small electric fields. Hence, to calculate the strength and the angular dependence of the Förster resonance the eigenstates in the electric field, where the pair states are tuned into resonance, must be calculated (see Figure 1.9). From these eigenstates the interaction can be calculated for every Förster resonance simultaneously, similar to equation (1.46). Since it is not possible to differenciate between the two alike atoms the coupled pair state is $\frac{1}{\sqrt{2}}(|pf_i\rangle + |f_ip\rangle)$, with the degenerate states $|pf_i\rangle$ and $|f_ip\rangle$. The antisymmetric combination of pair states does not lead to an interaction. This results in

$$\begin{aligned} U_{\mathrm{dd}} &= \pm \frac{1}{\sqrt{2}} (\langle pf_i| + \langle f_ip|) V_{dd} \, |dd\rangle \\ &= \pm \sqrt{2} \, \langle pf_i| \, V_{dd} \, |dd\rangle \,, \end{aligned} \tag{1.47}$$

which can be expressed as $U_{\mathrm{dd}} = \pm \frac{C_3}{r^3}$ with the C_3-coefficient as in the single interaction channel model (1.35). The sign is given by the phase between $|pf_i\rangle$ and $|dd\rangle$. Figure 1.10 shows this strength of the resonances. The resonance at the highest electric field shows the strongest interaction.

The θ-dependence of the operator V_{dd} results in an angular dependence of the strength of the dipole-dipole interaction, that is plotted in Figure 1.12 at the distinct electric fields where the Förster resonances occur. Different angular symmetries are visible for the different resonances.

Let's focus on the simple configuration where the atoms are aligned along their quantization axis, i.e. $\Theta = 0$. The transition between $44\mathrm{d}_{5/2}$ and $46\mathrm{p}_{3/2}$ is always $\Delta m_j = -1$ (cp. Figure 1.7) and only terms including at least one $d_{k,-}$ in the interaction operator (1.44) contribute. Furthermore, since $\Theta = 0$, most other terms drop out and we are left with

$$\langle pf| \, V_{\mathrm{dd}} \, |dd\rangle = \frac{1}{4\pi\epsilon_0} \, \langle pf| \, \frac{d_{1-}d_{2+} + d_{1+}d_{2-}}{r^3} \, |dd\rangle \,. \tag{1.48}$$

Interpreting this equation we see that only transitions where one atom is excited to $42\mathrm{f}_{7/2}$, $m_j = 7/2$ and the other atom to $46\mathrm{p}_{3/2}$, $m_j = 3/2$ are allowed as they are the

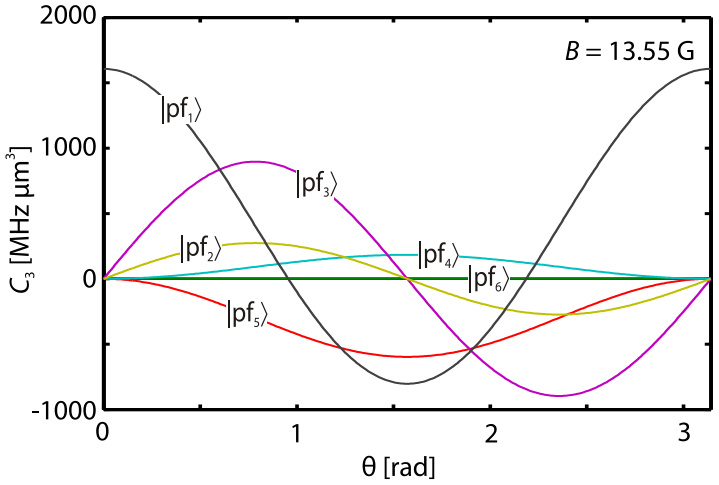

Figure 1.12: Angular dependence of the strength of the resonant dipole-dipole interaction at 13.55 G magnetic offset field along the quantization axis at the respective electric fields to tune the pair states into resonance.

only transitions with both, $\Delta m_j = +1$ for one atom and $\Delta m_j = -1$ for the other atom. This can also be seen from angular momentum conservation. One transition with $\Delta m_j = -1$ demands another transition with $\Delta m_j = +1$ to preserve the angular momentum.
Figure 1.9 shows that only resonance $|pf_1\rangle$ is dominantly composed of the $42f_{7/2}$, $m_j = 7/2$ state and induces an interaction at $\Theta = 0$, visible in Figure 1.12. It shows the same angular dependence ($\propto 1 - \frac{3}{2}\sin^2\Theta$) as the classical dipole interaction between permanent dipoles and shows no interaction under an angle of 54.7°, called the magic angle. Integration over the full solid angle results in zero interaction, which means that a homogeneous infinite sample at this Förster resonance does not experience an energy shift due to the interaction.
For a finite angle Θ the polarization axis of the oscillating dipoles is not identical with the quantization of the atoms and the connection between Δm_j and the polarization of the dipole moments becomes complicated. Other transitions are allowed where the projection of the angular momentum onto the quantization axis is not conserved and additional resonances appear. Some of these resonances show an angular dependence that does not result in zero when integrating over the full solid angle, namely $|pf_4\rangle$ and $|pf_5\rangle$.

1.3.6 van der Waals interaction

When no degenerate pair states exist, interactions can be calculated from second order perturbation theory and van der Waals interaction occurs. As already seen in the single interaction channel model the energies of the pair states depend on $\frac{U^2}{\Delta}$ and scale as $1/r^6$.

In many-level atoms these contributions from every single interaction channel have to be summarized, leading to the van der Waals interaction U_{vdW}

$$U_{\mathrm{vdW}} = -\sum_{k''k'} \frac{|\langle k''k'|\, V_{\mathrm{dd}}\, |kk\rangle\,|^2}{\Delta_{k''k'}}, \tag{1.49}$$

expressed as an interaction-induced energy shift of the pair states. $|k''k'\rangle$ denotes all pair states that are dipole-dipole coupled to the initial pair state $|kk\rangle$ and $\Delta_{k''k'} = E_{|k''k'\rangle} - E_{|kk\rangle}$ is the infinite separation energy defect between the pair states. In the presence of magnetic and electric fields the pair states consist of single-atom eigenstates in the respective field. Since $V_{\mathrm{dd}} \propto 1/r^3$ follows $U_{\mathrm{vdW}} \propto 1/r^6$. The van der Waals interaction is often expressed as $U_{\mathrm{vdW}} = -\frac{C_6}{r^6}$ with the van der Waals-coefficient C_6 describing the strength of the interaction.
The contribution of every single interaction channel scales as $1/\Delta$ and usually only some energetically close by pair states contribute significantly. In the calculations here only interaction channels with $|\Delta| < 10\,\mathrm{GHz}$ are considered. Furthermore, as the single-atom matrix elements $\langle k'|\, d_i\, |k\rangle$ decrease rapidly with increasing energy difference between initial and final state, the calculations are restricted to principal quantum numbers $n \pm 5$ around the quantum number n of the initial state. j and m_j can also be limited to $j, m_j \leq 11/2$ as dipole transitions couple only $l' = l \pm 1, 0$. In the case of van der Waals interaction of the $44\mathrm{d}_{5/2}$ state this reduces the relevant pair states to about 40000. Especially close to a Förster resonance, where some pair states are nearly degenerate, the system can be severely reduced, as it is done in chapter 1.3.7.
The calculated van der Waals interaction of two atoms in the $44\mathrm{d}_{5/2}$, $m_j = 5/2$ state as a function of the angle Θ between the interatomic axis and the quantization axis is shown in Figure 1.13. In zero electric field the interaction-induced energy shift is negative, i.e. the van der Waals interaction is attractive, and the interaction is almost isotropic in the angle Θ. Close to the Förster resonance at $0.234\,\mathrm{V/cm}$ (see Figure 1.8) however a pronounced angular dependence is visible and the interaction is clearly enhanced under some angles. Additionally the interaction changes from attractive below the resonance at $0.2\,\mathrm{V/cm}$ to repulsive above the resonance at $0.26\,\mathrm{V/cm}$.
The angular dependence can be understood from the following: Close to the Förster resonance only one interaction channel dominates. All other terms in the sum (1.49) result in an almost isotropic background. The dominant term accounts for the strong and anisotropic interaction proportional to $|U_{\mathrm{dd}}|^2$. Hence the van der Waals interaction close to a Förster resonance mirrors the angular dependence of the dipole-dipole interaction at resonance squared (see equation (1.47) and Figure 1.12).
The strength of the van der Waals interaction for different angles is shown in Figure 1.14 as a function of the electric field. At the electric fields where the Förster resonances appear, as calculated in chapter 1.3.3, the van der Waals interaction diverges. The change of the interaction from attractive at electric fields smaller than the electric field

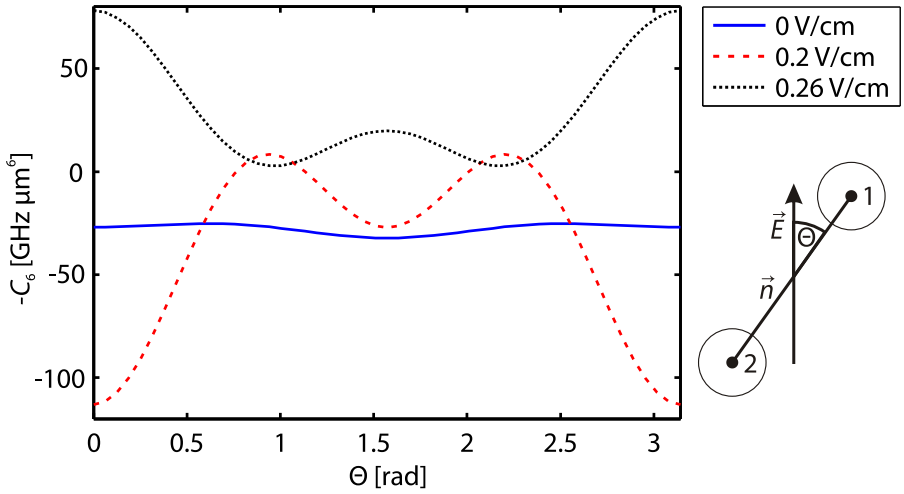

Figure 1.13: Calculated angular dependent van der Waals interaction for two atoms in the $44d_{5/2}$, $m_j = 5/2$ state at 13.55 G magnetic offset field for zero electric field and electric fields close to the Förster resonance of $|pf_1\rangle$ ($\vec{E} \parallel \vec{B}$).

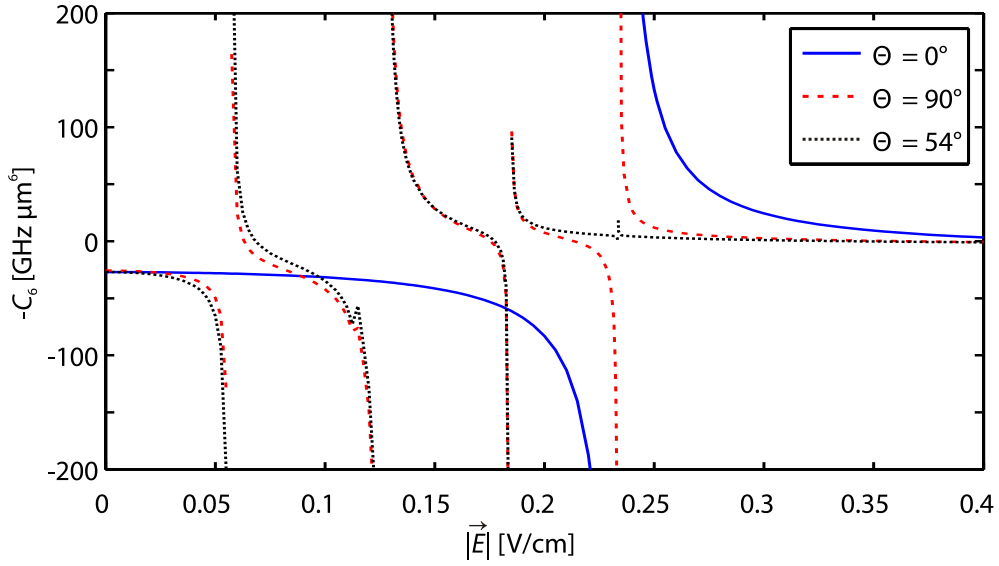

Figure 1.14: Electric field dependence of the strength of the van der Waals interaction for $\Theta = 0°$ and 90° and close to the magic angle of 54.7° at 13.55 G magnetic offset field.

of the Förster resonance to repulsive at higher fields is again visible in the sign of the energy shift.
When the atoms are aligned along the fields ($\Theta = 0$) only one resonance appears because of angular momentum conservation, as in the case of resonant dipole-dipole interaction. Under the magic angle of 54.7° the resonance in the highest electric field does not appear. In Figure 1.14 a very small signal at 0.234 V/cm is visible since the calculation was done at 54°, not exactly at the magic angle.
Care has to be taken here as these calculations are results of a perturbative approach. When the interaction strength $-C_6/r^6$ equals the energy defect a cross-over to the dipole-dipole interaction occurs (chapter 1.3.2) and equation (1.49) is no longer valid. This cross-over is a function of the interatomic distance and of the electric field. The van der Waals interaction provides good results for large interatomic distances and large energy defects only, i.e. detuned in the electric field from the Förster resonances. Close to the resonances, where the van der Waals interaction strength diverges, the perturbative approach fails and the results in Figure 1.14 are not correct.

1.3.7 Full diagonalization of the essential pair state system

Close to the Förster resonance the number of relevant states can be greatly reduced, because only a limited number of interaction channels with a small energy defect dominate. Other pair states contribute only insignificantly and can be omitted.
Figure 1.15 shows a pair state Stark map of the relevant Rydberg pair states at the Förster resonance. Only the $|pf_i\rangle$ states show a small energy defect and have to be considered besides the $|dd\rangle$ state. Since the states $|pf_i\rangle$ and $|f_ip\rangle$ are degenerate but only the symmetric combination of both couples to $|dd\rangle$, the pair states relevant for the Rydberg-Rydberg interaction are $\frac{1}{\sqrt{2}}(|pf_i\rangle + |f_ip\rangle)$ and $|dd\rangle$. To reduce the number of state further only $i = 1 \ldots 4$ was considered here, as the resonances of $|pf_5\rangle$ and $|pf_6\rangle$ appear at small electric fields that cannot be realized in the experiments.
In the presence of an excitation laser field that couples additionally the ground state 5s, denoted by g, to the 44d state, additional states have to be included. Every atom couples independently to the light field and the excitation has to be described as a single atom process. Therefore the additional states are $|gg\rangle$ and $\frac{1}{\sqrt{2}}(|gd\rangle + |dg\rangle)$ and no direct coupling from $|gg\rangle$ to $|dd\rangle$ exists. The antisymmetric combination is, again, not coupled by the field and needs not to be taken into account.
In the basis ($|gg\rangle$, $\frac{1}{\sqrt{2}}(|gd\rangle + |dg\rangle)$, $|dd\rangle$, $\frac{1}{\sqrt{2}}(|pf_1\rangle + |f_1p\rangle)$,$\frac{1}{\sqrt{2}}(|pf_2\rangle + |f_2p\rangle)$,$\frac{1}{\sqrt{2}}(|pf_3\rangle + |f_3p\rangle)$ and $\frac{1}{\sqrt{2}}(|pf_4\rangle + |f_4p\rangle)$) the Hamiltonian can be written in the dressed states

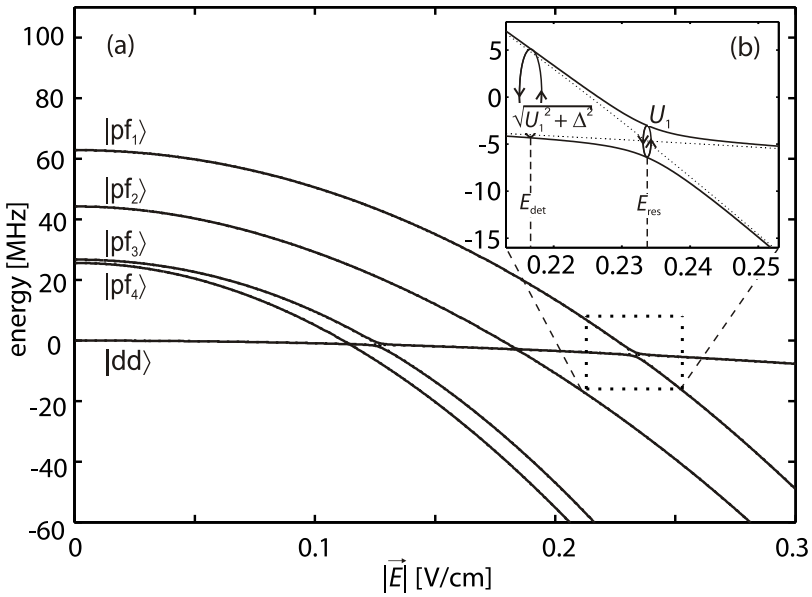

Figure 1.15: (a) Stark map of the relevant Rydberg pair states (see text). (b) shows a magnification of the Stark map at the electric field where the pair states are tuned into resonance. The dashed lines denote the pair state energies without coupling; the solid lines include a dipole-dipole coupling. The energy differences at the resonant electric field E_{res} and at a detuned electric field E_{det} are indicated.

picture as

$$H = \begin{pmatrix} 0 & \frac{\Omega}{\sqrt{2}} & 0 & 0 & 0 & 0 & 0 \\ \frac{\Omega}{\sqrt{2}} & \delta_L + E_d & \frac{\Omega}{\sqrt{2}} & 0 & 0 & 0 & 0 \\ 0 & \frac{\Omega}{\sqrt{2}} & 2\delta_L + 2E_d & U_1(r,\Theta) & U_2(r,\Theta) & U_3(r,\Theta) & U_4(r,\Theta) \\ 0 & 0 & U_1(r,\Theta) & 2\delta_L + E_{pf_1} & 0 & 0 & 0 \\ 0 & 0 & U_2(r,\Theta) & 0 & 2\delta_L + E_{pf_2} & 0 & 0 \\ 0 & 0 & U_3(r,\Theta) & 0 & 0 & 2\delta_L + E_{pf_3} & 0 \\ 0 & 0 & U_4(r,\Theta) & 0 & 0 & 0 & 2\delta_L + E_{pf_4} \end{pmatrix} \tag{1.50}$$

where E_d is the Stark shift of one atom in the 44d state, E_{pf_i} the shift of the $|pf_i\rangle$ pair state and δ_L the detuning of the laser to the 44d state. Ω is the Rabi frequency of the laser coupling between the $5s_{1/2}$ ground state and the $44d_{5/2}$ Rydberg state. The strength of the pair state couplings is given by the dipole-dipole operator matrix elements $U_i = \sqrt{2}\,\langle pf_i|\, V_{\mathrm{dd}}\, |dd\rangle$, depending on the interatomic distance r and the angle Θ (Figure 1.11).
Diagonalization of this Hamiltonian gives the pair state energies as a function of the interatomic distance. Figure 1.16 shows the energy levels of the Rydberg atom pair states

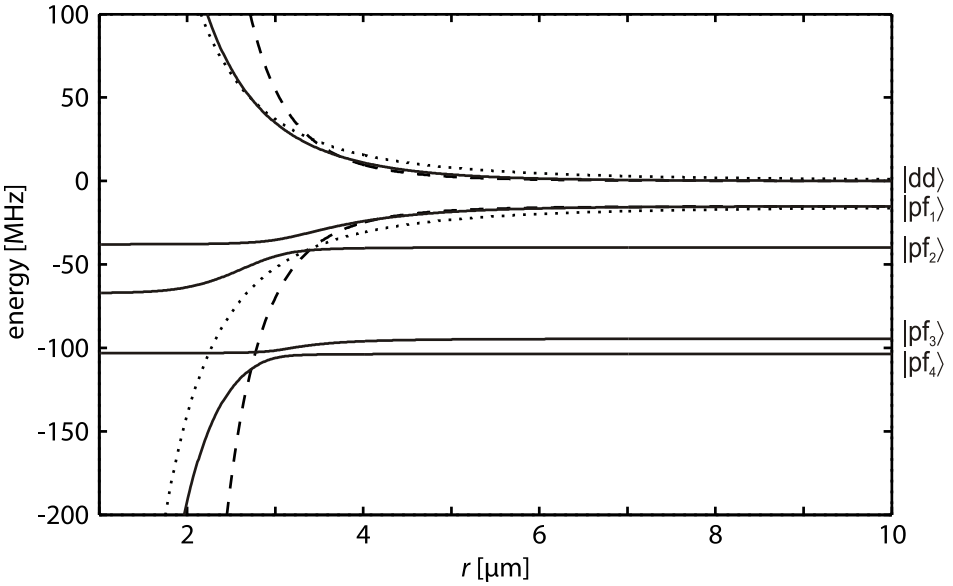

Figure 1.16: Potential energy curves obtained from the diagonalization of Hamiltonian (1.50) for $|\vec{E}| = 0.26\,\mathrm{V/cm}$ and $\Theta = 30°$. The labeling of the states at infinite interatomic distance r follows Figure 1.15. The results from perturbation theory are plotted as dotted lines (resonant dipole-dipole interaction) and dashed lines (van der Waals interaction).

for $\Omega = 0$, $\Theta = 30°$ and $|\vec{E}| = 0.26\,\mathrm{V/cm}$. The angle of $\Theta = 30°$ was exemplarily chosen so that all resonances appear. These calculations agree with the van der Waals interaction (dashed line, calculated from (1.49)) of the 44d pair state for large interatomic distances, even though these calculations are performed with a considerably reduced pair state basis. The repulsive potential at small distances can be roughly reproduced by the dipole-dipole interaction (equation (1.42), dotted line), but a clear deviation is visible. Diagonalization results in a stronger interaction than the pure dipole-dipole interaction due to the coupling to all four $|pf_i\rangle$ states. The attractively interacting states show a number of avoided crossings at small distances and do not agree with the perturbative results as several near-resonant interaction channels contribute.
This approach of full diagonalization of a reduced pair state system offers many advantages. Besides the reduced computational effort compared to the calculation of van der Waals interactions, also the cross-over region can be addressed, where neither the resonant dipole-dipole nor the van der Waals interaction provide good results. Furthermore this approach allows calculating the time evolution of the pair state system by use of the Schrödinger equation (1.4), that is fundamentally important for describing a pulsed experiment. This is done in the concept of the pair state interferometer in section 3.2.3.

1.3.8 Rydberg blockade and collective excitation

An important consequence of the Rydberg-Rydberg interaction is the so-called Rydberg blockade, which limits the population of the excited Rydberg state. This local blockade of Rydberg excitation has been widely studied theoretically [85] and experimentally in ultracold gases, employing van der Waals interaction [86], induced permanent dipole-dipole interaction in an electric field [81] and resonant dipole-dipole interaction at a Förster resonance [20].
In the case of two two-level atoms, with a coupling laser tuned on resonance to the ground state-Rydberg state transition with the Rabi frequency Ω_0, one atom can be excited to the Rydberg state. Due to the interaction between two atoms in the Rydberg state, the transition of the second atom to the excited state is shifted in energy by the interaction energy $U(r)$, depending on the interatomic distance r. This transition can only be driven by the laser if the interaction energy shift is smaller than the excitation linewidth, given by the Rabi frequency Ω or the total excitation linewidth $\Delta\omega$, in the case of additional broadening mechanisms exceeding the power broadening. This leads to the condition

$$\hbar\Delta\omega \leq |U(r)| \tag{1.51}$$

for the suppression of the excitation to the doubly excited state. Depending on the type of interaction it creates a blockade sphere of radius $r \leq \sqrt[k]{\frac{|C_k|}{\Delta\omega}}$ where the doubly excited state is suppressed, with $k = 3$ for dipole-dipole and $k = 6$ for van der Waals interaction. The picture of a spherical blockaded volume is, of course, only true for isotropic interaction. In the case of angular dependent dipole-dipole interaction this is more like a blockade ellipsoid and even shows no blockade effect under the magic angle of 54.7°.
In the limit of strong blockade ($U \gg \hbar\Delta\omega$) this effect is not dependent on the actual character of the interaction. This makes the Rydberg blockade possible with arbitrary interactions and independent of fluctuations in the interaction strength due to fluctuations in the interatomic distance. Especially these properties of Rydberg atoms raised the growing interest in ultracold Rydberg atoms as building blocks for quantum logic gates [41] or single photon sources [56, 54].
For typical interaction strength at $\Theta = 0°$ of the Rydberg states used here ($C_3 = \pm 2\pi \times 1556\,\mathrm{MHz}\mu\mathrm{m}^3$ at the resonance at $|\vec{E}| = 0.214\,\mathrm{V/cm}$, $C_6 = -2\pi \times 28\,\mathrm{GHz}\mu\mathrm{m}^6$ at $|\vec{E}| = 0\,\mathrm{V/cm}$) one obtains blockade radii of $17.5\,\mu\mathrm{m}$ at resonance and $6.7\,\mu\mathrm{m}$ at $E = 0$, with a linewidth of $2\pi \times 300\,\mathrm{kHz}$. At typical ground state atom densities of $\rho = 10^{10}\,\mathrm{cm}^{-3}$ up to $\rho = 10^{13}\,\mathrm{cm}^{-3}$ in ultracold atomic samples realized in the experiments here the blockade radius is considerably larger than the nearest neighbor distances between $2.8\,\mu\mathrm{m}$ and $0.3\,\mu\mathrm{m}$, calculated from the Wigner Seitz radius [87]

$$r_{\mathrm{WS}} = \sqrt[3]{\frac{3}{2\pi\rho}}. \tag{1.52}$$

More than two atoms are within the blockade sphere and the excitations are delocalized and shared collectively among all N atoms inside the blockade sphere. The single excited state is

$$|N,1\rangle = \frac{1}{\sqrt{N}} \sum_{i=1}^{N} |g_1, g_2, \ldots, r_i, \ldots, g_N\rangle \,, \tag{1.53}$$

where g denotes the ground state, r the Rydberg state and the subscript labels the atoms. The coupling to the ground state $|N,0\rangle$, described by a collective Rabi frequency Ω_{eff}

$$\Omega_{\text{eff}} = \langle N,1| \, H_{\text{AL}} \, |N,0\rangle = \sqrt{N}\Omega_0, \tag{1.54}$$

shows a collective enhancement by $\sqrt{N}$. The ensemble of N atoms behaves as a single atom, often called 'superatom' [88], with a Rabi frequency of Ω_{eff}. This enhancement of the Rabi frequency was nicely shown in [42, 43] in the case of two atoms.
In an ensemble of atoms, however, the spatial density distribution of the trapped cloud of ultracold atoms creates a band of collective Rabi frequencies in the system [89]. In the presence of a driving laser field no Rabi oscillations are visible as the spatially different oscillations add up. The excitation of such an ensemble shows a roughly linear increase with time up to a saturation in the Rydberg atom number, limited by the Rydberg blockade.
It is interesting to note that the Rydberg blockade significantly changes the excitation dynamics even when the system is not driven into saturation because the collective enhancement of the excitation dynamics appears already at small Rydberg densities. This behavior is important for the modeling of the pair state interferometer in chapter 3.2.3.
The concept of blockaded 'superatoms' has to be applied carefully, especially in the case of strong interactions between the Rydberg atoms. Strictly speaking, it is only valid in the case of strong blockade of an ensemble smaller than the blockade radius and with pure binary van der Waals interactions. In the case of dipole interaction ($\propto 1/r^3$) it was shown [90] that already in the case of three interacting atoms noninteracting states exist, even for strong two-body interactions. In the case of Förster resonances additional states can appear that do not show interactions, so-called Förster-zero states [31]. These states break the Rydberg blockade and enable multiple excitations.
However, a careful consideration of the model often leads to reasonable results with the great advantage that the number of atoms in such models can be strongly reduced. It is also used to simulate interaction-induced effects in section 3.2.3.

1.4 Ultralong-range Rydberg molecules

The unusual, often exaggerated properties of Rydberg atoms not only lead to interesting single-atom and collective effects, but also open the way to developments in the emerging field of ultracold chemistry. Ultracold is usually defined as the regime where collision dynamics of particles are dominated by single partial-wave scattering [12]. Only very few observations have been made so far that are specific to the ultracold chemistry regime, like photoassociation of ultracold molecules [59], Bose-Einstein condensation of molecules [46, 47] and Efimov resonances [48].
The interaction of a weakly bound Rydberg electron with ground state atoms within the electron's wavefunction can indeed solely be described by s- and p-wave scattering because of the low average velocity of the Rydberg electron. It leads to the binding of molecular states, first proposed in 2000 [91] and recently created and observed in photoassociation spectroscopy [49] in our group, with very low binding energies of some tens of MHz.
The binding mechanism is novel in the sense that it cannot be described by the classical binding mechanisms known to chemistry, that are covalent, ionic and van der Waals binding. Besides this peculiar character, which already shows the wide potential of ultracold chemistry with Rydberg atoms, ultralong-range Rydberg molecules show several unusual properties that have been studied in the last years. Examples are direct three body photoassociation to a trimer state [92], quantum reflection [92], coherent control of the binding [93] and the lifetime and decay process of the molecules [94].
Here, I will report on an additional, maybe even more stunning peculiarity of these molecules: the emergence of a permanent dipole moment in a homonuclear diatomic molecule. I will first describe the binding mechanism before I will explain how this dipole moment forms, that contradicts classical textbook knowledge. The exact calculation of the permanent electric dipole moment was done in a collaboration with theoretical physicists from the Max-Planck-Institute for the Physics of Complex Systems in Dresden and from the Harvard-Smithonian Center for Astrophysics in Cambridge, USA [50].

1.4.1 Binding mechanism

Ultralong-range Rydberg molecules are a bound state formed of one atom in a highly excited Rydberg state and a ground state atom. The binding relies on frequent scattering of the Rydberg electron off the ground state atom. The electron itself is only weakly bound to the ionic core of the Rydberg atom via Coulomb interaction and can be treated as a quasi-free particle of very low kinetic energy. The ground state atom forms a weak perturber within the electron's wavefunction that can be described by a zero-range Fermi pseudopotential interaction of a free, low-energy electron and a ground state

atom [95, 96] as[2]

$$\hat{V}(\vec{r},\vec{R}) = 2\pi A_s(k)\delta(\vec{r}-\vec{R}) + 6\pi A_p(k)^3\delta(\vec{r}-\vec{R})|\nabla|^2 \tag{1.55}$$

in s- and p-wave scattering. The positions of the ground state atom $\vec{R}$ and of the Rydberg electron $\vec{r}$ are expressed relative to the Rydberg atom core and $A_s(k)$ and $A_p(k)$ are the energy dependent s- and p-wave scattering lengths of the electron-ground state atom scattering [96, 97]. In the case of Rubidium, the triplet spin scattering length ($S = 1$) is negative ($A_s(k=0) = -16.05a_0$ [98, 99] and $A_p(k=0) = -21.15a_0$ [92]) and leads to an attractive potential, whereas the singlet ($S = 0$) scattering length is positive [100]. Therefore only atoms in the triplet state can bind and are considered here.
In a semiclassical picture the electron momentum is calculated from the classical energy equation $E_b = \frac{k^2}{2} - \frac{1}{R}$ for a bound particle of binding energy E_b in a Coulomb potential. The simplest approach to calculate the effect of this scattering is to adopt Fermi's idea of a pseudopotential

$$V_{\text{Fermi}} = \langle \Psi_{35s}(\vec{r})|\, \hat{V}(\vec{r},\vec{R})\, |\Psi_{35s}(\vec{r})\rangle\,. \tag{1.56}$$

In these Fermi-scattering calculations the interaction operator (1.55) acted on the unperturbed 35s Rydberg electron wavefunction only and influences of nearby states and perturbations of the electron wavefunction by the ground state perturber are omitted. These aspects will be discussed subsequently.
Figure 1.17 shows the calculated Fermi pseudopotential. At large interatomic distances, where the electron momentum is small, s-wave scattering dominates and the molecular potential resembles the oscillatory character of the electron wave function, creating a potential well that supports a bound state [91]. At smaller distances, where the electron momentum is bigger, the p-wave contribution becomes significant and the oscillatory behavior is strongly modified.
This Fermi-scattering theory approach yields an instructive description of the fundamentals of the novel binding mechanism and allows calculating a bound molecular state involving a ns Rydberg state by calculating the Fermi-pseudopotential. However, in the vicinity of the p-wave shape resonance this approach fails, because an avoided crossing at the resonance appears [102]. More accurate nonperturbative Green's function calculations [92] were used to calculate the molecular potential even for smaller interatomic distances. Another way to calculate the full potential is to diagonalize the Hamiltonian $H = H_A + \hat{V}$, where H_A is the unperturbed Rydberg atom Hamiltonian. For a large enough basis set this results in the same potential as the Green's function approach [50]. Figure 1.18 (b) shows this potential together with the corresponding excited states. The potential exhibits a deep drop at $R \approx 1200$ a.u. due to an avoided crossing at the shape resonance and a wide plateau between 1200 a.u. and 2000 a.u. Besides the vibrational ground state of the molecule at -23 MHz it features vibrationally excited states which

[2] All formulas in this chapter are in atomic units using the Bohr length $a_0 = 0.529 \times 10^{-10}$ m.

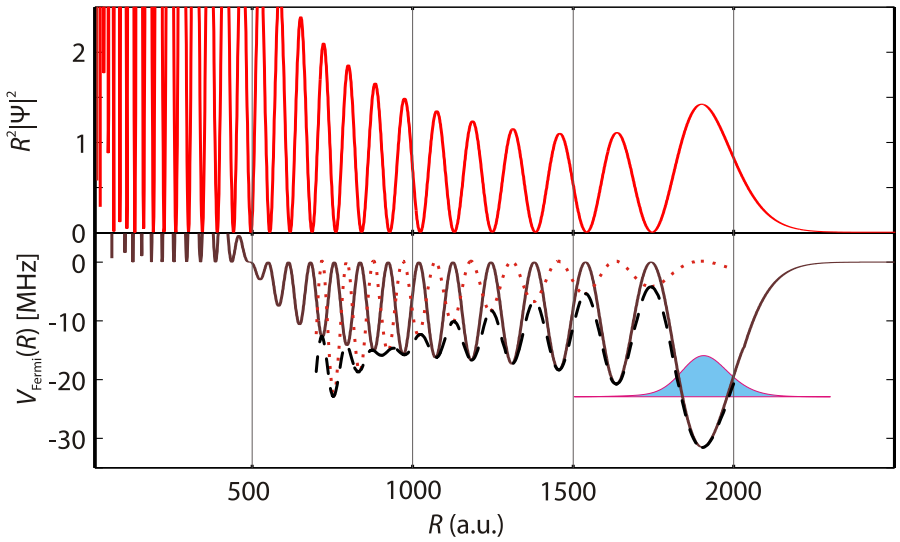

Figure 1.17: Calculated 35s electron probability density $R^2|\Psi|^2$ (upper panel) and molecular potential V_{Fermi} from equation (1.56) (lower panel) as a function of the interatomic distance R. The solid potential shows the pure s-wave contribution, the dotted line the pure p-wave contribution and the dashed line the full potential using the interaction operator from equation (1.55). The outermost potential well at 1900 a.u. ($\approx 100\,\text{nm}$) arises predominately by s-wave scattering and supports a bound state with a binding energy of 23 MHz, which vibrational wavefunction is indicated. Figure adapted from [101].

are delocalized over the potential plateau and are strongly influenced by the shape resonance. They are not conventionally bound in potential minima, but the binding emerges by quantum reflection at the sharp potential drop at the shape resonance [92]. Experimentally these molecules were created by direct photoassociation from unbound ground state atoms. In spectroscopy experiments they show up as additional resonances at slightly lower excitation frequencies compared to the atomic Rydberg line, where the frequency difference corresponds to the binding energy. Such a spectroscopy signal can be seen in Figure 1.18 (c), where the molecular ground states as well as several excited states are resolved.

So far only Rydberg ns states were considered, which are energetically well separated from other Rydberg states because of a large quantum defect. As the Rydberg electron wavefunction is spherically symmetric and non-degenerate no electric dipole moment was predicted in these states [91]. A pure quadratic Stark shift was expected, arising from the polarizability of the Rydberg atom. First measurements of the Stark effect for electric fields up to 3 V/cm [49] could not detect a deviation to this quadratic shift within the experimental resolution. However, recent results with higher resolution [50] show that this original picture is not complete and that these molecules indeed possess an electric dipole moment. I will report on the origin of this dipole moment in the next

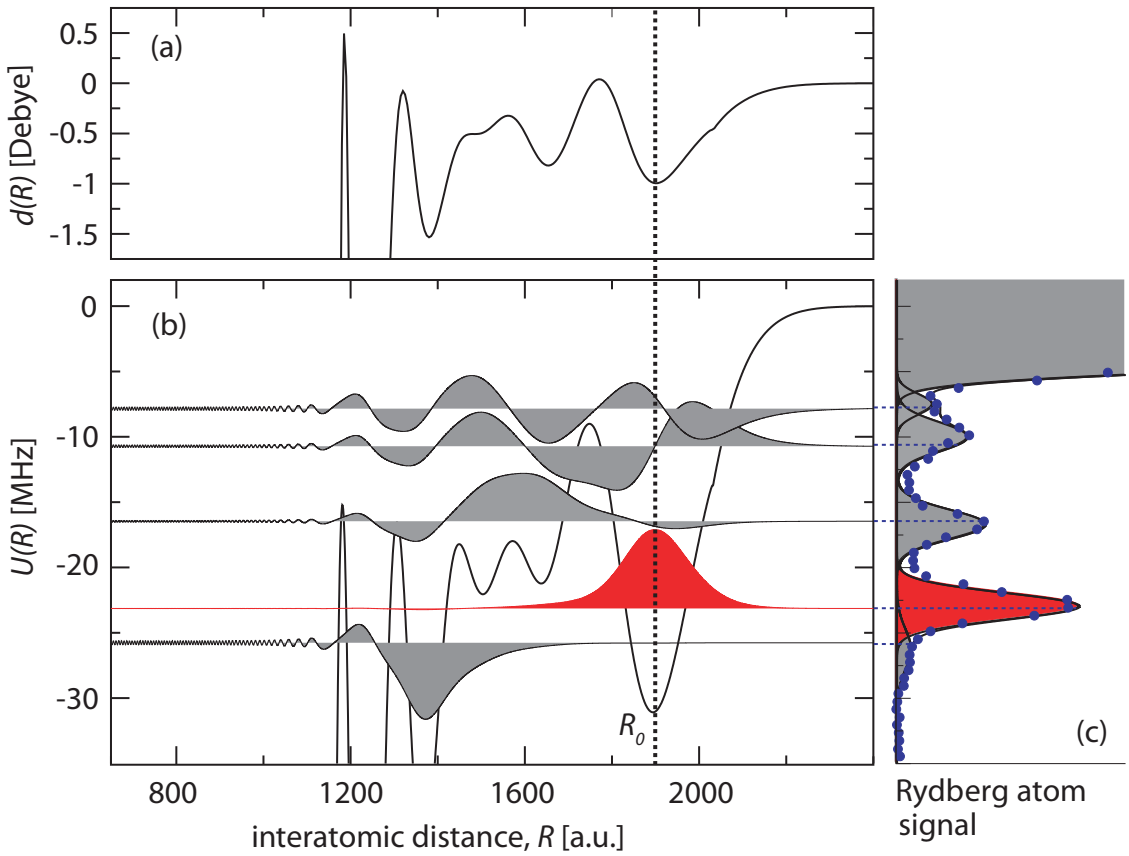

Figure 1.18: Calculated molecular potential, vibrational wavefunctions and dipole moment of the ultralong-range Rydberg molecule $^3\Sigma(5s-35s)$. (a) shows the calculated dipole moment as a function of the internuclear distance R. (b) The molecular potential obtained by diagonalization of the perturbed Hamiltonian shows a deep drop at ≈ 1200 a.u. due to a p-wave shape resonance (solid black line). The vibrational ground state of the molecule at -23 MHz is localized in the outermost potential well at ≈ 1900 a.u. (red shaded area) while the vibrationally excited molecular states (gray shaded areas) are bound via quantum reflection to the potential plateau. (c) shows a measured Rydberg spectrum featuring the ground and excited states in good agreement with the theory.

section and on the high resolution measurements in chapter 4.
Another class of molecules are formed if the Rydberg atom is in a high-l state. In the case of high-l Rydberg states many quasi-degenerate Rydberg levels exist, leading to a mixing of the states. Calculations of the molecular potential [91] show a less pronounced oscillatory behavior due to the mixing of the states, but one deep potential well that supports many bound states. Besides the orders of magnitude increased binding energy these molecules are also predicted to have huge permanent dipole moments. The necessary charge separation shows in a characteristic polar electron probability distribution reminiscent of trilobites, hence these states are called trilobite states.

1.4.2 Rydberg molecules in electric fields

To understand the behavior of molecules in electric fields a comprehensive understanding of dipole moments is necessary. An electric dipole moment $\vec{d}$ forms by a charge separation and is defined by the separated charge q times the distance $\vec{r}$

$$\vec{d} = q \cdot \vec{r}. \tag{1.57}$$

It induces a Stark effect of

$$\Delta E_{\text{Stark}} = \vec{d} \cdot \vec{E} \tag{1.58}$$

and its unit is ea_0 in atomic units or Debye, where $1\,\text{Debye} = 3.34 \times 10^{-30}\,\text{Cm}$ in SI units.
This charge separation can either be permanent or induced. An induced charge separation is created by an electric field that polarizes the atom or molecule, described by the polarizability α, and leads to an induced dipole moment $\vec{d} = \alpha\vec{E}$. Atoms or molecules possess an induced dipole moment in a finite electric field even if they do not show a dipole moment in the absence of an electric field. Inserting the induced dipole moment into equation (1.58) leads to a quadratic Stark effect in the electric field. Note that this description in terms of a polarization is only valid for small electric fields that do not mix several states. Beyond this a linear Stark effect emerges.
A charge separation in the absence of an electric field forms a permanent dipole moment. However, it is necessary to distinguish between the body-fixed reference frame, that is aligned along the molecular axis, and the space-fixed laboratory frame, that is aligned, e.g., along the external electric field. A charge separation in the eigenstates of the molecule always results in a body-fixed dipole moment. A space-fixed dipole moment forms if the dipole moment is not averaged out by a rotation of the molecule. Only if a permanent dipole moment $\vec{d}$ in the laboratory reference frame exists a linear Stark effect emerges, following equation (1.58). Therefore a linear Stark effect at small electric fields is clear evidence for a space-fixed permanent dipole moment.
Homonuclear molecules as dioxygen (O_2) or nitrogen (N_2) or ultracold homonuclear molecules as Cs_2 [103], consisting of two same atoms, do usually not possess a perma-

nent dipole moment due to symmetry reasons. None of the atoms is superior and no charge separation occurs. Instead, they can be polarized and an induced dipole moment forms that leads to a quadratic shift of the molecular excitation line in an applied electric field. A linear Stark shift, as an evidence for a permanent space-fixed dipole moment, can only occur in the case of different electronegativities of the constituents in heteronuclear molecules [104]. This classical argumentation can be found in many physics and chemistry textbooks [105, 106].
In the following I will explain how the permanent, space-fixed dipole moment in the ultralong-range Rydberg molecule forms. I will first explain the occurrence of the charge separation in this homonuclear molecule, that is the origin of a body-fixed dipole moment. Subsequently I will show why this body-fixed dipole moment is oriented in space to form a space-fixed dipole moment, resulting in a linear Stark effect.
The body-fixed dipole moment in the homonuclear ultralong-range Rydberg molecules forms due to the unusual binding mechanism. Frequent attractive electron-ground state atom collisions bind the ground state atom to the Rydberg electron wavefunction, as explained in the preceding chapter. The back action of this interaction also changes the electron wavefunction and localizes the Rydberg electron slightly to the position of the ground state perturber. The original Fermi-scattering approach [91] omits this effect and does not predict a charge separation. Complete diagonalization however includes the back action and results in slightly perturbed eigenfunctions. Figure 1.19 shows the perturbed probability density $|\Psi|^2$ of the Rydberg electron in the presence of the ground state atom. Although the overall shape of the wavefunction is still nearly spherically symmetric, a localization to the region of the ground state atom is visible. This results in a charge separation in the body-fixed frame of these states.
Usually exchange symmetry prohibits a permanent body-fixed dipole moment of eigenstates of a homonuclear molecule, even if molecular states with a charge separation exist. Two states, where e.g. the body-fixed permanent dipole moment points up ($|\uparrow\rangle$) and down ($|\downarrow\rangle$), are degenerate in zero electric field and the eigenstates $\frac{1}{\sqrt{2}}(|\uparrow\rangle \pm |\downarrow\rangle)$ of the molecule do not show a permanent dipole moment. Here, the two atoms differ considerably in their electronic state and thereby in the size of the electron wave functions. The ground state electron wavefunction is many orders of magnitude smaller than the Rydberg electron wavefunction. An exchange between the states $|\uparrow\rangle$ and $|\downarrow\rangle$ can either happen if the Rydberg excitation is transferred to the initial ground state atom or if the electrons are interchanged between the atoms. Excitation transfer is suppressed by a small overlap integral between both wavefunctions due to the size difference and since the corresponding transition between the 5s ground state atom and the ns Rydberg atom is not dipole allowed. Parity exchange by an interchange between the electrons has to happen via tunneling of the ground state electron to the ionic core of the Rydberg atom, about 100 nm away. The strength of the coupling between the two states is proportional to the tunneling amplitude and exponentially small in the binding length.

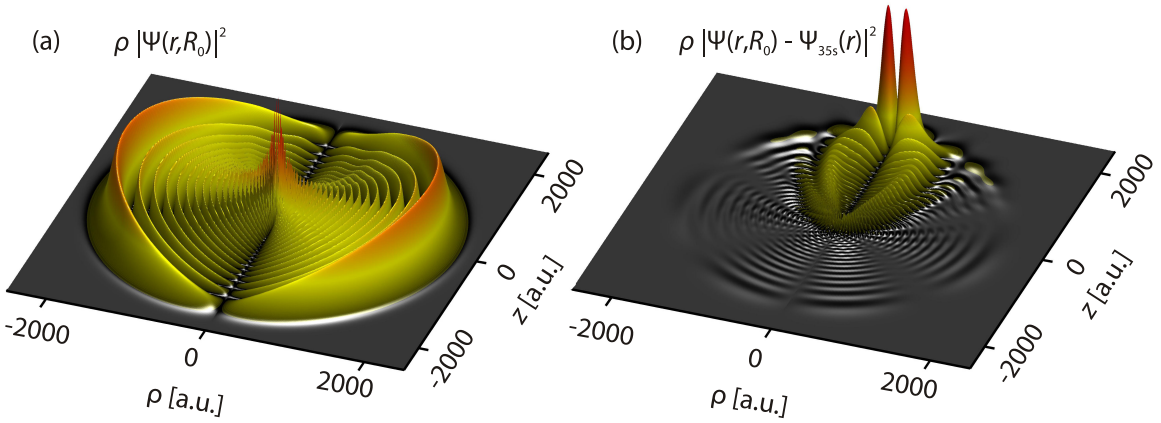

Figure 1.19: (a) A surface plot of the perturbed Rydberg electron probability density $\rho|\Psi|^2$ in the $^3\Sigma(5s-35s)$ molecular state in cylindrical coordinates, where ρ is the radial coordinate. (b) Subtracting the unperturbed Ψ_{35s} Rydberg atom wavefunction shows the locally enhanced probability density of the perturbed wavefunction at the position of the ground state atom at $\rho = 0\,\text{a.u.}$ and $z = 1900\,\text{a.u.}$, featuring a Cologne Cathedral-like structure. The probability density in (b) is scaled by a factor 200 compared to (a). Note that the minimum at the axis $\rho = 0\,\text{a.u.}$ stems from the presentation in cylindrical coordinates, where the probability density is multiplied by ρ.

The corresponding delocalization time is longer than the time of the universe and no parity exchange will happen during the lifetime of the molecule. In a photoassociation experiment any external field will break this symmetry and the molecule is directly created in one localized state and due to the improbable parity exchange a body-fixed permanent dipole moment in a homonuclear molecule occurs.
Even in the case of a body-fixed dipole moment, both for the ultralong-range Rydberg molecules and for heteronuclear linear molecules with different electronegativities of the constituents, on time average the space-fixed dipole moment is zero as in free space the linear molecule rotates uniformly top over top. In a quantum mechanical object this is expressed by rotationally invariant rovibratonal eigenfunctions. A permanent dipole moment in a quantum mechanical object requires a charge separation to form a body-fixed dipole moment and degenerate opposite parity eigenstates that mix to form rotationally non-invariant states [105]. This applies also to polar molecules in the ro-vibrational ground state, as KRb [107] or LiCs [108]. The closest eigenstates in the case of KRb, e.g., are rotational states splitted by the rotational constant $B = 1\,\text{GHz}$ [107]. These eigenstates can mix in the presence of strong electric fields that lead to an orientation of the molecule in the external field and to a space-fixed dipole moment, measurable as a linear Stark effect in these strong fields. But for small fields the rotational states are non-degenerate and only a quadratic Stark effect is visible. These polar molecules have no permanent space-fixed dipole moment.

In the case of ultralong-range Rydberg molecules the situation is completely different as the rotational constant B

$$B = \frac{\hbar^2}{2I}, \tag{1.59}$$

with the moment of inertia $I = \mu R^2$, is small. For the homonuclear ${}^3\Sigma(5s{-}35s)$ molecule (reduced mass $\mu = 1/2 \cdot m_{\mathrm{Rb}}$) one obtains $B = 11.5\,\mathrm{kHz}$ because of the huge binding length of $R \approx 100\,\mathrm{nm}$. This is considerably smaller than the molecular linewidth of $\Delta\nu = 142\,\mathrm{kHz}$ [94], hence the rotational states are nearly degenerate and mix within the linewidth to form localized electronic states producing a permanent dipole moment and a linear Stark effect even at the smallest electric field. This can also be seen as taking $T = \frac{1}{2\pi\Delta\nu} = 1\,\mu\mathrm{s}$ long snapshots, limited by the lifetime of the molecule, during which the dipole moment only rotates through a negligibly small angle with respect to the external field [109]. The molecule appears oriented in space and a body-fixed dipole moment also shows as a space-fixed dipole moment, leading to a linear Stark effect at small electric fields.
In conclusion, the fundamental difference of the ultralong-range Rydberg molecules to usual homonuclear diatomic molecules is its huge binding length and its unusual binding mechanism. The nature of the binding, which is only moderated by the highly excited Rydberg electron, leads to a charge separation in the molecules. In contrast to the delocalized Rydberg electron the electron of the ground state atom is strongly localized. This vast difference in the length scale suppress the exchange of the charge separation and enables this molecule to possess an body-fixed electric dipole moment. Furthermore, the huge binding length allows a slow rotation that can be neglected on the timescale of the lifetime. Thereby a permanent space-fixed electric dipole moment forms, contradicting the long-held belief of textbook physics that homonuclear diatomic molecules are never polar.

To calculate this permanent electric dipole moment d the matrix element of the dipole operator z has to be calculated as

$$d(R) = \langle \Psi(r,R)|\, z\, |\Psi(r,R)\rangle\,. \tag{1.60}$$

The perturbed wavefunction $|\Psi(r,R)\rangle$ of the Rydberg electron in the presence of the bound ground state atom is calculated by diagonalizing the Hamiltonian

$$H = H_A + \hat{V}, \tag{1.61}$$

where H_A is the unperturbed atomic Hamiltonian and $\hat{V}$ the interaction operator (1.55). The dipole moment, shown in Figure 1.18 (a) as a function of the interatomic distance R, is on the order of 1 Debye and somewhat follows the oscillations of the molecular potential. Whenever the potential shows clear dips due to a strong scattering process also the dipole moment is strong.

The dipole moment of the vibrational states is calculated by averaging the distance-dependent dipole moment $d(R)$ over the distribution of the vibrational wave function, plotted in Figure 1.18 (b). For the vibrational ground state of the ${}^3\Sigma(5s-35s)$ molecule an expectation value of the dipole moment of $d = 1.17$ Debye was found and a decrease of the dipole moment with $1/(n^\star)^2$, where $n^\star$ is the effective quantum number. The calculated dipole moments for a wide range of principal quantum numbers, together with measured values, can be found in chapter 4.2 and Figure 4.5 (a).
This scaling can be understood as the perturbation of the electron probability density stems from a mixing with degenerate high-l molecular states Ψ_{nT}, so-called trilobite states. This mixing is clearly visible in the characteristic probability distribution in Figure 1.19 (b). Non-degenerate p states can also be mixed to generate a dipole moment, but as their dipole moment is small this mixing is not relevant for the derivation of the scaling law. The perturbed wavefunction can be written as

$$\Psi(r,R) = \Psi_{ns}(r) + \epsilon(R)\Psi_{nT}(r,R), \tag{1.62}$$

where $\epsilon(R)$ is the mixing fraction. The trilobite wavefunction $\Psi_{nT}(r,R)$ is the wavefunction of the Rydberg electron at position r in the high-l state in the presence of the ground state atom at position R. The trilobite states possess a permanent dipole moment of magnitude [91]

$$d_T \approx R - \frac{1}{2}(n^\star)^2 \tag{1.63}$$

in atomic units, that scales as $(n^\star)^{-2}$ due to mixing of degenerate states in the Rydberg manifold. The unperturbed $\Psi_{ns}(r)$ wavefunction does not exhibit a dipole moment.
The permanent dipole moment of the low-l molecule state (1.62) is

$$d(R) = \langle\Psi(r,R)|\, z\, |\Psi(r,R)\rangle = \epsilon(R)^2 d_T(R). \tag{1.64}$$

The mixing fraction scales as $\epsilon \propto (n^\star)^{-2}$ [50] and will be calculated in the following. Using (1.63), one obtains the scaling of the dipole moment

$$d(R) \propto 1/(n^\star)^2 \tag{1.65}$$

that was also numerically observed.

The scaling of the mixing fraction ϵ can be obtaind by minimizing the pure s-wave molecular potential

$$V(R) = \langle\Psi(r,R)|\, H_0 + 2\pi A_s \delta(R-r)\, |\Psi(r,R)\rangle \tag{1.66}$$

using the perturbed wavefunction (1.62). If the energy is normalized to the Rydberg s state ($E_{ns} = 0$) one obtains

$$\begin{aligned} V(R) = {} & \epsilon\Delta_T + 2\pi A_s |\Psi_{ns}(R)|^2 + 2\pi A_s \epsilon^2 |\Psi_{nT}(R,R)|^2 \\ & + \epsilon \cdot 2\pi A_s \mathrm{Re}\left[\Psi^*_{ns}(R)\Psi_{nT}(R,R)\right] \end{aligned} \tag{1.67}$$

with the energy gap $\Delta_T = E_{(n-3)(l>3)} - E_{ns}$ between the Rydberg s state and the next $(n-3)$ Rydberg manifold (see 1.3) that scales as $(n^\star)^{-3}$. The p-wave contribution is considerably smaller for this particular molecular state, where the molecule is in the vibrational ground state, and is neglected. Minimization of the second order polynomial (1.67) leads to

$$\epsilon = -\frac{2\pi A_s \mathrm{Re}\left[\Psi^*_{ns}(R)\Psi_{nT}(R,R)\right]}{2(\Delta_T + 2\pi A_s |\Psi_{nT}(R,R)|^2)}. \tag{1.68}$$

The second term in the denominator describes the binding energy of the trilobite, that is smaller than the energy gap Δ_T and can be neglected.
The scaling of the mixing fraction with n can now be discussed term by term. From the scaling of the size of the Rydberg wavefunction with $(n^\star)^2$ and from the wavefunction normalization follows $|\Psi_{nl}(R)|^2 \propto 1/V \propto (n^\star)^{-6}$ and especially $\Psi_{ns}(R) \propto (n^\star)^{-3}$. Together with $\Delta_T \propto (n^\star)^{-3}$ one obtains

$$\epsilon \propto \Psi_{nT}(R,R). \tag{1.69}$$

The trilobite wavefunction constitutes of all quasidegenerate high-l states ($l \geq l_{min} = 3$) and the scaling of the probability amplitude at position R can be calculated to be [91]

$$\begin{aligned} |\Psi_{nT}(R,R)|^2 &= \sum_{l=l_{\min}}^{n-1} \frac{2l+1}{4\pi} |\Psi_{nl}(R)|^2 \\ &\propto \frac{(n^\star)^2}{(n^\star)^6} \propto \frac{1}{(n^\star)^4}, \end{aligned} \tag{1.70}$$

since the sum over l scales as $(n^\star)^2$ and $|\Psi_{nl}(R)|^2 \propto (n^\star)^{-6}$. This results in a scaling of the mixing fraction as $\epsilon \propto (n^\star)^{-2}$.

2 Experimental setup

The fundamental topics of the experiments in this thesis, as coherent control of interacting atoms and ultralong-range Rydberg molecules, impose challenging requirements on the experimental setup. Coherent control necessitates long coherence times, that can especially be realized at ultracold temperatures. Controlled interactions are offered by Rydberg atoms and apparently it is favorable to combine ultracold atoms with Rydberg excitation to realize coherent control of interactions. Furthermore, the creation of ultralong-range Rydberg molecules, need dense and cold samples that can be achieved in ultracold atoms as well. Hence evaporatively cooled atomic samples provide an ideal environment for these experiments. The element of choice in this case is ^{87}Rb, as trapping and evaporative cooling of ^{87}Rb atoms in a magnetic trap is well understood and performed in many other experiments. Here, the fundamental difference to most other BEC and cold atom experiments is the expansion of the setup to excite and detect Rydberg atoms. This includes a high stability laser system for two-photon excitation, electric field control and ion detection.
Therefore I divide the description of the setup into two parts: The preparation of the ultracold atoms that is mostly well known in the field of atomic physics and quantum optics, and a second part that describes the essential components for dealing with Rydberg atoms. As the fundamental experimental setup was already set up and described by my predecessors [73, 101, 110, 111, 112] and only selectively improved during this thesis I will only describe the parts that differ from previous work or that are fundamentally important in the course of this work.

2.1 Preparation of ultracold atoms

For the preparation of ultracold atoms a magnetic trap in combination with an increasing-field Zeeman slower loaded magneto-optical trap (MOT) is used. The sequence starts with an 8 s long MOT loading phase where the 160°C hot atom beam from the Rubidium oven is slowed in a Zeeman slower [112, 113] and trapped in the MOT. The magnetic fields for the MOT are generated by small currents of 19.6 A in the pinch coils (see Figure 2.2 and explanation of the cloverleaf trap later in this chapter), generating an axial gradient of 19 G/cm and a radial gradient of 9.5 G/cm. A

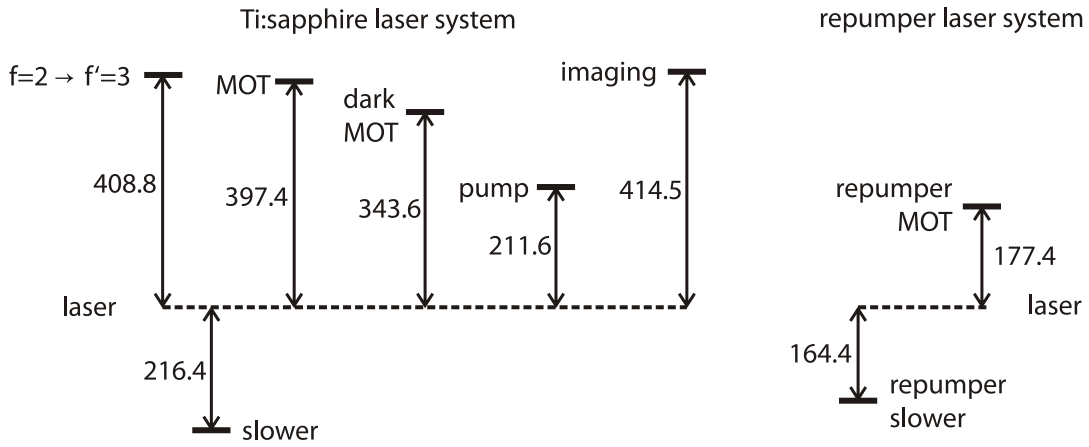

Figure 2.1: Relative frequencies in MHz of the laser beams necessary for cooling and trapping. The Ti:sapphire laser is locked via polarization spectroscopy 408.8 MHz below the ($f = 2 \rightarrow f' = 3$) transition and divided into four beams. The cooling beams (MOT and dark MOT), the beam for optical pumping, for absorption imaging and for the Zeeman slower (see text for details) are shifted by double pass AOMs to the respective frequencies. The laser for the repumping beams for the MOT and for the Zeeman slower is a diode laser locked via polarization spectroscopy to the ($f = 1 \rightarrow f' = 1$) transition and shifted via double-pass AOMs to the Zeeman shifted repumper transition $5s_{1/2}$ ($f = 1 \rightarrow f' = 2$) in the respective magnetic fields of the MOT and the Zeeman slower.

Titanium-Sapphire laser system (Ti:sapphire) (Figure 2.1) provides the six MOT beams with a detuning of about 2Γ and intensities of $9.5 \cdot I_{\text{sat}}$ radially and $5.1 \cdot I_{\text{sat}}$ axially, driving the cooling transition $5s_{1/2}$ ($f = 2 \rightarrow f' = 3$) in ^{87}Rb with a natural linewidth of $\Gamma = 2\pi \times 6.1\,\text{MHz}$ and a saturation intensity of $1.6\,\text{W/m}^2$ [78]. The same laser is used for the slowing beam in the Zeeman slower. The cooling transition is not a perfectly closed transition, hence atoms decaying to the $f = 1$ state have to be pumped back. A diode laser system drives the repumper transition $5s_{1/2}$ ($f = 1 \rightarrow f' = 2$) and pumps atoms to the $f' = 2$ state. From there they can decay back to the $f = 2$ ground state and into the cooling transition. The diode laser also provides a repumper beam for the Zeeman slower. The relative frequencies of the beams are shown in Figure 2.1.
After loading of the MOT the slower is turned off and a mechanical shutter prevents the atom beam to heat the trapped atoms. In the MOT the atoms experience a repulsive force due to reabsorption of scattered photons (radiation trapping) [114]. This force equals the trapping force at some atom density and a further increase of the number of trapped atoms will only increase the size of the cloud. This limitation can be circumvented by a dark MOT phase [115, 116], where the intensity of the repumper light is reduced to about $0.01\,\text{W/m}^2$. This collects atoms in the dark hyperfine ground state that is independent of the cooling light. At the same time, the magnetic field gradients are reduced to 10.2 G/cm axially and 5.1 G/cm radially at a current in the pinch coils of

10.5 A and the detuning of the MOT light is increased to about 10Γ. Thereby the number of scattered photons and with it the repulsive interaction due to radiation trapping is reduced and higher densities are achieved, advantageous to efficiently load the atoms into the magnetic trap. Also the trapping forces are smaller than in the MOT phase but as no further atoms are loaded into the trap and only cold atoms are confined smaller forces are sufficient.
Next in the experimental sequence the magnetic field for the MOT is completely turned off to further cool the atoms for 5 s in a molasses phase [117] before the magnetic trapping fields are turned on and the atoms are transferred into a shallow magnetic trap first before the trap is compressed to increase the density. In the magnetic trap the atoms experience a potential due to their magnetic moments, depending on the magnetic substate. Therefore the unpolarized atoms from the MOT and molasses have to be optically pumped into the $f = 2$, $m_f = 2$ state. The circularly polarized pumping light is also generated by the Ti:Sapphire laser system (Figure 2.1). About 8×10^8 atoms can be transferred from the molasses to the magnetic trap at a final temperature of 350 μK in the compressed magnetic trap. The additional dark MOT phase decreased this temperature in the magnetic trap by a factor of two compared to the experimental situation before [110].
A schematic of the setup is shown in Figure 2.2. Due to the symmetry of the magnetic trap the z-axis is called the axial direction whereas the x- and y-axes form the radial direction. The magnetic trapping fields are generated by a set of coils in cloverleaf configuation [118, 119]. In this configuation only coils in one plane in the setup (the x-y-plane) are needed, allowing full 2π optical access in the symmetry plane of the setup, only limited by the vacuum chamber. Two 'pinch coils', creating an axial trapping, are surrounded by four 'cloverleaf coils' each. Figure 2.2 (b) shows the arrangement of these coils, reminiscent of a four-leaf clover. It creates a local minimum in the magnetic field strength at the symmetry point inbetween the two sets of coils. However, this minimum is at a high magnetic offset field that is compensated for by two additional 'bias coils' in Helmholtz configuation. The setup is optimized to result in a small offset magnetic field. This bias field is ideally about $B_0 = 1$ G if the pinch and bias coils are connected in series at a current of 400 A. Details about the trap design and the current control can be found in [110]. Due to misalignments of the coils the bias field is 13.55 G in the experiment, if it is not compensated by additional magnetic fields.
After loading the atoms into the magnetic trap the temperature of the cloud is reduced and the density increased by evaporative cooling. A radio frequency source drives transitions between the m_F and $m_F \pm 1$ substates of the $f = 2$ ground state atoms, that are splitted in the magnetic field. The radio frequency is scanned from 45 MHz down to about 1 MHz in 38 s and transfers atoms to untrapped $m_F \leq 0$ states. Since the splitting between m_F and $m_F \pm 1$ increases with the magnetic field strength, atoms are lost from the high magnetic field regions that can only be reached by the hottest atoms.

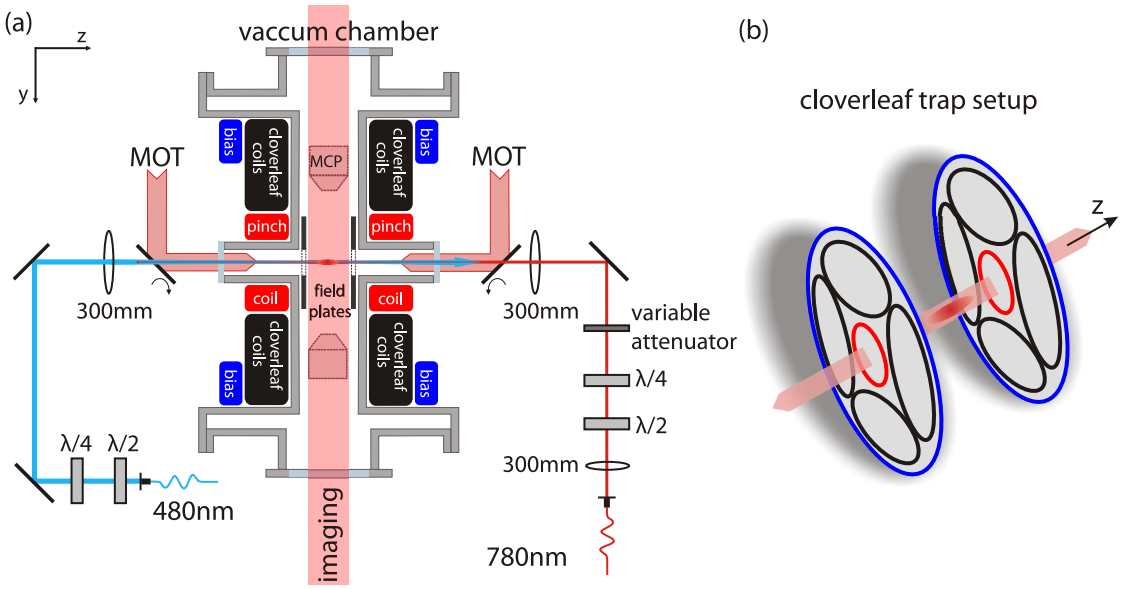

Figure 2.2: (a) Schematic of the vacuum chamber, coil assembly, cooling, imaging and excitation light in the y-z plane. The cloverleaf geometry of the 12 coils lies in the radial plane (x-y plane). The trapped atoms form a cigar-shaped cloud with the symmetry axis along the axial direction (z-axis) in the middle of the vaccum champer. Along this axis two MOT beams, but also the Rydberg excitation beams, propagate. The beam for absorption imaging lies in the y-axis. The field plates and the ion detectors (MCP) are inside the vacuum chamber and shown in Figure 2.6 in detail. (b) Coil assembly of the cloverleaf trap. The inner (outer) coils are the pinch (bias) coils, centered on the symmetry axis of the trap (z-axis). The eight clover leaf coils are off axis.

This loss of hot atoms reduces the temperature of the remaining, rethermalized cloud. Because of the necessary rethermalization during the cooling process, evaporative cooling is most efficient at high atom densities that can be achieved in a tight trap at small bias fields in this setup. An additional current in the bias coils is applied that compensates for the misalignment of the coils and reduces the bias field to 1 G for the evaporative cooling. After this cooling sequence the cloud consists typically of about 4.5×10^6 atoms at a density of $1 \times 10^{13}\,\mathrm{cm}^{-3}$ and a temperature of $4.5\,\mu\mathrm{K}$. If the evaporative cooling is continued the phase transition to a Bose-Einstein condensate can be crossed in this apparatus. The radio frequency also populates the $(f = 2, m_f = 1)$ state, which is also trapped. Atoms in this state generate additional signals in the Rydberg spectroscopy in chapter 3.

The atom density can be varied after cooling by a Landau-Zener sweep [120, 121]. A microwave is ramped through the resonant frequency of about 6.8 GHz between the trapped $5s_{1/2}$ $f = 2$ state and the untrapped $f' = 1$ state, effectively removing atoms from the cloud. The fraction of adiabatically transferred atoms can be adjusted by the ramp time to vary the atom density.

After evaporative cooling the magnetic offset field can be varied by reducing the additional current in the bias coils to adiabatically change the magnetic offset field to values between 1 G and 13.55 G. The radio frequency is increased from its minimum value at the same time to adjust for the increased Zeeman splitting of the ground state. It serves as a radio frequency knive to remove hot atoms. The offset field also changes the trap frequencies (see [112]). The higher the offset field B_0 the shallower the trap which means that the density and the temperature of the atoms are reduced if the offset magnetic field is ramped up. Usually the magnetic offset field was measured in this experiment by microwave spectroscopy between the trapped ($f = 2$, $m_f = 2$) state and the untrapped ($f = 1$, $m_f = 1$) ground state [73]. Here, Rydberg spectroscopy was used (Figure 3.3), as it was found to give more accurate and faster measurements of the magnetic offset field.
Most experiments in this thesis are performed at the highest experimentally possible offset field of 13.55 G. This is advantageous in respect of Rydberg interactions, as will be discussed in chapter 3, but also because no additional current in the bias coils is applied, reducing the magnetic field noise and instability. At this field the trap frequencies were measured to be $\omega_z = 2\pi \times 16.6\,\mathrm{Hz}$ and $\omega_r = 2\pi \times 85.1\,\mathrm{Hz}$. Even though clear differences of the used trap to the ideal cloverleaf situation exist, visible in the high bias field, a cigar-shaped harmonic trapping potential with the measured trapping frequencies is present. For the trapped cloud the $1/\sqrt{e}$-width σ_i ($i = r, z$)

$$\sigma_i = \frac{1}{\omega_i}\sqrt{\frac{k_B T}{m}} \tag{2.1}$$

can be calculated from the measured temperature and the peak density ρ of the Gaussian density distribution

$$\rho = \frac{N}{(2\pi)^{3/2}\sigma_r^2\sigma_z} \tag{2.2}$$

can be calculated from the atom number N. After ramping the magnetic field to 13.55 G typically 3×10^6 atoms at a temperature of 700 nK are in the trap, leading to widths of $\sigma_r = 15.3\,\mu\mathrm{m}$ and $\sigma_z = 80.7\,\mu\mathrm{m}$ and a peak density of $2 \times 10^{12}\,\mathrm{cm}^{-3}$.
The measured atom numbers and the temperatures of the sample are obtained by time-of-flight (TOF) measurements [110]. These can either be performed by fluorescence measurements in big, usually hot samples or by absorption imaging. The absorption of a resonant beam in y-direction (Figure 2.2) is measured using a CCD camera after passing through the chamber.

2.2 The Rydberg excitation and detection

Rydberg excitation of the ultracold atoms from the $5s_{1/2}$ ground state to Rydberg ns and nd states is done by direct two-photon excitation, 400 MHz blue detuned from the

intermediate $5p_{3/2}$ state to preserve the coherence in the excitation process, as shown in Figure 2.3. I will only briefly describe the laser setup, more details can be found in [73, 122, 123].
Two laser systems (Figure 2.4), consisting of extended cavity diode lasers in master-slave configuration each, are used to provide light at 780 nm for the lower transition and at 960 nm, which is subsequently frequency doubled to generate light at 480 nm for the upper transition. Both master lasers are stabilized to a passively stable cavity via a Pound-Drever-Hall locking scheme to a linewidth of below 20 kHz each. The total linewidth of the two-photon transition was measured to be 60 kHz. Temperature drifts of the setup result in considerable frequency drifts of up to 30 kHz/min for the two-photon transition to the Rydberg state, as shown in Figure 2.5. Double-pass AOMs between both master and slave lasers are used to shift and scan the excitation frequencies without intensity fluctuations in the experiment. For spectroscopy in ultracold gases the 780 nm light is scanned over a range of up to 60 MHz. Additional single-pass AOMs can switch both beams within 10 ns before they are coupled into optical fibers, directing the excitation light to the main experimental setup. Excitation times between some tens of nanoseconds up to some tens of microseconds per pulse are realizable, where various pulses can be combined to excitation pulse trains.
In Figure 2.2 (a) the red and blue excitation light in the vacuum chamber is indicated. The beams are counter propagating in the axial direction to reduce the Doppler width and focused into the chamber to $1/e^2$-diameters of 500 μm and 85 μm, respectively, at the position of the atoms. The power of the blue beam is 70 mW, the used red power in this work is up to 10 μW to realize two-photon Rabi frequencies of up to $\Omega_0 = 2\pi \times 100\,\mathrm{kHz}$. The red power and simultaneously the two-photon Rabi frequency can be varied by a variable attenuator in the red beam (Figure 2.2). The polarizations of the Rydberg excitation beams are adjusted using $\lambda/2$ and $\lambda/4$ waveplates directly after the fibers (Figure 2.2) to access ns and nd states, as shown in Figure 2.3. However, in the inhomogeneous fields in the magnetic trap the polarization is not well defined for the whole atomic cloud and excitations to different states do also appear.
The excitation is directly followed by field ionization where high voltages are applied to the field plates B (2 kV) and H (2.5 kV) inside the vacuum chamber, shown in Figure 2.6. Strong electric fields are generated that ionize the Rydberg atoms, but not the ground state atoms. The generated ions are pushed towards the ion detector, a multi channel plate (MCP), and detected. From the amplified MCP signal the Rydberg atom number created by the excitation pulse sequence is obtained. Details can be found in [101, 122]. The field ionization is not state selective in this experiment and only the total number of atoms excited to Rydberg states $n \gtrsim 30$ can be measured.
Even though the rise time of the fields is about 20 ns and the time of flight of the ions is below 1 μs the whole sequence of ionization and detection takes about 8 ms, where most time is spent to allow for the electric fields to decay. Thereafter the whole sequence of

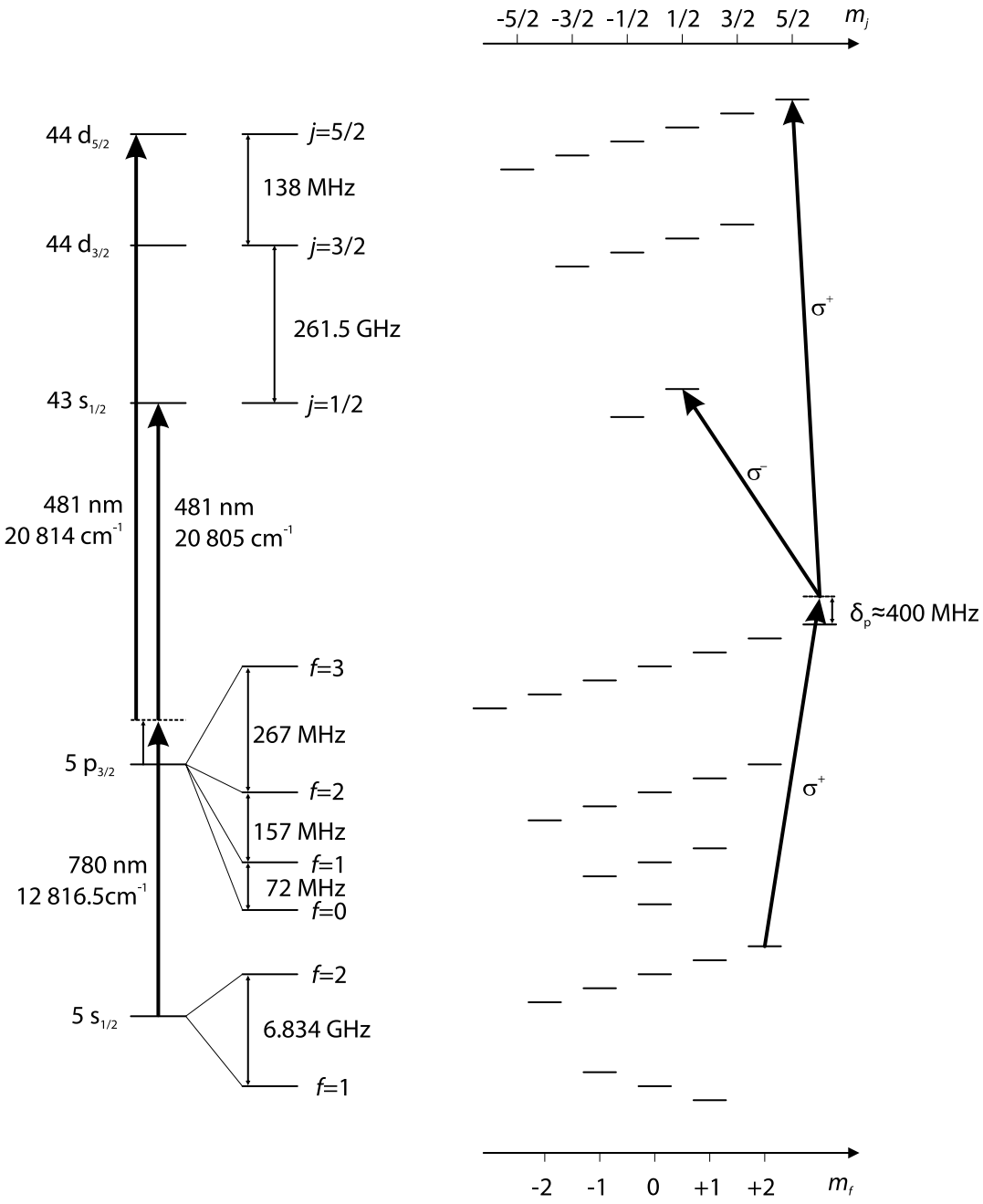

Figure 2.3: Level scheme of the finestructure, hyperfine structure and magnetic field splitting (from left to right) of the relevant atomic levels of ^{87}Rb. The Rydberg states 44d and 43s only show negligibly small hyperfine splittings that scale as $(n^\star)^{-3}$ [69, 72] and are described in the j, m_j-basis, whereas 5s and 5p are described in f, m_f-basis. The ideal excitation paths to s and d states are indicated on the right hand side and differ in the polarization of the upper transition. Details about the magnetic field dependence can be found in chapter 1.2.3.

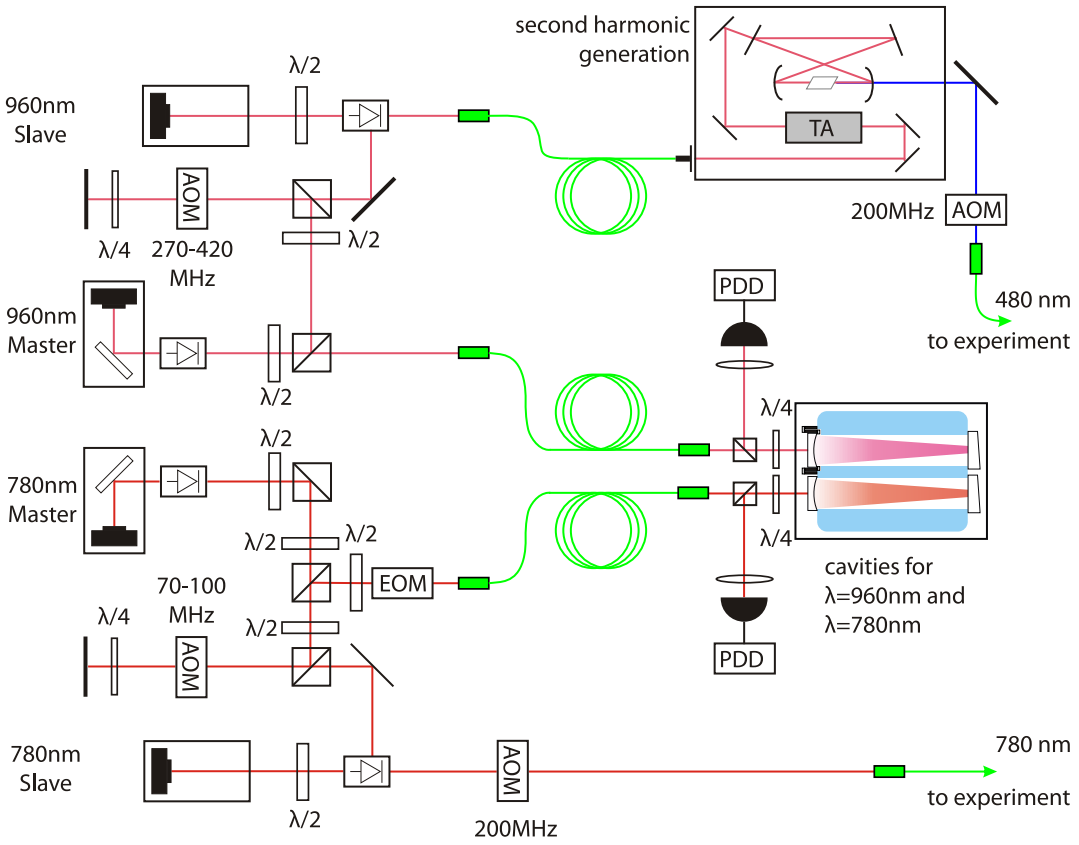

Figure 2.4: Laser system for the two-photon Rydberg excitation including two master-slave laser systems at 780 nm and 960 nm, passively stable resonators for Pound-Drever-Hall locking schemes (PDD), AOMs for frequency shifts and a second harmonic generation setup, including a tapered amplifier (TA), for frequency doubling to generate 480 nm light.

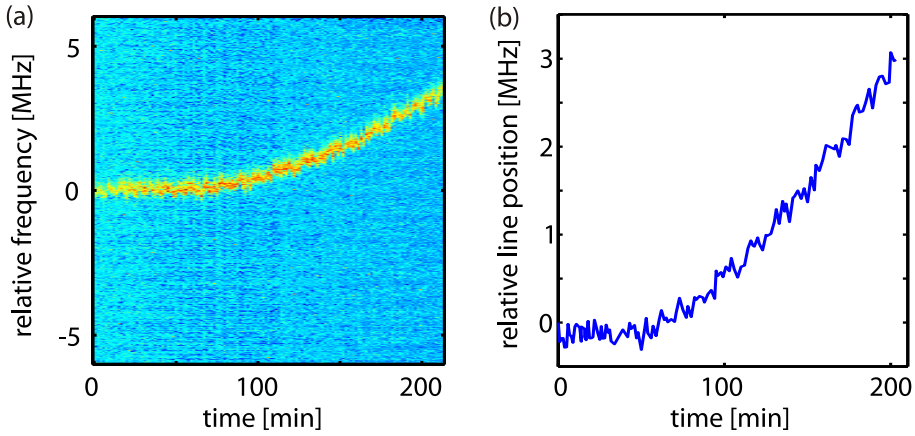

Figure 2.5: Frequency drift of the Rydberg excitation line versus time. (a) shows the color coded spectroscopy data and (b) the extracted relative line position. At time = 0 min the experiment was turned on, clearly followed by a frequency drift of the locking point, probably due to a changed temperature in the lab, changing the resonance frequency of the cavity.

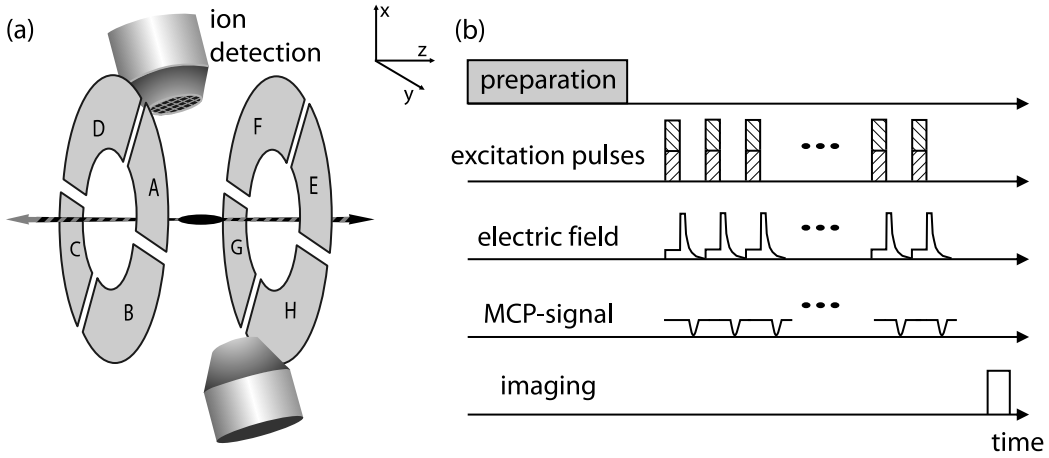

Figure 2.6: (a) Setup of the field plates and ion detectors inside the vacuum chamber. The plates B and H are used for field ionization, A and C for applying small electric fields during the excitation. The lower ion detector is not used. (b) Sequence of preparation (cooling and trapping of atoms), excitation, ion detection and absorption imaging. The time axis is not to scale.

excitation and detection can be repeated. As only a very limited fraction of atoms is excited to the Rydberg state, typically about 10^{-4}, 401 sequences are performed in a series within one cloud in these experiments. During these 3.2 s of Rydberg excitation and detection the cloud is not severely heated and no additional cooling is necessary. This results in an average repetition rate of 8 Hz, even though the evaporative cooling sequence in this experiment is long.
During the excitation additional electric fields can be applied to the remaining six field plates. To create an almost homogeneous field along the axial direction (parallel to the offset magnetic field) the field plates A and C are used. Versatile voltage sequences up to 10 V can be applied by an arbitrary waveform generator[1] with a rise time of 30 ns.

In conclusion, this experimental setup offers narrowband laser excitation to Rydberg states in dense and ultracold samples. The density and the magnetic offset field can be controlled and electric fields can be switched in arbitrary sequences during the excitation. This provides ideal situations for coherent control of Rydberg interactions and for the creation of ultralong-range Rydberg molecules. However, despite absorption imaging of ground state atoms to obtain temperatures and densities of ultracold atoms, the only observable in the case of Rydberg atoms is the total Rydberg atom number. This necessitates that every demanded quantity of the Rydberg atoms has to be mapped onto the Rydberg atom number to be measureable. Spectroscopy with complex pulse sequences can realize it in this setup, based on the possible high number of excitation and

[1] Keithley 3390

detection cycles within one atomic sample, the narrowband excitation and the flexible control of the excitation pulse sequence and electric field sequence.

3 Coherence at Förster resonances

Understanding the fundamental interactions between single atoms lies at the heart of physics. The area of ultracold atomic physics goes even further and aims at coherent control of interactions. This is of great interest as ultracold strongly interacting atoms can serve as model systems for correlated quantum many-body physics, for example in quantum computing [8, 57, 124] but also in order to understand nature [51]. Very promising candiates in this respect are Rydberg atoms with strong and tunable interactions, for which many proposals for quantum information processing [39, 40, 41] and simulation [13] exist. Especially in quantum computing strong progress has been achieved in the last years with the realization of two-qubit gates with neutral atoms using the Rydberg blockade [42, 43, 44]. Another possibility to realize quantum computing with neutral atoms is the phase gate [40], that relies on a controlled interaction-induced phase shift in the atoms.
Furthermore coherent Rydberg interactions are expected to not only create exotic ground states and quantum phase transitions [125] but also realize quantum dynamics, for example in coherent energy transport in strongly correlated many-body systems [18, 29]. In biophysics these non-radiative exciton dynamics are relevant for photosynthesis in certain biological systems [51] and might be modeled using strongly interacting ultracold atoms [34].
One promising possibility to induce and control interactions between Rydberg atoms are Förster resonances. Coherence at Förster resonances has been studied by means of Ramsey techniques in the coupling between pair states [28] and by direct observation of Rabi oscillations between the ground and the Rydberg state [26]. Still, complete coherent control and a full understanding of the decoherence mechanisms, especially in the case of a macroscopic ensemble of interacting atoms, remains an open field.
In this chapter I will present experiments realizing coherent control of the electronic state and the phase of an ensemble of ultracold atoms. Furthermore I will present experiments resolving several Förster resonances to an unprecedented accuracy in the Förster defect and study the coherence at these resonances. The results show that coherent coupling between the involved pair states in the presence of strong interactions is possible, but also they show additional sources of dephasing. Still, it can be shown that a coherent, interaction-induced phase shift of the atoms is possible. This realizes coherent control

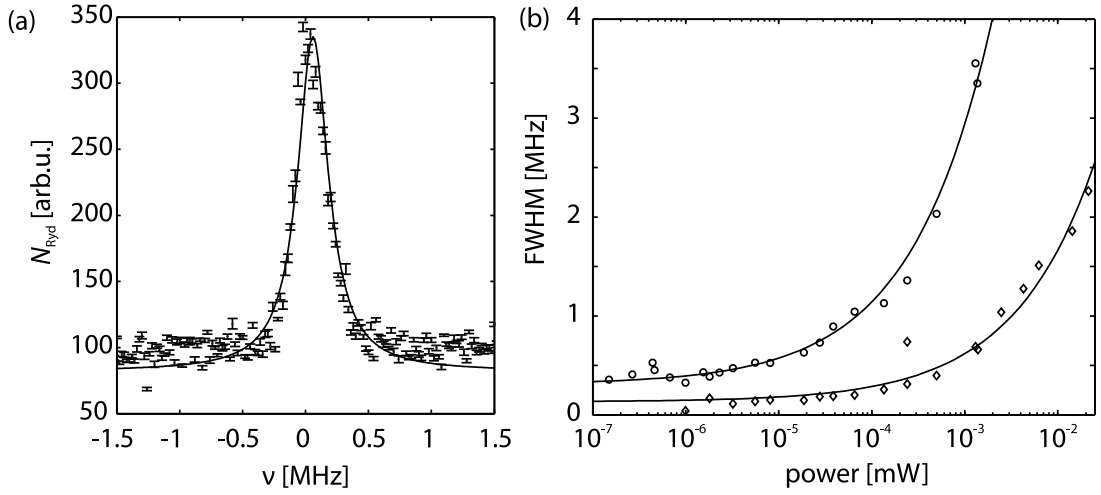

Figure 3.1: Linewidth measurement for the $43s_{1/2}$ and $44d_{5/2}$ state. a) shows the excitation spectrum of the 44d state at the lowest Rabi frequency of about 1 kHz (data points, averaged over 10 measurements). The solid line is a lorentzian fit to the data, resulting in a linewidth (FWHM) of 300 kHz. b) Dependence of the FWHM on the red excitation power for the 43S (diamonds) and 44d (circles) and a square root fit to guide the eye.

of the interaction, where the strength and the sign of the interaction, from attractive to repulsive, can be easily tuned.

Coherent control is limited to timescales given by the coherence times. Ultimately, they are limited by the excitation linewidth to the Rydberg states. To measure the excitation linewidth spectra consisting of 401 Rydberg excitation measurements with excitation times of 20 μs were taken in a magnetic offset field of 13.55 G. A detailed description of the excitation and detection sequence can be found in chapter 2.2. Figure 3.1 (a) shows such a spectrum of the $44D_{5/2}$, $m_j = 5/2$ resonance at the lowest possible Rabi frequency of about $2\pi \times 1$ kHz (limited by the detection efficiency) together with a lorentzian fit to obtain the linewidth. Power broadening increases the linewidth with increasing intensity of the 780 nm excitation laser, that is driving the lower part of the two-photon excitation to the Rydberg state, and the linewidth follows the Rabi frequency $\Omega_0 \propto \sqrt{I}$, as seen in Figure 3.1 (b). The square root fit shows that this proportionality is nicely reproduced in the experiment. From an extrapolation to negligible intensities the minimal linewidth was obtained to be $\Delta\nu = 300$ kHz for the 44d state. The 43s state shows a considerably smaller linewidth of 110 kHz.

Several mechanisms can account for the linewidth, e.g. the lifetime of the excited state or the linewidth of the excitation lasers, but also effects like Doppler broadening or magnetic and electric field broadenings. The lifetime of the Rydberg state is on the order of 50 μs for the 44d state [126], creating a natural linewidth of 3 kHz. This is considerably smaller than the linewidth of the lasers that was measured to be about 60 kHz, and the

Doppler broadening of about 20 kHz at 700 nK for counter propagating red and blue excitation lasers [122]. Thus, the natural linewidth and the Doppler broadening alone do not explain the observed linewidth. Instead, the excitation to the 44d state shows stronger dependencies on the magnetic and electric fields as the 43s state, that can explain the observed broadening and are discussed in the following.
In a magnetic trap the atoms experience a spatially dependent magnetic field. This can lead to differential Zeeman shifts for transitions between different states, as shown in Table 1.3. Transitions between the ground state with l=0 and an s Rydberg state do not show this differential shift. But the transition to Rydberg d states is dependent on the magnetic field with a differential Zeeman shift of $2\,\mu_B B$. In a magnetically trapped cloud this creates a broadening of the transition depending on the temperature of the atoms. For a temperature of 700 nK one calculates a width of 50 kHz.
Inhomogeneous electric fields or noise in the electric field broadens the excitation spectrum as well. The ground state shows only a small dependence on the electric field and the differential Stark shift of the excitation transition can directly be calculated from the polarizabilities of the Rydberg states (Table 1.2). The 44d state experiences a five times stronger broadening by electric fields as the 43s state. For a realistic estimate of the electric field variation of 0.001 V/cm (for electric field noise as well as for the inhomogeneity of the field) one obtains broadenings on the order of 50 kHz at offset electric fields in the order of 0.5 V/cm.
In conclusion, the observed broadened linewidth of $\Delta\nu = 300\,\text{kHz}$ of the 44d transition compared to the narrower 43s transition can be explained by a combined effect of the stronger dependence on electric fields and the magnetic field broadening. The coherence times are limited to $T < \frac{1}{2\pi\Delta\nu} = 0.53\,\mu\text{s}$. In the experiments here also the 43s excitation shows a broadened minimal linewidth of 110 kHz compared to earlier experiments at low magnetic offset fields, where a linewidth of 60 kHz was measured [73]. This discrepancy can be attributed to the larger extent of the atomic cloud at higher magnetic offset fields that result in a stronger sensitivity on electric field inhomogenities.
Other sources of dephasing are couplings to additional atomic states. In the experiments here, an offset magnetic field bigger than 0.5 G in the magnetic trap is unavoidable. This leads to a Zeeman splitting of the magnetic substates. If the splitting is smaller than the linewidth of the excitation, all states can be excited which will lead to a dephasing. The magnetic field has to be strong enough so that the Zeeman effect clearly exceeds the excitation linewidth. For pulsed experiments the Fourier-broadened linewidth can reach several MHz, necessitating offset magnetic fields on the order of some Gauss.
Additional to the magnetic field an electric field of about 0.2 V/cm is needed to shift pair states into resonance to create Förster resonance conditions, as explained in chapter 1.3.3. The atoms experience a Zeeman and a Stark shift which can create crossings between different m_j-levels. To shift these crossings to electric fields outside the experimentally interesting range again a big magnetic offset field is needed. The experiments

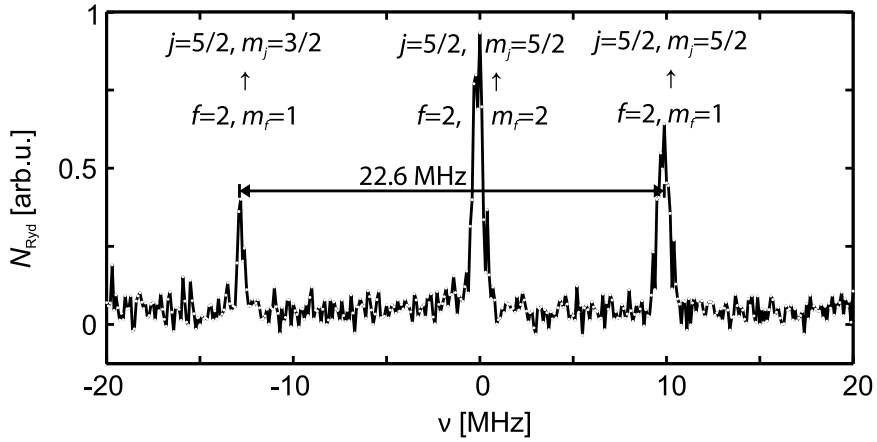

Figure 3.2: Excitation spectrum showing the transitions from the $5s_{1/2}$ ($f = 2$, $m_f = 1$) ground state to the $44d_{5/2}$ $m_j = 3/2$ (left peak at -18.8(1) MHz) and $m_j = 5/2$ (right peak at 9.9(1) MHz) states and from the $5s_{1/2}$ ($f = 2$, $m_f = 2$) to the $44d_{5/2}$ $m_j = 5/2$ state (cf. level scheme in Figure 2.3) at the highest experimentally realizable magnetic offset field in zero electric field.

in this thesis are performed at the highest experimentally possible offset magnetic field. To calibrate the offset magnetic field the Zeeman splitting of the $44d_{5/2}$ substates $m_j = 5/2$ and $m_j = 3/2$ was spectroscopically measured. The transition from the $m_f = 2$ ground state to the $m_j = 3/2$ Rydberg state is suppressed by the polarization of the excitation light (see Figure 2.3). This is not the case for transitions from the $m_f = 1$ ground state, that is unintentionally populated by microwave transitions during evaporative cooling, making this unwanted peculiarity actually profitable for a fast calibration of the magnetic field. Hence, spectroscopy of ground state atoms in the $5s_{1/2}$ ($f = 2$, $m_f = 1$) state in a pure magnetic field was used for calibration, as shown in Figure 3.2. From the differential Zeeman shift of $1.2\,\mu_B B$ (Table 1.3) the magnetic field is obtained to be 13.55(6) G.

To study the single-atom shifts in combined electric and magnetic fields single-pulse spectra of 20 μs were taken in variable electric fields at the magnetic offset field of 13.55 G, resulting in the two-dimensional Stark map in Figure 3.3. Several transitions are resolved in the spectroscopy signal. They adiabatically connect to the transitions from the $5s_{1/2}$ ($f = 2$, $m_f = 2$) ground state to $44d_{5/2}$, $m_j = 5/2$ (0 MHz), $44d_{5/2}$, $m_j = 3/2$ (-22 MHz) and $44d_{5/2}$, $m_j = 1/2$ (-45 MHz) in zero electric field. The additional resonance at -13 MHz is a transition from the $5s_{1/2}$ ($f = 2$, $m_f = 1$) ground state to $44d_{5/2}$, $m_j = 3/2$. These splittings are sufficient that a single Rydberg state can be excited even in the pulsed experiments in this thesis.

With increasing electric field the states experience differential Stark shifts, resulting in degeneracies at certain electric fields. For a finite angle between $\vec{E}$ and $\vec{B}$ these levels couple and avoided crossings appears, as it can be seen in Figure 3.3. This effect is

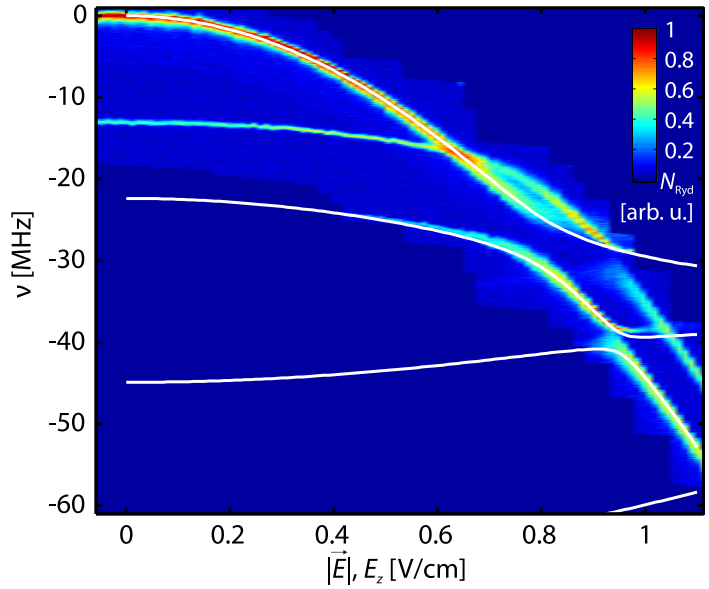

Figure 3.3: Stark map of the 44d state and calculations for B = 13.55 G at an angle of $\theta_{EB} = 15°$ between the electric and magnetic field. The calculations (white lines) are plotted versus the total electric field $|\vec{E}|$. The measured spectra are plotted versus the applied electric field E_z and the normalized Rydberg atom number N_{Ryd} is color coded.

described in chapter 1.4 and in detail in [73]. As a single-atom effect it can easily cover binary interaction effects and it leads to a dephasing of the single-atom states. However, at 13.55 G the single-atom crossings are shifted to electric fields of 0.7 V/cm, far outside the experimentally interesting regime of about 0.2 V/cm.
The white lines in Figure 3.3 are calculated by diagonalizing the single atom Hamiltonian (1.32) at 13.55 G offset field and an angle of $\theta_{EB} = 15°$ between the electric and the magnetic fields. This measurement is also used to calibrate the electric field by finding the best agreement for the quadratic slope of the $m_j = 5/2$ state between the experiment and the calculation. Since the Stark effect $\Delta E_{\mathrm{Stark}}$ is in good approximation quadratic in the total electric field $|\vec{E}|$,

$$\Delta E_{\mathrm{Stark}} = -\frac{\alpha}{2}|\vec{E}|^2 = -\frac{\alpha}{2}(E_z^2 + E_r^2), \tag{3.1}$$

where α is the polarizability, a constant radial electric field E_r will lead to a constant energy shift. This gives an offset in the Stark map that cannot be detected in the experiment. Hence only the electric field E_z in one direction can be calibrated. From the size of the avoided crossing the angle θ_{EB} can be obtained. The best agreement was found at $B = 13.55$ G and an angle of $\theta_{EB} = 15°$, as shown in Figure 3.3.

3.1 Coherent control of Rydberg atoms

Studying the coherence of a system is a challenging task, as the coherence is no observable. Here, as in most Rydberg experiments, the Rydberg atom number is measured and the coherence properties of the atoms have to be mapped onto the atom number. Several approaches exist, for example rotary-echo experiments [27, 127] or direct observation of Rabi oscillations. All of these approaches offer information about coherence times and can study dephasing and decoherence mechanisms, but they suffer from various disadvantages. In rotary echo experiments the phase of the atoms is not measured and some information about the coherent evolution is lost. The latter approach is limited to special systems where the Rabi frequency of the driving excitation field is spatially constant [128], a complicated task due to the collective nature of the Rydberg excitation (chapter 1.3.8). It can be realized in single atom systems [129] or with great technical effort in macroscopic samples [26].
Another type of experiments to study coherence are Ramsey experiments with the advantage to gain insight into both, decoherent but also coherent processes in strongly interacting Rydberg gases. Ramsey experiments are well suited as the level of coherence and the phase of the atoms is interferometrically mapped onto the state of the atoms and thereby onto the Rydberg atom number. Norman Ramsey's idea [130], already formulated in 1950, relies on separated oscillatory fields. In the original experiment the two fields were spatially separated and a molecular beam passed through the fields one after another. This idea can be expanded also to a pulsed experiment where the separation is not in space but in time.
Ramsey experiments have been applied to Rydberg systems to study coherence in single-atom traps [131], in the energy transfer between pair states in a MOT [28], in resonant microwave coupling of Rydberg atoms [132] and in the photoassociation of ultralong-range Rydberg molecules [93]. Here I will use Ramsey methods to study the coherent two-body dynamics at a Förster resonance.

3.1.1 An optical Rydberg Ramsey interferometer

The basic idea behind Ramsey experiments is the following: First the oscillating field couples two atomic states shortly. After some time, where the system can evolve, the states are probed by a second coupling field. Interference effects appear, resulting in the classical Ramsey fringes if the delay time between the two pulses or the detuning of the coupling field to the atomic resonance (Figure 1.2) are varied.
In chapter 1.1.2 the appearance of the fringes was derived from the time evolution of the atoms in the case of a two level system and understood as an atom interacting with a classical light field. However, these experiments can also be viewed as an atom interferometer [133]. The two states, coupled by the field, are the two arms of the

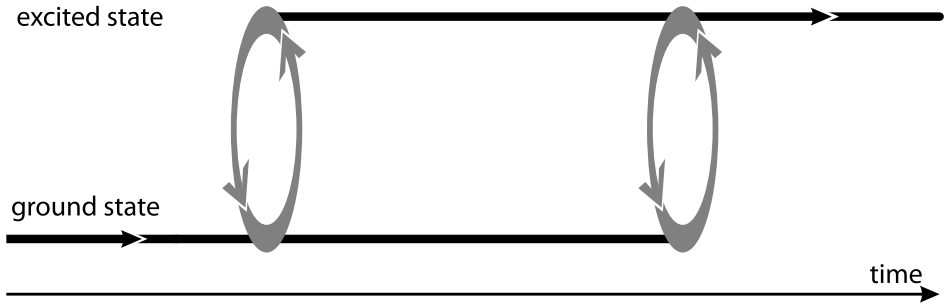

Figure 3.4: Schematic of the Ramsey interferometer. The system starts in the ground state and the pulsed coupling fields interfere the ground and excited state. After the Ramsey sequence the population in the excited state is detected.

interferometer and the field acts as a beam splitter when it couples the two states. In contrast to well-known setups as a Mach-Zehnder or a Michelson interferometer the splitting of the two beams does not happen in space, but in the electronic state of the atom. In absence of the coupling field and within the lifetime of the excited state the arms are not coupled and can evolve independently, as necessary for an interferometer. A schematic is shown in Figure 3.4. Here, the Ramsey sequence is realized by two optical excitation pulses coupling to a Rydberg state, separated by a variable delay time. After this sequence the Rydberg atom number is measured by field ionization and ion detection. Hence, if the delay time or the detuning is varied, oscillations in the Rydberg atom number will occur (see Figure 3.5 (a)).
Ramsey's method is advantageous to single pulse experiments in many aspects. It does not only offer the possibility of an enhanced resolution, it also is independent of spatial inhomogenities of the strength of the oscillatory field. This is important in the experiment here as the Rabi frequency is not constant over the sample. It spatially varies because of the Gaussian intensity profile of the exciting lasers and because of the density dependent enhancement of the collective excitation of Rydberg atoms (equation (1.54)). This gives rise to a suppression of direct Rabi oscillations [89]. Ramsey experiments, similar to rotary-echo experiments [27], can refocus this dephasing and are not sensitive to a spatially varying strength of the coupling field. Furthermore, interferometric Ramsey experiments offer phase sensitivity, providing the possibility to use them as a tool to study coherent effects by measuring the population in one arm only.
The Ramsey experiments in the following are done in a magnetically trapped and evaporatively cooled atomic cloud at a density of $1.2 \times 10^{12}\,\mathrm{cm}^{-3}$ and a temperature of $1\,\mu$K in a magnetic offset field of 13.55 G. To obtain spectra two short laser pulses (upper part of Figure 3.5 (b)) of $\tau_\mathrm{p} = 0.15\,\mu$s duration, separated by a delay time of $1\,\mu$s, are applied to the atoms. The Rydberg atom number is measured after the second light pulse. This sequence of excitation and detection is repeated 401 times in one atomic cloud. The excitation lasers are scanned from -6 MHz to +6 MHz relative to the atomic resonance

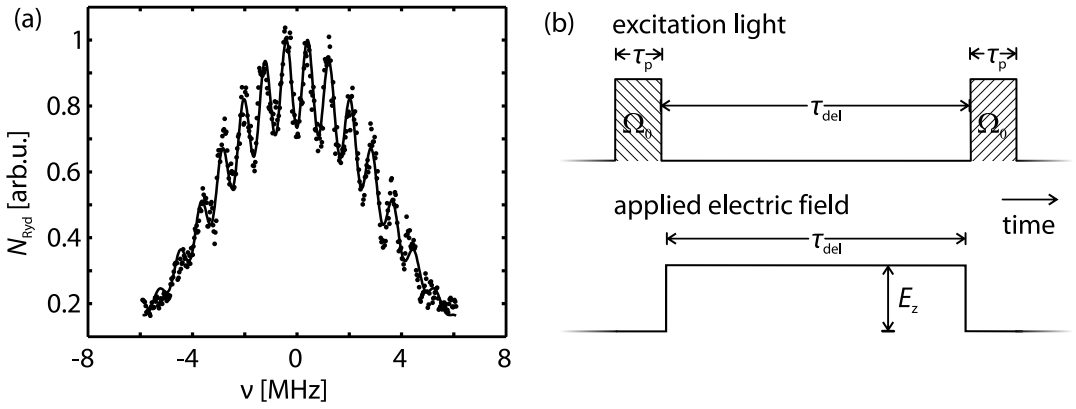

Figure 3.5: (a) single shot Ramsey spectrum for $\tau_\mathrm{p} = 0.15\,\mu$s, $\tau_\mathrm{del} = 1\,\mu$s and $E_z = 0.3\,\mathrm{V/cm}$ (dots) and least square fit to the data (solid line). ν is the detuning of the exciting laser relative to the atomic resonance. (b) Ramsey pulse sequence for the excitation light and for the electric field used as a phase shifter.

throughout these measurements. Thereby one entire Ramsey spectrum is measured in one atomic cloud in steps of 30 kHz, which is below the excitation line width. The single atom Rabi frequency is about $2\pi \times 100\,\mathrm{kHz}$ for the two-photon excitation.
Figure 3.5 (a) shows a typical Ramsey spectrum. The width of the signal of about 6 MHz is given by the Fourier width of the $\tau_\mathrm{p} = 0.15\ \mu$s long excitation pulses. Ramsey fringes in frequency space are clearly visible in these single shot data. No averaging over different atomic clouds is necessary.
The appearance of a Ramsey pattern in frequency space directly proves the coherence of the excitation process on the timescales of the experiment. More information about the coherent nature of the experiment can be obtained from the phase ϕ of the fringe pattern and the visibility V

$$V = \frac{\max(N_\mathrm{Ryd}) - \min(N_\mathrm{Ryd})}{\max(N_\mathrm{Ryd}) + \min(N_\mathrm{Ryd})}. \tag{3.2}$$

The phase of the Ramsey fringes offers an observable for coherent processes changing the time evolution of the atoms. Incoherent processes will not shift the phase. The visibility describes the depth of the Ramsey fringes and is a measure for the coherence in the system. Any loss of coherence will lead to less effective interference between the ground and excited state during the second Ramsey pulse and thereby reduce the visibility of the Ramsey fringes in the spectrum. However, from a single Ramsey spectrum dephasing and decoherence cannot be differentiated.
To extract these observables the Rydberg spectrum depending on the frequency of the

excitation laser $\omega = 2\pi \times \nu$ (Figure 3.5 (a)) is fitted by

$$N_{\mathrm{Ryd}} = a \cdot \mathrm{sinc}^2\left(\frac{(\omega-\omega_0)\tau_{\mathrm{p}}}{2}\right) \cdot \left(\frac{2V}{1+V}\cos^2\left(\frac{(\omega-\omega_0)(\tau_{\mathrm{d}}+\tau_{\mathrm{del}})}{2}+\phi\right)+\frac{1-V}{1+V}\right)+N_0, \tag{3.3}$$

including seven free fit parameters, following equation (1.16) obtained from the Optical Bloch equations (1.1.1) for the approximation $\Omega \gg (\omega - \omega_0)$ [73, 130]. Ω is the Rabi frequency, ω_0 an offset in the detuning, ϕ the phase of the Ramsey fringes, a is a scaling factor and N_0 an offset in the Rydberg population. The sinc^2-term describes the Fourier broadened envelope of the Ramsey spectrum whereas the cos^2-term accounts for the Ramsey fringes. As the approximation $\Omega \gg (\omega - \omega_0)$ is not fulfilled for the whole spectrum, deviations between the fit and the data for big detuning are visible. However, the function reliably reproduces the visibility and the phase of the Ramsey spectrum and is used throughout this thesis.

The visibility in the experiment is not only reduced by a loss of coherence of the atoms. It is also influenced by technical constraints, especially by the ion detection. The ion detector and the following amplifier show saturation with higher ion signals. This leads to a non-linear response of the ion detection and reduces the visibility for high Rydberg atom numbers. Figure 3.6 shows visibilities and maximal pulse areas of the ion detector signal at the 43s Rydberg line for varying powers of the 780 nm excitation laser. A rather weakly interacting s state was chosen to reduce the influence of interactions in this measurement. With higher excitation powers the pulse area increases, as expected due to the increased number of excited Rydberg atoms at higher Rabi frequencies. Similarly the visibility is reduced that can have several reasons, possibly a reduced coherence time due to power broadening of the excitation.

These measurements were repeated for otherwise constant experimental conditions with two different acceleration voltages (1750 V and 2000 V) applied between the front and the back of the ion detector, plotted in Figure 3.6. Higher acceleration voltages amplify the ion signal by an amplification of the secondary emission of electrons [122] and create stronger ion signals, as expected. Also a clear deviation in the visibility between both measurements is observed for powers above 10 μW, that corresponds to a maximum pulse area of about 1000 arb.u. While the overall loss of visibility with higher powers can have several reasons, this deviation can be attributed to the non-linear response of detector and amplifier. From this qualitative comparison of the data one can estimate that the influence of the detector does not dominate for spectra with a maximum pulse area of below 1000 arb.u. The following experiments in this thesis were done at an acceleration voltage of 1750 V and at excitation powers small enough to limit the pulse area to below 1000 arb.u. Because of this limitation the maximal possible Rydberg atom number in these experiments is limited to a value considerably below the maximum Rydberg fraction possible due to Rydberg blockade.

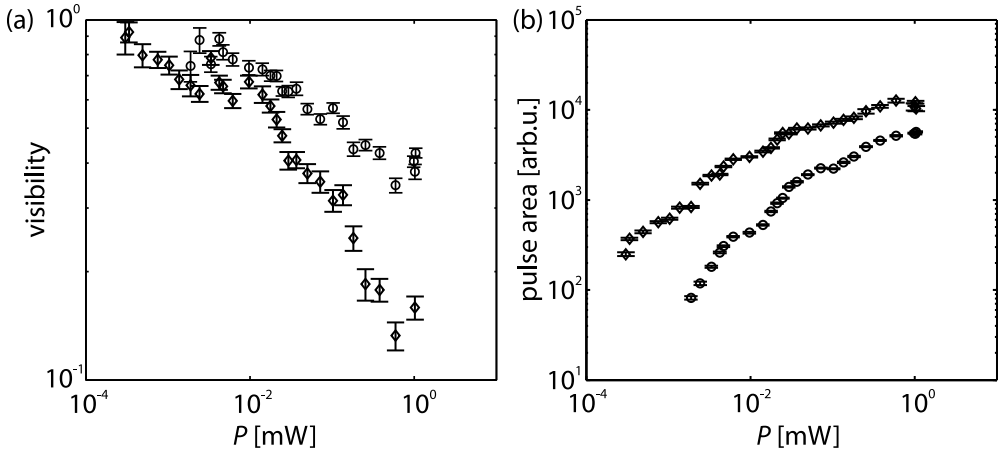

Figure 3.6: (a) Dependence of the visibility on the power P of the 780 nm excitation laser. Diamonds (circles) show measurements with an acceleration voltage of 2000 V (1750 V) at the ion detector (MCP). (b) shows the maximum pulse area of the detector signal for the same measurements. The unit of the pulse area follows the calibration of the atom number [134]. Due to aging of the MCP the actual Rydberg atom number probably differs, but the measurement at 2000 V acceleration voltage gives a rough estimate for the Rydberg atom number.

3.1.2 A controlled Stark-tuned phase shifter

Ramsey experiments realize atom interferometers, where the two paths of the interferometer are atoms in the ground state and atoms in the excited state. Even though the paths of the Ramsey interferometer are not separated in space, they can be distinguished via the Stark effect and phase shifts in only one path can be generated to control the relative phase in the interferometer.
Rydberg atoms show very strong Stark effects because of the large extent of the Rydberg electron wave function. In contrast, ground state atoms are rather insensitive to electric fields. The 44d state shows a quadratic Stark effect with a polarizability of $\alpha = 85.557(1)\,\mathrm{MHz/(V/cm)^2}$ (Table 1.2), orders of magnitude bigger than for ground state Rb-atoms with a polarizability of $0.0794(16)\,\mathrm{Hz/(V/cm)^2}$ [78]. Thus, in the interferometer the electric field can be seen as only affecting the Rydberg state.
If an electric field is applied during the delay time between the Ramsey pulses, as in the sequence in Figure 3.5 (b), a quadratic phase shift

$$\phi = -2\pi \int \frac{\alpha}{2} |\vec{E}(t)|^2 dt \tag{3.4}$$

accumulates between the Rydberg and the ground state atoms and generates a phase shift of the Ramsey fringes. The envelope of the Ramsey spectrum, however, is not shifted as the electric field is not present during the excitation.
Figure 3.7 shows such Ramsey spectra versus the pulsed electric field E_z. Every column shows a Ramsey spectrum consisting of 401 sequences of excitation and detection as

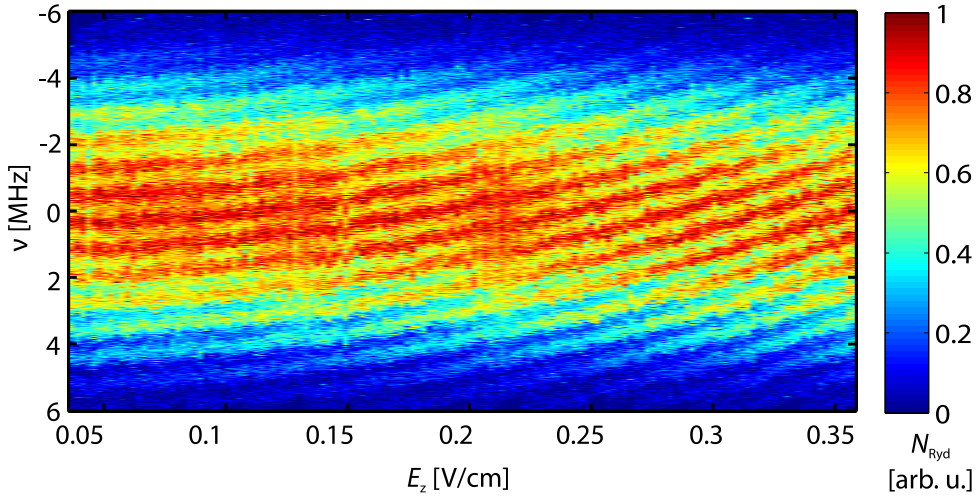

Figure 3.7: Color coded Ramsey spectra for varying pulsed electric fields. With increasing field a phase shift of the fringes occurs that depends quadratically on the electric field.

explained in chapter 2.2 and is measured in one atomic sample. To measure the influence of an electric field these measurements were repeated with varying electric fields between $E_z = 0.05\,\mathrm{V/cm}$ and $E_z = 0.36\,\mathrm{V/cm}$.
Clearly a quadratic phase shift of the fringes is visible in Figure 3.7. With increasing electric field the fringes are shifted towards smaller detuning, revealing the negative Stark effect of the Rydberg atoms. Even for electric fields of up to 0.36 V/cm, where phase shifts of 12π are realized, no loss of visibility is observed. As the visibility is a measure for the coherence in the system, this shows a remarkable stability of the coherence with respect to homogeneous fields. In a spatially constant electric field, the Stark effect acts as a homogeneous single atom effect. This does not disturb the coherence.
From a fit to every spectrum, as discussed in chapter 3.1.1, the phase ϕ can be obtained and is plotted in Figure 3.8. Due to historical and aesthetic reasons $-\phi$ is plotted versus the electric field, leading to quadratic increase in the plot. The measured phase shift can be compared to calculations of the phase shift of a $1\,\mu$s long electric square pulse, following equation (3.4). Apart from the phase in zero electric field, Figure 3.8 shows a perfect agreement between the calculated and the measured phase, showing the high precision of the electric field calibration. Nonetheless, a radial electric field does not contribute to the Stark effect here, just like for the Stark map in Figure 3.3.
The phase in zero electric field is expected to be zero, but a finite phase is obtained in the experiment. This has technical reasons in the experiment. One whole spectrum is measured in one atomic sample. Because of the field ionization in every sequence, but possibly also because of other loss mechanisms, the atom number is reduced from the beginning of each spectrum to the end, here towards bigger detuning. A quantitative analysis of this loss and its effect on the spectrum is difficult, but it effectively shifts the

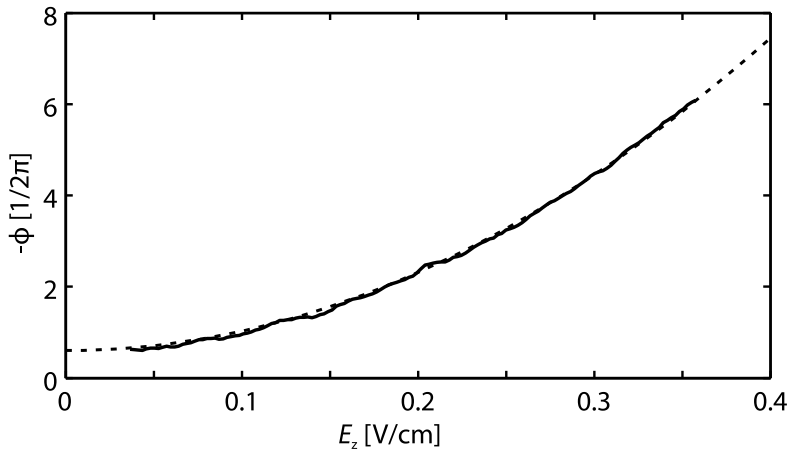

Figure 3.8: Phase of the Ramsey fringes obtained from a least square fit to the Ramsey spectra in Fig. 3.7 (data points). The error of the fit is on the order of the width of the line and therefore not shown. The dashed line is a parabola following the Stark effect expected from calculations, where only the offset is adjusted to the data.

envelope of the spectrum towards smaller detuning. The measured phase is the phase difference of the Ramsey fringes to the center of the envelope function, as can be seen in the fit function (3.3). A shift of the envelope function because of atom losses thereby results in a constant phase shift in the evaluation, which is responsible for the phase shift in zero electric field.
These results show that the phase of the Rydberg atoms can arbitrarily be shifted by the electric field. Together with the coherent excitation process coherent control of the electronic state and phase of the atoms is obtained. Thereby a full coherent control of the internal degrees of freedom of single atoms can be realized on the μs timescale. This is a crucial ingredient for applications like quantum information processing or quantum simulation in ultracold atoms. Even if these applications can, possibly, not be realized in an experiment like this, these experiments show the possibility to coherently control ensembles of atoms between the ground and Rydberg state as a basis for further progress in coherent Rydberg physics.

3.2 Coherence in the presence of strong interactions

Besides the coherent control of the atoms, strong tunable interactions are necessary for most proposed applications of ultracold atoms. These interactions can be induced by Förster resonances in Rydberg systems, as explained in detail in chapter 1.3.3, and will be investigated in the following chapters.
Interactions between the atoms complicate coherent control as even binary interactions can lead to various sources of dephasing that can be understood using the fully co-

herent concept of a pair state interferometer. I show here that the evolution of the atoms remains coherent in the presence of the strong Förster resonance induced interactions, despite these dephasing processes. This internal coherence leads to a measurable interaction-induced phase shift of the Rydberg atoms, which was not measured before.

3.2.1 High resolution spectroscopy of Förster resonances

In order to induce and coherently control interactions between Rydberg atoms in an ensemble of ultracold atoms the Stark tuned Förster resonance

$$44\mathrm{d}_{5/2} + 44\mathrm{d}_{5/2} \rightarrow 46\mathrm{p}_{3/2} + 42\mathrm{f} \tag{3.5}$$

is used, that was presented in chapter 1.3.3. When the energy of these pair states is tuned into resonance, for example by an electric field of about 0.2 V/cm, strong interactions between the atoms arise. The electric field can be seen as a control parameter for the strength of the interactions. Taking a closer look into Figure 3.7 we see a reduced visibility of the Ramsey fringes at about 0.08 V/cm, 0.13 V/cm and 0.21 V/cm that can be attributed to the Förster resonances. This structure in the visibility can be extracted by the fit to the Ramsey spectra, shown in Figure 3.5, that was also used to extract the phase in the previous chapter.
Figure 3.9 shows this fitted visibility of the Ramsey fringes versus the electric field E_z that is obtained from the calibration of the Stark effect (cp. Figure 3.3). Three clearly distinct dips in the visibility can be seen. Also shown are results of the same experiment at different densities of ground state atoms. With decreasing density of ground state atoms, but constant Rabi frequency, the density of Rydberg atoms is reduced. The measurements show that the dips diminish with decreasing densities. For the lowest attainable density of $1 \times 10^{10}\,\mathrm{cm}^{-3}$ the noise level is increased due to the weak ion signal in the spectroscopy. However, none of the dips are visible. The disappearance of the features at low densities is a clear sign for an interaction process. We attribute these features to Förster resonance interactions.
The origin of the loss in visibility in the Ramsey spectroscopy at the Förster resonance is dephasing due to the increased interaction. It will be simulated and explained using the concept of a pair state interferometer in chapter 3.2.3. Here I will only focus on the position of the Förster resonances in the electric field.
In Figure 3.9 the calculated electric fields to tune the pair states into resonance are indicated by diamonds in units of the total electric field $|\vec{E}|$. The measured and calculated resonance positions show a slight mismatch, which can be attributed to an insufficient electric field calibration and to an imprecisely known quantum defect of the Rydberg g states. Due to these error sources an identification of the different resonances in detail is complicated. Information can be obtained by measuring the magnetic field dependence of the resonance positions. The experiment shown in Figure 3.7 was repeated

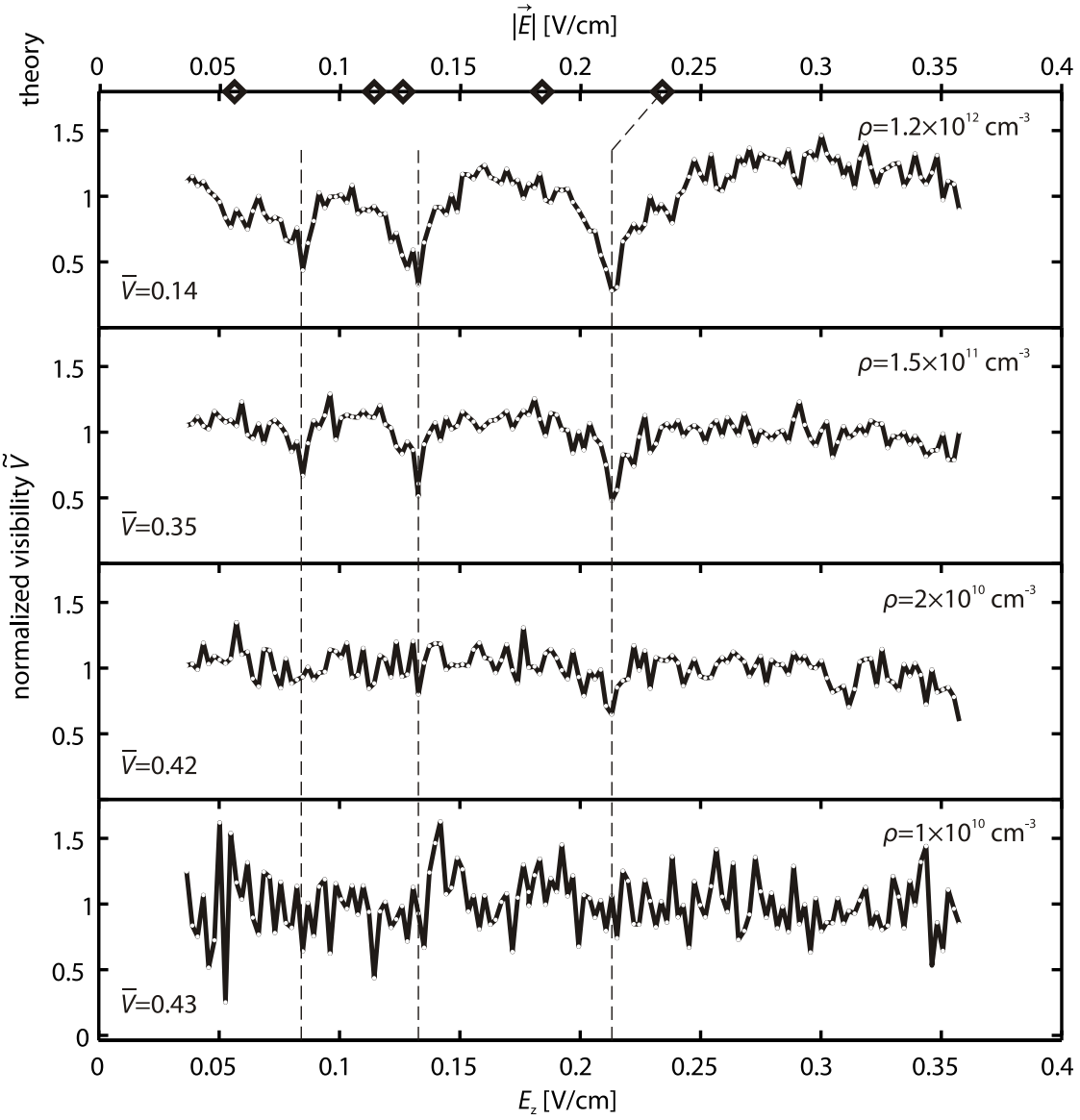

Figure 3.9: The visibility normalized to the mean value $\bar{V}$ of each dataset is plotted versus the electric field for different densities of ground state atoms. The uppermost panel at $\rho = 1.2 \times 10^{12}\,\mathrm{cm}^{-3}$ is the same dataset as in Figure 3.7 and 3.8. The magnetic field is 13.55 G and the Rabi frequency ($\Omega_0 = 100\,\mathrm{kHz}$) is constant for all measurements. The lower electric field axis, valid for all datasets, denotes the calibrated electric field component E_z. The dashed vertical lines denote the Förster resonant fields obtained from the measurements. On the upper electric field axis (total electric field $|\vec{E}|$, including an experimentally noncontrollable radial component) the calculated resonant electric fields are indicated by diamonds.

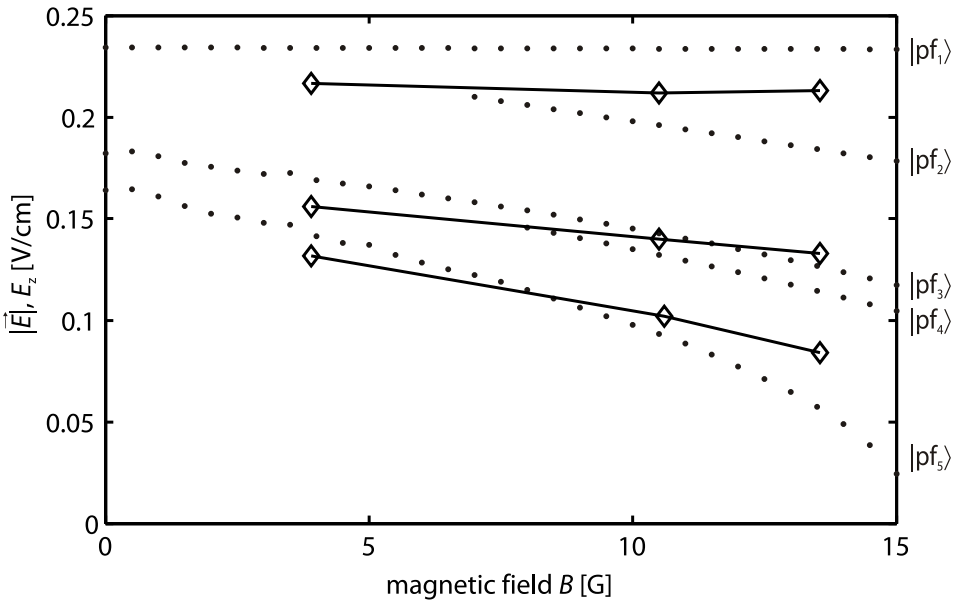

Figure 3.10: Magnetic field dependence of the electric fields where the Förster resonances appear. Dots show the strongest calculated resonances with an angular maximum in the interaction strength of $U_{\max} > 2\pi \times 100\,\mathrm{MHz}\mu\mathrm{m}^3$ (versus the total electric field $|\vec{E}|$) and diamonds show measured values (versus the calibrated electric field E_z).

in different magnetic fields and the electric fields where the dips in the visibility occur were determined. Figure 3.10 shows the calculated electric fields where the strongest resonances appear as a function of the magnetic field and the measured positions of the resonances at 3.9 G, 10.6 G and 13.55 G. The measured resonance at $E_z = 0.21\,\mathrm{V/cm}$ does not show a dependence on the magnetic field and can clearly be assigned to the calculated resonance at $|\vec{E}| = 0.234\,\mathrm{V/cm}$ ($|pf_1\rangle$). The assignment of the other observed resonances is not definitely clear. From the fact that all three resonances are visible at 3.9 G they can probably be attributed to the calculated resonances $|pf_3\rangle$ / $|pf_4\rangle$, that cannot be resolved, and $|pf_5\rangle$.

A radial electric field E_r cannot be included in the calibration as it is not measured in the differential Stark effect. This stray field will increase the strength of the actual electric field relative to the value obtained from the calibration and shift the measured calibrated component of the resonant electric field to smaller values. Figure 3.11 shows the shifts of the electric fields E_z, where the Förster resonances appear, as a function of the radial stray field. The calculations were done as in chapter 1.3.3. At a radial electric offset field of about 0.08 V/cm the best agreement with the measured value for the definitely identified resonance $|pf_1\rangle$ at the strongest electric field is obtained.

However, additionally the electric and magnetic field in the experiment are not parallel and the angle between the radial stray field and the plane of the calibrated electric field and the magnetic field is unknown. A quantitative analysis of this effect seems not

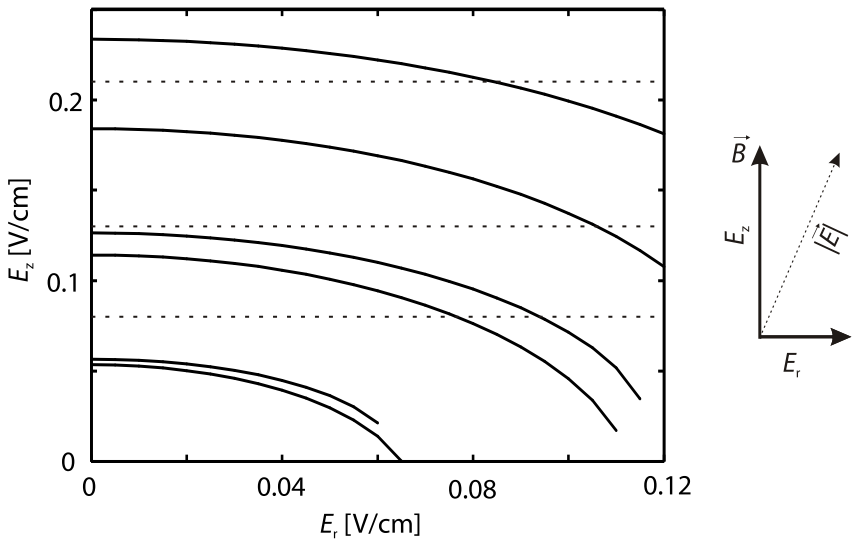

Figure 3.11: Calculated electric fields E_z to tune pair states into Förster resonance as a function of a constant radial electric stray field E_r (solid lines). The dashed lines indicate the calibrated component of the electric field of the measured resonances. The schematic shows the geometry of the calculations.

reasonable as too many unknown parameters contribute.
Furthermore, the position of the calculated resonances is imprecise due to the unknown quantum defect for the relevant 42g state here. The error in the calculations might be as large as 10% (Table 1.4), on the same order as the mismatch to the experiment. Therefore neither a precise calibration of the electric fields in the experiment, nor a determination of the g quantum defect is possible.
However, several resonances can be resolved. From the width of the signal in Figure 3.9 at $E_z = 0.21\,\mathrm{V/cm}$ of $\sim 0.01\,\mathrm{V/cm}$ a resolution of $\sim 5\,\mathrm{MHz}$ in the Förster defect can be calculated from the differential Stark shifts of the pair states (cp. Figure 1.8). This is clearly below the splitting of the resonances and opens the possibility to tune the angular dependence of the interaction, shown in Figure 1.12. In experiments on this Förster resonance so far the resolution was on the same order as the splitting [82]. For another microwave-assisted Stark tuned Förster resonance in ^{85}Rb a considerably better resolution of 0.6 MHz was reported [25].

3.2.2 Measurement of decoherence times of the Ramsey interferometer

At the position of the Förster resonances a reduced visibility is measured as a sign for a loss of coherence in the Ramsey interferometer. The visibility itself is a non-trivial function in the coherence and additionally it is affected by technical issues, mainly the

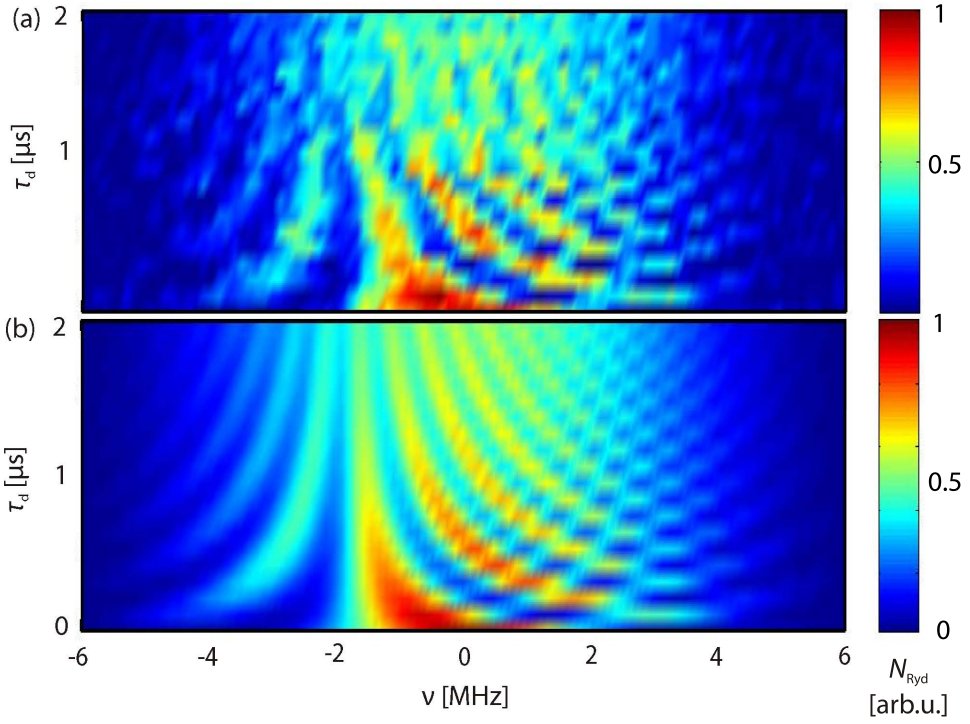

Figure 3.12: Ramsey experiment with variable delay times between $\tau_d = 0\,\mu s$ and $\tau_d = 2\,\mu s$ at an atom density of $1.2 \times 10^{12}\,cm^{-3}$. (a) Color coded, normalized experimental data and (b) data obtained by a numerical fit, both at $E_z = 0.21\,V/cm$.

ion detector and signal amplifier (see Figure 3.6 (a)). It is not suited for a quantitative analysis of the loss of coherence at the Förster resonance. Instead coherence times can describe the coherence in the system, based on the optical Bloch equations (1.9) including phenomenological decay constants.

To obtain the coherence times, Ramsey spectra with varying delay times were measured for pulsed electric fields of strength E_z, using the sequence in Figure 3.5 (b). Every spectrum consists of 401 measurements of the Rydberg atom number N_{Ryd} and is done in one atomic sample. The measurement of these spectra was repeated 21 times with delay times between $\tau_d = 0\,\mu s$ and $2\,\mu s$, where the electric field pulse length always equals the delay time. A typical dataset of 21 spectra at a pulsed electric field of $E_z = 0.21\,V/cm$ is shown in Figure 3.12 (a). With increasing delay time the Ramsey fringe frequency rises, as expected from (1.13). The clear asymmetry stems from the unidirectional Stark effect in the pulsed electric field with varying length. No oscillations in the delay time are visible at a detuning of -1.9 MHz, as this detuning equals the Stark effect at 0.21 V/cm for a polarizability of $85.6\,MHz/(V/cm)^2$ (Table 1.2).

With increasing delay times the visibility of the fringes is reduced as an effect of the loss of coherence. This can be described by the coherence time in terms of the Optical Bloch equations. To obtain this coherence time a numerical solution of the Optical Bloch

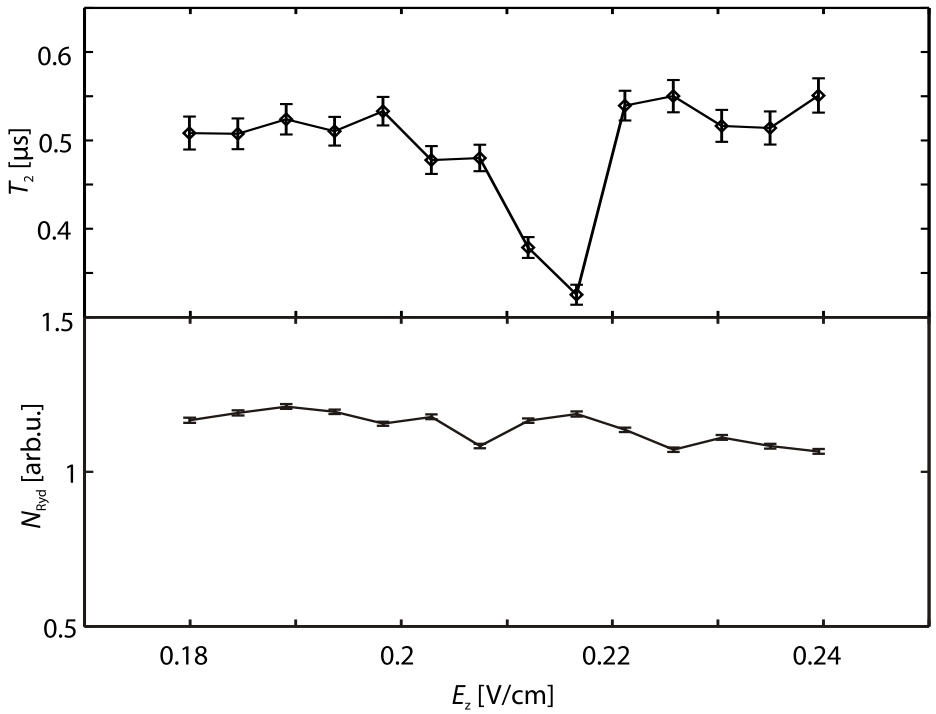

Figure 3.13: Upper panel: coherence time T_2 obtained from numerical fits to datasets at different electric fields E_z. Lower panel: Rydberg atom number in arbitrary units obtained from the fit. The errorbars denote the standard deviation of the fit parameters.

equations (1.9), including the phenomenological decay constants T_1 and T_2, is fitted to the experimental data. The result of such a fit is plotted in Figure 3.12 (b). As the excited state lifetime T_1 is much longer than the duration of each sequence it is fixed to the calculated lifetime of the $44d_{5/2}$ state of $T_1 = 47\,\mu$s [126]. Fits with $T_1 = 100\,\mu$s and $T_2 = 25\,\mu$s show that the results vary only within the standard deviation of the fit. The remaining fit parameters are the coherence time T_2 and a numerical factor N, proportional to the Rydberg atom number.
The measurement of 21 spectra, consisting of 401 data points each, is repeated for 14 different electric fields close to the strongest Förster resonance. The results of fits to these 14 sets of measurements are plotted in Figure 3.13. The Rydberg atom number is almost constant in these experiments. This is expected since the varied electric field during the delay time does not influence the maximal number of excited atoms. The slight variation is because of slow drifts of the performance of the experiment on the time scale of these measurements that take about 30 min per data point.
The coherence time shows a clear dip at 0.214 V/cm, in good agreement with the observation in Figure 3.9. At electric fields detuned from the resonance a constant coherence time of about $0.5\,\mu$s is measured. This corresponds to the linewidth of the excitation to the 44d state of $\Delta\nu = 300\,$kHz (Figure 3.1 (b)), giving a coherence time of

$\tau = \frac{1}{2\pi\Delta\nu} = 0.53\mu$s. Hence, the maximal coherence time is limited by technical constrains on the magnetic and electric field homogeneity and stability as the source of the excitation line broadening and not by interaction effects. The reduced coherence time at the Förster resonance to about $0.32\,\mu$s can clearly be attributed to interaction-induced dephasing processes.
Assuming that the total dephasing rate $\Gamma_{\text{tot}} = 1/0.32\,\mu$s at the resonance is linear in the technical dephasing rate $\Gamma_{\text{tech}} = 1/0.53\,\mu$s and in the interaction-induced dephasing rate Γ_{int}

$$\Gamma_{\text{tot}} = \Gamma_{\text{tech}} + \Gamma_{\text{int}} \tag{3.6}$$

one can calculate an interaction-induced coherence time of $T_2^{\text{int}} = 1/\Gamma_{\text{int}} = 0.7\,\mu$s.
Treating the system at Förster resonance by the two-level optical Bloch equations is a substantial approximation. It totally neglects interactions between the atoms and couplings to other states. In this model, every effect beyond the two-level system is regarded by the coherence time only. Thus, couplings to other states and interactions will contribute to the observed coherence time, even though these couplings may be fully coherent. For a comprehensive understanding of strongly interacting atoms at the Förster resonance pair states have to be considered. An extended model based on pair states will be treated in chapter 3.2.3.
However, the approach of the optical Bloch equations offers to extract quantitative values for the observed loss in coherence, which justifies this evaluation. Based on this quantitative analysis the observed loss of coherence can be compared to other experiments. In [131] a coherence time of $3.6\,\mu$s for single atoms in a dipole trap was measured by Ramsey spectroscopy, but this coherence time was limited by technical constrains on the motional dephasing and magnetic field fluctuations. Damped Rabi oscillations in an ensemble of atoms was measured in [128], but here the coherence time was limited by the laser linewidth. An interaction-dependent damping of oscillations could be observed in [129] in the case of 1-10 atoms with coherence times in the μs regime. Unfortunately no exact values are given.

3.2.3 The concept of a pair state interferometer

In the preceding chapters the electric fields to tune the system into Förster resonance were obtained and a loss of visibility in the Ramsey interferometer at resonance was measured. This loss could be quantified in terms of a coherence time in a two-level single-atom model, but so far no source of this loss of visibility was identified. Especially interesting is the character of the processes that are responsible for the loss of visibility in these experiments, to understand if an ensemble of atoms with induced Förster resonance interactions can be coherently controlled.
At the Förster resonance binary interactions between Rydberg atoms are expected that cannot be included in a single-atom model. Instead atom pair states have to be con-

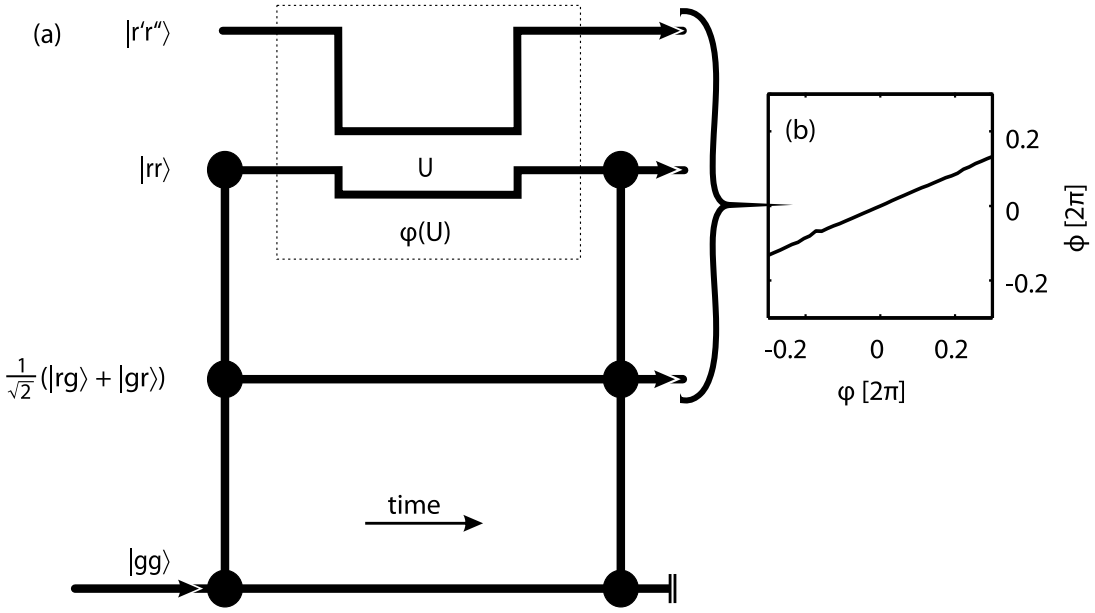

Figure 3.14: (a) Schematic of the pair state interferometer. A pulsed Ramsey field couples the lower three states simultaneously. A Rydberg detector detects the number of Rydberg atoms N_{Ryd}, resulting in a Ramsey spectrum. Interactions between Rydberg atoms couple only the $|rr\rangle$ state to the $|r'r''\rangle$ state, thereby inducing a population transfer to $|r'r''\rangle$ and a phase shift $\varphi(U)$ of $|rr\rangle$ relative to the other states. This phase shift translates to a phase shift ϕ of the Ramsey fringes. (b) shows the transfer function for $0.6\,\pi$-Ramsey pulses describing the dependence of the fitted phase of the Ramsey fringes ϕ on the phase shift φ in the $|rr\rangle$ path for small phase shifts.

sidered, which can describe interactions and couplings to other pair states of atoms as shown in chapter 1.3.2. I will introduce the concept of a pair state Ramsey interferometer in the following, extending the usual two-level atom interferometer (described in chapter 3.1.1 with the excitation light sequence as in Figure 3.5) to two interacting atoms coupled to the optical excitation field. Besides the ground state $|gg\rangle$ and the doubly excited state $|rr\rangle$ there are two singly excited states $|gr\rangle$ and $|rg\rangle$. Only the symmetric combination of the two couples to the Ramsey field. Hence a pair state interferometer consists of three simultaneously interfering paths instead of two in the usual two-level interferometer. Only one of these states, the doubly excited state, experiences strong interactions as it is coupled to other doubly exited states $|r'r''\rangle$.
Figure 3.14 shows a schematic of the relevant pair states for a Ramsey interferometer in an ensemble of atoms with switchable interaction. The system starts in the state where both atoms are in the ground state $|gg\rangle$. Optical light pulses excite single atoms to the Rydberg state and induce couplings between $|gg\rangle$, $\frac{1}{\sqrt{2}}(|gr\rangle + |rg\rangle)$ and $|rr\rangle$. A direct excitation from $|gg\rangle$ to $|rr\rangle$ is suppressed as it is a second order process. Usually a population of $\frac{1}{\sqrt{2}}(|gr\rangle + |rg\rangle)$ after the excitation pulses cannot be omitted. A differ-

ent situation occurs for $\pi/2$ pulses, that transfer the atoms completely to the excited state. The singly excited state is not populated and the system can again be reduced to two interfering paths. In single atom experiments this can indeed be realized, but in an ensemble of atoms, as in the experiments here, $\pi/2$ excitation pulses are not possible because of spatially inhomogeneous Rabi frequencies (chapter 1.3.8). A description based on pair state interferometry with three simultaneously interfering paths is necessary.
Another previously unpopulated Rydberg pair state $|r'r''\rangle$ can be coupled to the $|rr\rangle$ state by a switchable interaction during the delay time between the two Ramsey pulses before the lower three states are coupled again by the optical light field. After this sequence the total number of Rydberg atoms is detected in a Rydberg detector.
This concept of a pair state interferometer is valid for any tunable interaction like induced permanent dipole-dipole interaction or Förster resonances with the control parameters static electric or oscillating fields. The actual form of the interaction is not relevant, but the strength of the interaction determines the response of the interferometer on the interaction. In the case of weak interactions that are slowly turned on the atoms in the state $|rr\rangle$ can adiabatically follow the interaction-induced energy shift. In this adiabatic regime, the atoms remain in the $|rr\rangle$ state but the energy shift accumulates to a phase shift $\varphi(U)$ relative to the interaction independent states $|gg\rangle$ and $\frac{1}{\sqrt{2}}(|gr\rangle + |rg\rangle)$. This phase shift can be calculated from

$$\varphi(U) = \frac{U(r)}{2}\tau_{\mathrm{d}}, \tag{3.7}$$

since the energy shift of the $|rr\rangle$ state is half of the interaction energy $U(r)$. τ_{d} is the time where the interaction is switched on. At the Förster resonance at $|\vec{E}| = 0.234\,\mathrm{V/cm}$, exhibiting a calculated strength of $2\pi \times 1556\,\mathrm{MHz}{\cdot}\mu\mathrm{m}^3$, and at the blockade radius of $6.7\,\mu\mathrm{m}$ at $|\vec{E}| = 0\,\mathrm{V/cm}$ (cp. chapter 1.3.8) the atoms will pick up a phase shift of 2π in about $\tau_{\mathrm{d}} = 0.4\,\mu\mathrm{s}$ if the interaction is switched adiabatically. In the case of strong or spontaneously switched interactions, the atom pair cannot follow adiabatically and a population transfer to $|r'r''\rangle$ appears, usually additional to a phase shift between $|rr\rangle$ and $\frac{1}{\sqrt{2}}(|gr\rangle + |rg\rangle)$.
The probability for a diabatic transition can be calculated from the Landau-Zehner formula [120]

$$p = e^{-\frac{U^2}{\hbar}/\left|\frac{d}{dt}(E_{|pf\rangle} - E_{|dd\rangle})\right|}, \tag{3.8}$$

where U is the coupling strength between the coupled pair states and $E_{|dd\rangle}$, $E_{|pf\rangle}$ are the energies of the pair states. Realistic parameters in the experiments here are a coupling strength of $U = 2\pi \times 1\,\mathrm{MHz}$, a switching time of $T = 20\,\mathrm{ns}$ of the electric fields and a change of energy of $\left|\frac{d}{dt}(E_{|pf\rangle} - E_{|dd\rangle})\right| = 2\pi \times 140\,\mathrm{MHz}/T$ (Figure 1.15). One obtains a probability of $P = 0.994$ for a diabatic passage, almost pure diabaticity.
This pair state interferometer behaves considerably different than a two-path interferometer. For example, even in the case of adiabatically switched interactions and an

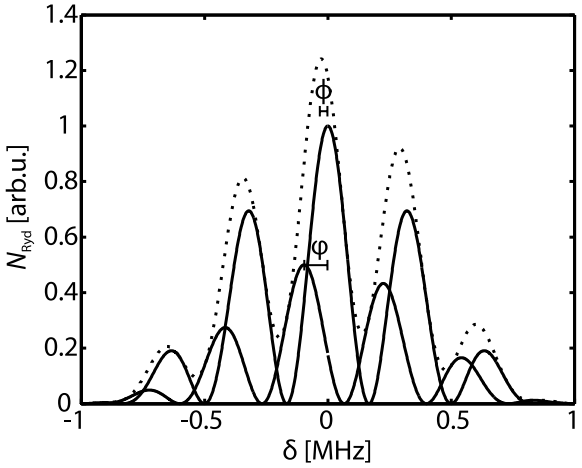

Figure 3.15: The solid lines show Ramsey spectra, phase shifted by φ. If these spectra are summed (dotted line) a reduced visibility occurs and a smaller phase shift ϕ is measured.

individual pair of atoms, a coherent phase shift $\varphi(U)$ in the $|rr\rangle$ path leads to a loss of visibility in the Ramsey spectrum. This can be understood from a simplified Ramsey interferometer, where simultaneously two independent Ramsey spectra are measured, whereof one is phase shifted relative to the other. Figure 3.15 shows two such spectra (solid lines). If the sum of both spectra is measured (dotted line) a reduced visibility is obtained. In the pair state interferometer these two spectra occur as $\frac{1}{\sqrt{2}}(|gr\rangle + |rg\rangle)$ interferes simultaneously with $|gg\rangle$ and $|rr\rangle$. Both interferences generate a Ramsey spectrum, but only one is phase shifted by the interaction. This leads to a reduced visibility depending on the strength of the interaction, even in a fully coherent system.
Compared to Figure 3.15 the actual situation is more involved as both interferences are not independent and interfere the same $\frac{1}{\sqrt{2}}(|gr\rangle + |rg\rangle)$ state. The Ramsey spectrum in the pair state interferometer is a non-trivial function in the populations of the pair states. This population depends on the pulse area of the excitation pulses and is depending on the detuning of the laser. Therefore the Ramsey spectra of the pair state interferometer differ from the model of Figure 3.15. However, the simple picture offers an easy understanding of one origin of the observed loss in visibility.
Furthermore in the pair state interferometer the observed phase shift ϕ is reduced compared to the interaction-induced phase shift $\varphi(U)$ of $|rr\rangle$, also visible from the model in Figure 3.15. Again, the actual pair state interferometer is more involved and the transfer function from the interaction-induced phase shift $\varphi(U)$ to the phase shift of the Ramsey fringes ϕ is a non-trivial function in the experimental parameters.
To gain more insight into the behavior of the interferometer it can be simulated by numerically solving the Schrï£¡dinger equation (1.4) with the Hamiltonian (1.50) for the actual situation in the experiments presented here. The interaction is tuned by Stark shifting the Förster resonance between $|dd\rangle$ and $|pf_1\rangle$. The contributions of other

resonances are omitted for simplicity, reducing the system to only four states $|gg\rangle$, $\frac{1}{\sqrt{2}}(|gd\rangle + |dg\rangle)$, $|dd\rangle$ and $\frac{1}{\sqrt{2}}(|pf_1\rangle + |f_1p\rangle)$ that correspond to the states of the pair state interferometer in Figure 3.14. It can be described by the four dimensional Hamiltonian

$$H = \begin{pmatrix} 0 & \frac{\Omega_{\text{eff}}}{\sqrt{2}} & 0 & 0 \\ \frac{\Omega_{\text{eff}}}{\sqrt{2}} & \delta_L + E_d & \frac{\Omega_{\text{eff}}}{\sqrt{2}} & 0 \\ 0 & \frac{\Omega_{\text{eff}}}{\sqrt{2}} & 2\delta_L + 2E_d & U_1(r,\Theta) \\ 0 & 0 & U_1(r,\Theta) & 2\delta_{\text{L}} + E_{pf_1} \end{pmatrix} \tag{3.9}$$

with the exemplary but realistic parameters $\Omega_{\text{eff}} = 2\pi \times 2\,\text{MHz}$ for the effective Rabi frequency, $U_1 = 2\pi \times 1556\,\text{MHz}{\cdot}\mu\text{m}$ for the interaction strength and the interatomic distance $r = 5\,\mu\text{m}$. δ_L is the detuning of the exciting laser relative to the atomic resonance, E_d the Stark effect of the 44d state and E_{pf_1} the Stark shift of the $|pf_1\rangle$ pair state.

Figure 3.16 shows the time evolution of the populations in the four pair states for a typical pulse sequence like in Figure 3.5. During the optical excitation pulse (shaded area) a population of $\frac{1}{\sqrt{2}}(|gd\rangle + |dg\rangle)$ and of $|dd\rangle$ is created. In between the optical Ramsey pulses, when the system is tuned close to the Förster resonance by an applied electric field, population oscillates between the $|dd\rangle$ and the $\frac{1}{\sqrt{2}}(|pf_1\rangle + |f_1p\rangle)$ state. In the simulation the fields are switched spontaneously, hence this population transfer occurs for all interaction strengths. This is a good approximation of the almost pure diabatic switching of the field in the experiment. When the second Ramsey field pulse is applied, the electric field is tuned to zero. A remaining coherence between $|dd\rangle$ and $\frac{1}{\sqrt{2}}(|pf_1\rangle + |f_1p\rangle)$ still leads to small oscillations with the Förster defect $\Delta = 63\,\text{MHz}$ at zero electric field, but dominantly the lower three pair states are interfered again.

The Rydberg atom detection in the experiments presented in this work is not state selective and only the total number of Rydberg atoms can be measured. To simulate these experiments the (normalized) number of Rydberg atoms N_{Ryd} is obtained by summing the populations p_i of the four states at the end of the sequence, as shown in Figure 3.16, as $N_{\text{Ryd}} = p_{|gd\rangle} + 2p_{|dd\rangle} + 2p_{|pf_1\rangle}$. The full simulated spectrum consists of simulations for 201 detunings δ_L between -6 MHz and +6 MHz. This Ramsey spectrum in frequency space can be fitted using equation (3.3) as in the experiment to obtain the visibility and the phase ϕ of the Ramsey fringes.

This phase differs from the interaction-induced phase shift φ of the $|dd\rangle$ state as described previously in terms of the transfer function. To obtain this transfer function no interaction ($U_1 = 0\,\text{MHz}{\cdot}\mu\text{m}^3$) but a fixed phase shift $e^{-i\frac{\varphi}{2\pi}}$ of the $|dd\rangle$ state between the two Ramsey pulses was included. Figure 3.14 shows the simulated transfer function in the case of 0.6π Ramsey pulses. For small interaction-induced phase shifts $\varphi(U)$ the transfer function is a monotonic function in $\varphi(U)$. Close to $\varphi(U) = \pi$ the Ramsey fringe pattern is strongly disturbed so that the fit function (3.3) is not a good approximation

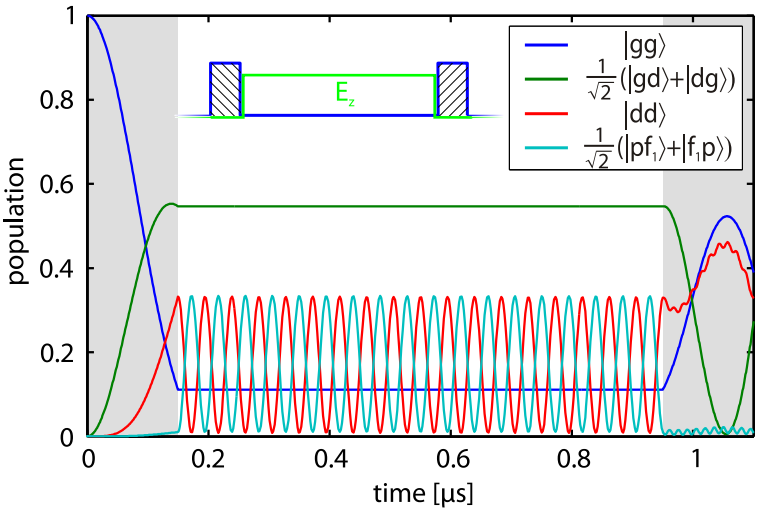

Figure 3.16: Evolution of the populations in the pair states of the interferometer for the pulse sequence in the inset using experimentally realistic parameters for the Förster resonance at the highest electric field. The shaded areas indicate the time of the excitation pulses.

of the simulated spectrum and the phase is not well defined. The actual dependence of ϕ on $\varphi(U)$ is depending on the pulse area of the Ramsey pulses. However, under any circumstances the effective phase shift ϕ is smaller than the phase shift of the doubly excited state $\varphi(U)$.
This totally coherent model of a pair state interferometer is used to simulate the experiments in the following chapters, using different electric field pulse sequences. However, in an ensemble of atoms with strong binary interactions the ensemble average over different interaction strength $U(\Theta, r)$ due to the distance and angular dependence of the interaction even at constant density results in an additional dephasing. This can be attributed for if the angular dependence and different interatomic distances are averaged. Irrespective of the situation exactly on Förster resonance, the interaction is predominantly of van der Waals type, with scales as r^{-6} with the interatomic distance. This features a short range interaction which effect can be described in good approximation by calculating the next neighbor contribution. The dephasing due to the different interaction strengths can hence be simulated by averaging over the next neighbor distribution, which is given by the Chandrasekhar distribution [87, 135]

$$P(r) = e^{-r^3/r_0^3} 3r^2/r_0^3 \tag{3.10}$$

in the case of a random distribution of particles with average distance r_0.
The angular dependence of the interaction is averaged out in an extended ensemble considerably larger than the next neighbor distance between Rydberg atoms. As the van der Waals interaction (1.49) is calculated from $|\langle k''k'| V_{\mathrm{dd}}(\Theta, r) |kk\rangle|^2$, the quadratic

mean of the angular dependence of the dipole-dipole interaction between two states

$$\bar{U}(r) = \sqrt{\frac{1}{\pi}\int_0^\pi \left(U_{\mathrm{dd}}(\Theta, r)\right)^2 \mathrm{d}\Theta} \tag{3.11}$$

is calculated and included in the simulations of the pair state interferometer.
This ensemble averaging is a necessary simplification of the system to describe it in the two-atom picture, but limits the accuracy of the simulations. Moreover, an inhomogeneous density distribution will lead to yet another source of dephasing, especially because of inhomogeneous collective Rabi frequencies. Furthermore in the experiment decoherence due to a finite excitation linewidth is present. These dephasing mechanisms are not included in the concept of the pair state interferometer and have to be considered if the simulations are compared to actual experiments.
The pair state interferometer simplifies the experiments in many other ways. Besides the ensemble averaging for the angular dependence and the inhomogeneous atom distribution only binary interactions are calculated and the many-body nature of the experiment is considered solely by a collective enhancement of the Rabi frequency. Direct three- or four-body interactions are only expected when respective many-body states become resonant [136]. But even in absence of direct many-body interaction higher order terms in the interaction can play profound roles [137] and additional dynamics can arise in a many-body system even with pure binary interactions [22, 28]. These additional processes can enhance and broaden the interaction effects and should be kept in mind to evaluate the results correctly. However, the considered binary interactions still play the dominant role and the concept of a pair state interferometer describes the fundamental characteristics of the experiments here.

3.2.4 Coherent evolution of pair states

Dephasing mechanisms lead to a loss of coherence in single-pulse experiments. Here, this dephasing appears for example between pair states because of inhomogeneous interaction strengths in the atomic ensemble. Some of the inhomogeneous dephasing mechanisms can be refocused by using Ramsey type pulse sequences for the interaction strength. That means that the interaction strength has to be pulsed like in a Ramsey sequence to refocus the dephased pair state system into the initial state. Thereby Ramsey experiments are not sensitive to inhomogeneous coupling strengths of the Ramsey pulses, which enable to directly observe the coherent evolution of the ensemble even in the presence of inhomogeneous interaction strengths.
The interaction strength can be tuned by the electric field and a Ramsey type pulse sequence in the interaction strength can be realized by the pulsed electric field sequence from Figure 3.17 (a). The electric field is first pulsed for $t_{\mathrm{res}} = 200\,\mathrm{ns}$ to the electric field E_{res} with a rise time of 20 ns to tune the pair states into Förster resonance. After

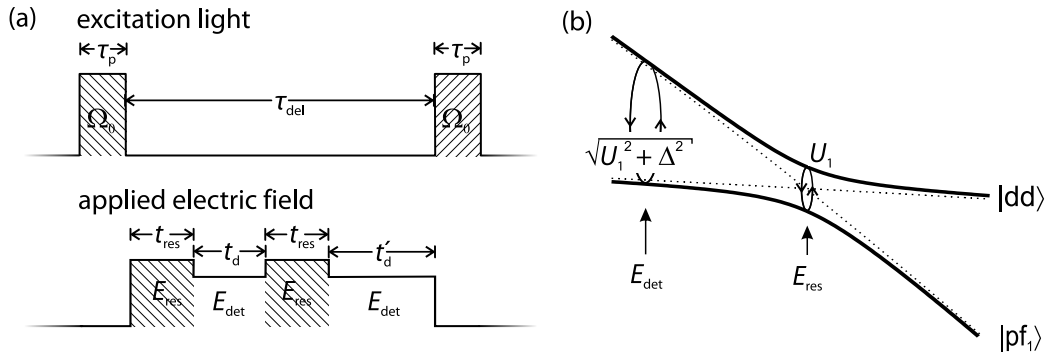

Figure 3.17: (a) Pulse sequence of the double Ramsey experiment. (b) Relevant avoided crossing between the $|dd\rangle$ and the $|pf_1\rangle$ state with the coupling strength U_1. The resonant electric field E_{res} and a detuned electric field E_{det} are indicated and the respective energy differences are specified.

a variable delay time t_{d} between 0 ns and 400 ns a second 200 ns pulse at E_{res} is applied. Between and after these two Ramsey-like pulses the electric field is detuned from exact resonance to a variable value E_{det} (t_{d} and t'_{d}). The total length of this electric field pulse train matches the delay time of $\tau_{\mathrm{del}} = 800\,\mathrm{ns}$ between the 150 ns optical Ramsey pulses. The single atom Rabi frequency is about $\Omega_0 = 2\pi \times 25\,\mathrm{kHz}$ and the peak ground state atom density is $2 \times 10^{12}\,\mathrm{cm}^{-3}$. Using this double Ramsey sequence 401 times with laser detunings ranging from -6 MHz to +6 MHz Ramsey spectra were taken for different delay times t_{d} and different electric fields E_{det}. From a fit of (3.3) to every Ramsey spectrum the visibility and phase can be obtained.
This particular sequence offers the advantage that the total time at the resonant electric field ($2 \times t_{\mathrm{d}}$) and at the detuned field ($t_{\mathrm{d}} + t'_{\mathrm{d}}$) are constant throughout one measurement. Additional losses of coherence, e.g. dephasing due to inhomogeneous atom distributions or due to a finite laser linewidth, reduce the visibility to a constant value throughout one measurement. Oscillations in the visibility when varying the delay time between the resonant pulses can clearly be separated. This is, for example, not the case for the pulse sequence in Figure 3.19, that will be discussed later.
In the experiment the Förster resonance at the highest electric field of $E_{\mathrm{res}} = 0.213\,\mathrm{V/cm}$, obtained from Figure 3.9, is used. The avoided crossing between the relevant pair states is shown in Figure 3.17 (b) together with the electric fields E_{res} and E_{det}. This resonance is used as it can clearly be attributed to the calculations and it shows the strongest interaction. Measurements were done at detuned electric fields between 0.181 V/cm and 0.241 V/cm. Figure 3.18 (a) shows the fitted visibility for some of these measurements versus the delay time t_{d} between the resonant electric field pulses. Clear oscillations in the visibility can be seen, that show no damping on the timescale of the experiments. The observed oscillations directly proof the coherent coupling between Rydberg pair

states, similar to the observation of [28]. The oscillation frequency is smaller the closer the detuned electric field E_{det} is to the resonant field E_{res}. From sinusoidal fits to the visibility, which are shown in Figure 3.18 (a) as well, the frequency of the oscillations is obtained.
The Förster defect at the detuned electric field E_{det} can be calculated from the differential Stark shift of the pair states, as shown in Figure 3.17. Here, the slight deviation of the calculated electric field to tune the pair states into Förster resonance to the measurements can be compensated by a constant offset field of 0.018 V/cm. This linear approximation is reasonable for the resonance used here, since the calibrated electric field is bigger than the expected radial stray field $E_z \gg E_r$ and only measurements at electric fields close to the Förster resonance are performed.
Figure 3.18 (b) shows the fitted oscillation frequency of the measurements versus the Förster defect. The measured oscillation frequency follows the Förster defect Δ and shows a minimum at the position of the resonance. Close to the resonance the amplitude of the oscillations (Figure 3.18 (c)) is strongly reduced and no oscillation frequency could be measured.
This experiment can be regarded as a Ramsey-like experiment between the $|dd\rangle$ and the $|pf\rangle$ states only. The first resonant electric field pulse resonantly couples the $|dd\rangle$ state to the $|pf\rangle$ state, generating a coherence between these states. During the delay time t_{d} the electric field is detuned from exact resonance. In contrast to usual Ramsey experiments the two states are still coupled and the atom pairs will oscillate between $|dd\rangle$ and $|pf\rangle$ with the oscillation frequency $\nu(\Delta) = \sqrt{U_1^2 + \Delta^2}$. The second resonant electric field pulse interferes both pair states again. The maximum visibility in the Ramsey spectrum occurs at an electric field E_{det} where after the delay time t_{d} and the second resonant electric field pulse the atom pairs are refocused into the $|dd\rangle$ state. The oscillations between the pair states are now visible as oscillations in the visibility when the delay time t_{d} is varied.
From this interpretation of the experiment one expects that the oscillation frequency equals the Förster defect Δ for $\Delta \gg U_1$, as observed in Figure 3.18 (b). Close to the resonance, however, a deviation of this linear behavior is expected following $\nu(\Delta) = \sqrt{U_1^2 + \Delta^2}$. In the experiment this is not observed for Förster defects of $|\Delta| \gtrsim 2\,\mathrm{MHz}$. Closer to the resonance ($|\Delta| \lesssim 2\,\mathrm{MHz}$ corresponds to $E_z \approx 0.209 \ldots 0.217\,\mathrm{V/cm}$) no oscillations could be measured. This can be understood as follows: Strong dephasing occurs when the system is dominated by the interaction between the pair states ($\Delta \lesssim U_1$), as this interaction forms a broad band due to the dependence on the interatomic distance. However, the coupling between single pair states is coherent on the timescale of the experiment. This coherence leads to the observed oscillations in the interferometer if the time evolution is dominated by the spatially constant Förster defect.
The smallest measured oscillation frequency is about 2 MHz, giving an upper limit for the average interaction strength. At the Förster resonance used here, with an angular

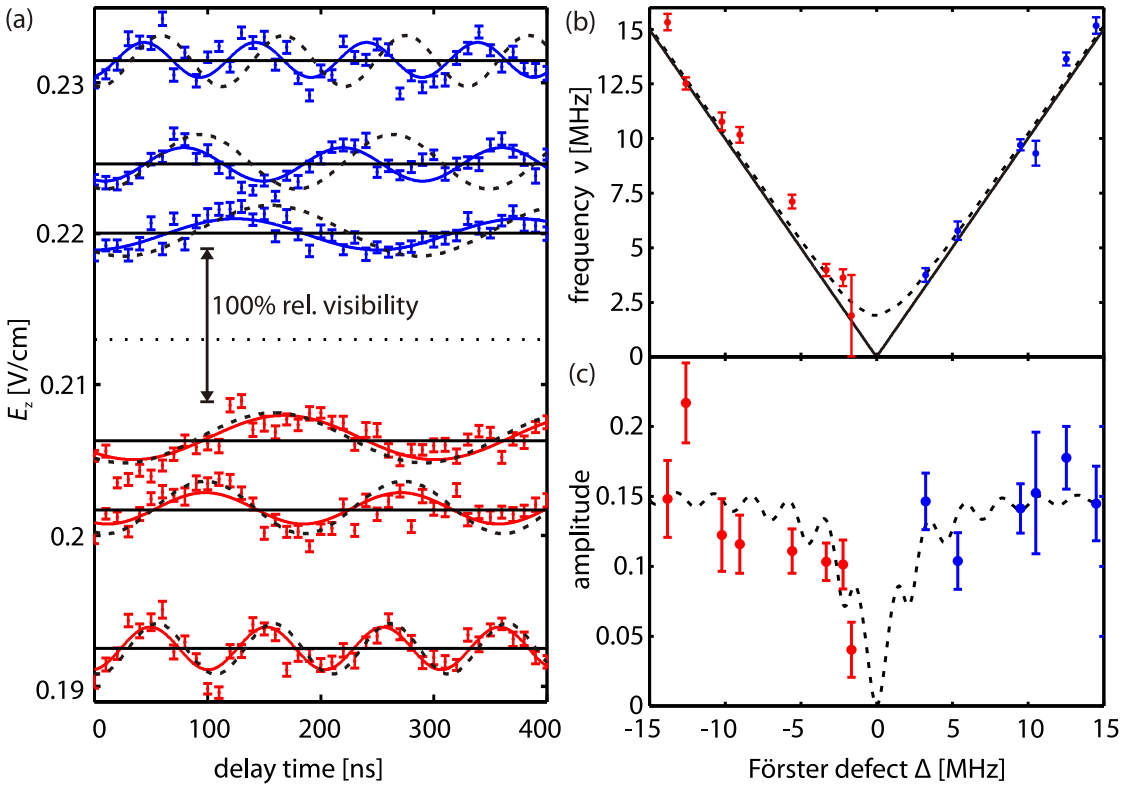

Figure 3.18: (a) Oscillations in the visibility are measured in the double Ramsey pulse sequence. The electric field during the delay time E_{det} is indicated by the solid black lines. The oscillations in the visibility (data points with error bars resulting from the standard deviation of the fit to the Ramsey spectrum) are normalized and centered on the applied electric field. The solid lines are sinusoidal fits to the data. The dashed lines are simulations of the experiment. The dotted horizontal line indicates the electric field to tune the pair states into Förster resonance. (b,c) Measured (data points with errorbars obtained from fit) and simulated (dashed line) dependence of the frequency and the amplitude of the oscillations in the visibility on the Förster defect. The solid line in (b) shows $\nu = |\Delta|$. The Blue (red) data indicate positive (negative) Förster defects.

averaged interaction strength of $2\pi \times 719\,\mathrm{MHz}{\cdot}\mu\mathrm{m}^3$, interaction strength of about 2 MHz are expected at interatomic distances between Rydberg atoms of 7 μm. This estimate gives a lower limit on the interatomic distance. It matches the blockade radius of 6.7 μm (chapter 1.3.8) during the Rydberg excitation at $E_z = 0$. In the experiment the system is not driven into the saturated Rydberg density and bigger interatomic distances are expected, in perfect accordance to the estimate of the lower limit on the distance.
Using the concept of the pair state interferometer from chapter 3.2.3 and the experimental pulse sequence (Figure 3.17 (a)) the results of this experiment can be simulated by numerically solving the Hamiltonian (3.9). As these experiments are very close to a single Förster resonance the dynamics are dominated by a single resonance and can be described by four pair states $|gg\rangle$, $\frac{1}{\sqrt{2}}(|gd\rangle + |dg\rangle)$, $|dd\rangle$ and $\frac{1}{\sqrt{2}}(|pf_1\rangle + |f_1p\rangle)$. To estimate the collective Rabi frequency $\Omega_{\mathrm{eff}} = \sqrt{N_{\mathrm{B}}}\Omega_0$ the number of Rydberg atoms per blockade sphere N_{B} has to be calculated. The blockade radius during the excitation at $E_z = 0$ is 6.7 μm (chapter 1.3.8). At a density of $\rho = 2 \times 10^{12}\,\mathrm{cm}^{-3}$ this corresponds to $N_{\mathrm{B}} = 2600$ and a 50-times enhancement of the Rabi frequency to $\Omega_{\mathrm{eff}} = 2\pi \times 1.27\,\mathrm{MHz}$. In the simulations a collective Rabi frequency of $\Omega_{\mathrm{eff}} = 2\pi \times 1\,\mathrm{MHz}$ is used, close to the estimated value. Test simulations with higher Rabi frequencies showed similar results that only slightly varied in the amplitude of the oscillations. The interatomic distance is fixed to 9 μm, reasonably bigger than the estimated lower limit of the interatomic distance of about 7 μm.
The simulated visibility is shown as dashed black lines in Figure 3.18 and agrees remarkably well with the measurements. The dependence of the simulated oscillation frequency on the Förster defect perfectly matches the expected $\sqrt{U_1^2 + \Delta^2}$ behavior. It shows the expected linear increase with the Förster defect for $|\Delta| \gg U_1$ and the deviation from the linear $\nu = |\Delta|$ behavior at small Förster defects. Figure 3.18 (c) displays the simulated and observed amplitude of the oscillation in the visibility. The amplitude features a pronounced dip at the resonance and a periodic variation of the amplitude with the Förster defect. This oscillation cannot be resolved in the experiment. The interaction strength might be measureable in the regime, where the interaction strength is at least on the same order as the Förster defect. This appears at Förster defects, where the oscillation frequency shows the deviation from the linear behavior in Figure 3.18 (b). Unfortunately this is the same regime where also the dip in the amplitude occurs. No experimental results could be obtained in this regime.
The amplitude is in perfect agreement to the measurements. The agreement in the amplitude might come as some surprise as the total value of the visibility is strongly affected by technical reasons, e.g. the excitation linewidth, that is not included in the simulations. However, the Ramsey-like sequence in the interaction strength is independent of the initial phase of the $|dd\rangle$ pair state after the excitation pulse. Thereby the observed oscillations are independent from the laser-induced dephasing that only reduces the overall visibility in the experiment. This explains the agreement in the amplitude

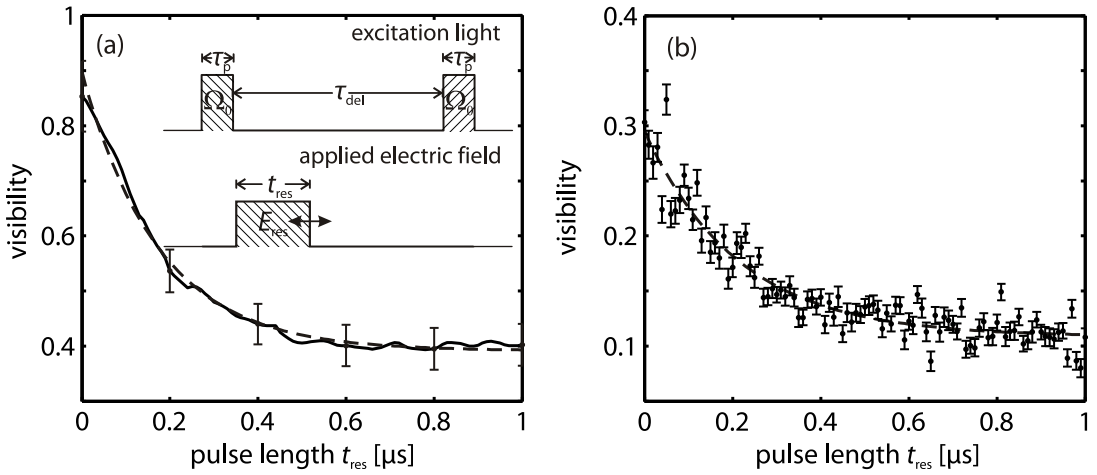

Figure 3.19: Simulated (a) and measured (b) visibility versus the length of the single electric field pulse t_{res}. The errorbars denote the standard deviation of the fit to the Ramsey spectrum. The dashed lines are results of fits to the simulated and experimental data. The inset in (a) shows the pulse sequence for this experiment.

of the oscillations in contrast to the absolute visibility.
In these simulations no averaging over the density distribution of the Rydberg atoms was done, as suggested in connection with equation (3.10). Test calculations averaging over several interatomic distances between $2\,\mu$m and $25\,\mu$m, weighted by the next neighbor distribution (3.10) with an average interatomic distance $r_0 = 9\,\mu$m, did not show a strong influence for $|\Delta| > 2\,$MHz. This can be understood as for $|\Delta| > 2\,$MHz the evolution is dominated by the Förster defect and not the interaction strength. The computationally expensive averaging was omitted here.
In the experimental sequence used so far the evolution exactly on resonance, where the system is completely dominated by the interaction strength, cannot be studied. For $E_{\mathrm{det}} \to E_{\mathrm{res}}$ the sequence consists of one single electric field pulse and does not depend on the delay time. However, in principle direct Rabi oscillations could be measured using a single resonant electric field pulse $E_{\mathrm{res}} = 0.213\,$V/cm with variable length, as shown in Figure 3.19. For this experiment the delay time between the 150 ns optical Ramsey pulses was chosen to be 1000 ns and the length of the electric field pulse was varied between $t_{\mathrm{res}} = 0\,$ns and $t_{\mathrm{res}} = 1000\,$ns in 101 steps. The results of this measurement are shown in Figure 3.19 (b). Instead of Rabi oscillations only an exponential decay of the visibility occurs with a time constant of 213 ns. This can be explained by dephasing due to the inhomogeneous interaction strength, as predicted in [135] based on Monte Carlo calculations for an ensemble of atoms. The measured time constant agrees rather well with the obtained total coherence time of 320 ns from chapter 3.2.2.
To simulate this experiment the next neighbor distribution of Rydberg atoms has to be accounted for, as this distribution dominates the observed dephasing. The experimental

sequence is simulated for 93 interatomic distances between 2 μm and 25 μm and the Ramsey spectra are weighted and averaged according to a Chandrasekhar distribution (3.10) with an average interatomic distance of $r_0 = 9\,\mu$m. These averaged spectra are fitted as in the experiment. The result of these simulations is shown in Figure 3.19 (a) and shows an exponential decay as well. The small oscillations are due to the finite number of averaged distances.
The overall visibility is higher by a factor of three to four in the simulations compare to the measurements. This might be explained by additional dephasing due to the finite linewidth of the excitation. It was measured to be 300 kHz for the 44d state in the high magnetic offset field. This corresponds to a coherence time of 0.53 μs and reduces the visibility on the 1 μs time scale of the experiment, that was also shown in the measurements of the coherence time T_2 in chapter 3.2.2. This effect is not included in the simulations.
An exponential fit to the simulation results in a time constant of 175 ns, in pretty good agreement to the experimental value given that the used model simplifies the system in many ways. For example, exactly on resonance the atoms experience a $1/r^3$ long-range interaction. Calculating solely the next neighbor contribution, as done in the simulations, is not sufficient. Instead the contributions of all atoms have to be taken into account, effectively reducing the width of the band of interaction strength. This might result in a lower dephasing in the experiment. Furthermore the angular averaging of the interaction strength is valid for van der Waals interaction but not for resonant dipole-dipole interaction. There the angular average would result in zero interaction for a spherical sample and possibly reducing the interaction and with it the dephasing in the cigar shaped system here.
However, the simulations reproduce the fundamental characteristics of the many-body system excellent and demonstrate the validity of the presented physical picture of a pair state interferometer to describe the fully coherent evolution of the ensemble of strongly interacting Rydberg atoms. This coherent evolution is remarkable as there is no real experimental control over the interatomic spacings, strongly affecting the interaction strength and generating dephasing. These experiments show the coherence of the coupling between pair states in Rydberg systems and are a significant step towards coherent many-body control.

3.2.5 Interaction-induced phase shifts in a pair state interferometer

In chapter 3.2.1 a reduced visibility at Förster resonance was measured, that was qualitatively explained in terms of the pair state interferometer in chapter 3.2.3. The double Ramsey experiments in chapter 3.2.4 showed that, despite the dephasing within the interferometer, a coherent evolution of atom pairs occurs. This is an essential prerequisite for an interaction-induced phase shift, as necessary for a proposed quantum phase

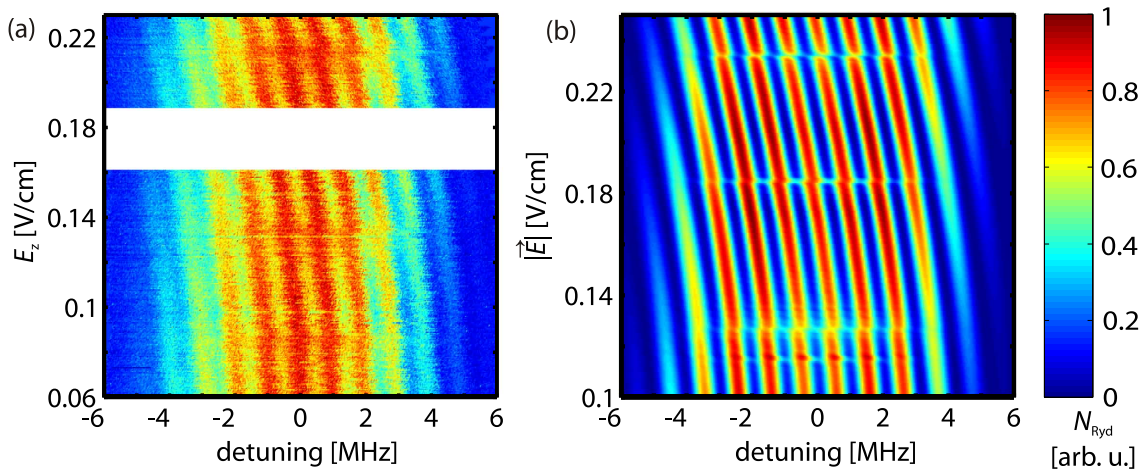

Figure 3.20: Measured (a) and simulated (b) color coded Ramsey spectra versus the electric field. A loss of visibility and a dispersive phase shift at the Förster resonances is visible in both data sets.

gate [40, 39]. The concept of the pair state interferometer predicts the occurrence of this interaction-induced phase shift and the possibility to observe the phase shift in the Ramsey interferometer close to a Förster resonance (cp. Figure 3.14).
Here I will show experiments using the same pulse sequence with only slightly optimized timing as in chapter 3.2.1 to measure this Förster interaction-induced phase shift and I will present simulations reproducing the experimental findings. To the best of our knowledge this phase shift was not observed before.
In these experiments a single electric field pulse of $\tau_{\mathrm{del}} = 800\,\mathrm{ns}$ was applied between two $\tau_{\mathrm{p}} = 150\,\mathrm{ns}$ optical Ramsey pulses (see Figure 3.5). Compared to the measurements in chapter 3.2.1 the timing was optimized to a slightly shorter sequence and a smaller single atom Rabi frequency of $\Omega_0 = 2\pi \times 25\,\mathrm{kHz}$ was used. This enhances the coherence and enables the observation of the interaction-induced phase shift. 401 Ramsey pulse sequences followed by field ionization and ion detection were used in series on the same atomic sample to measure one Ramsey spectrum. These measurements were performed for 322 pulsed electric fields between $E_z = 0.060\,\mathrm{V/cm}$ and $0.161\,\mathrm{V/cm}$ as well as between $0.188\,\mathrm{V/cm}$ and $0.234\,\mathrm{V/cm}$. The range between $0.161\,\mathrm{V/cm}$ and $0.188\,\mathrm{V/cm}$ was excluded to reduce the experimental effort as there no Förster resonances are observed (see Figure 3.7).
Figure 3.20 shows the color coded Ramsey spectra versus the pulsed electric field. Again, a loss of visibility at the Förster resonances at $0.084\,\mathrm{V/cm}$, $0.132\,\mathrm{V/cm}$ and $0.213\,\mathrm{V/cm}$ occurs. Despite this loss, a small deviation in the quadratic phase shift around the Förster resonances is visible, indicating a coherent interaction between the Rydberg atoms.
The experiment is numerically simulated by the full seven dimensional Hamiltonian

(1.50), taking all Förster resonances into account. This is necessary as the electric field is scanned over all resonances in this experiment. The spectra were averaged and weighted by the next neighbor distribution (3.10) to damp oscillations in the resonant energy transfer, as expected in an ensemble of atoms. The best results were obtained from simulations with a collective Rabi frequency of $\Omega_{\text{eff}} = 2\pi \times 2\,\text{MHz}$, slightly bigger than the estimated collective Rabi frequency of $2\pi \times 1.27\,\text{MHz}$ at the experimental peak density of $2 \times 10^{12}\,\text{cm}^{-3}$, and an average Rydberg atom distance of $r_0 = 9\,\mu\text{m}$, reasonably exceeding the blockade radius of $6.7\,\mu\text{m}$ during the excitation. The simulated Ramsey spectra are shown in Figure 3.20 as well. The experimental data and the simulations seem not to agree at the first glance. The overall visibility in the simulations is considerably higher and fools the eye. A more quantitative analysis of these data is necessary. However, despite this mismatch in visibility a phase shift at the Förster resonances, as predicted from the pair state interferometer model and as observed in the measurements, is reproduced.

The more quantitative analysis of the experiment and of the simulations is done by fitting every Ramsey spectrum with the function (3.3). The visibility V and phase ϕ of the Ramsey fringes are plotted in Figure 3.21. A comparison of the measured and simulated visibility show very similar losses of visibility at the resonances, but also clear differences. Apart from the absolute positions of the Förster resonances in the electric field, that are discussed in chapter 3.2.1, the measured visibility is about a factor of four smaller than in the simulations. This can be explained by the dephasing due to the finite excitation linewidth that is not included in the simulations. Furthermore the measured dips are broader, possibly also because of additional dephasing processes beyond the pair state model, e.g. resonant energy transfer in many-body systems [28]. However, quantitatively the observed visibility at the Förster resonance can be reproduced with the two-body calculations.

The phase is not expected to be substantially disturbed by an additional loss of coherence. The middle panel in Figure 3.21 shows the expected quadratic dependence on the applied electric field in the measurements and the simulations because of the quadratic Stark effect (1.28). To observe a deviation from this single-atom effect the quadratic dependence was fitted and subtracted from the data. The difference is shown in the lower panels in Figure 3.21. The measured data clearly features a dispersive shape of the phase of the Ramsey fringes in the electric field centered around the resonant electric fields where the Förster resonances occur. This dependence is perfectly reproduced by the simulation even in the amplitude of the phase shift.

The interaction-induced phase signal not only directly verifies the coherence of the interaction but also contains information about the character of the interaction. The sign of the phase shift is determined by the direction of the interaction energy shift of $|dd\rangle$, hence depending on the direction of the interaction. In the limit of van der Waals interaction it depends on $1/\Delta$. This changes sign at the resonance position from attractive

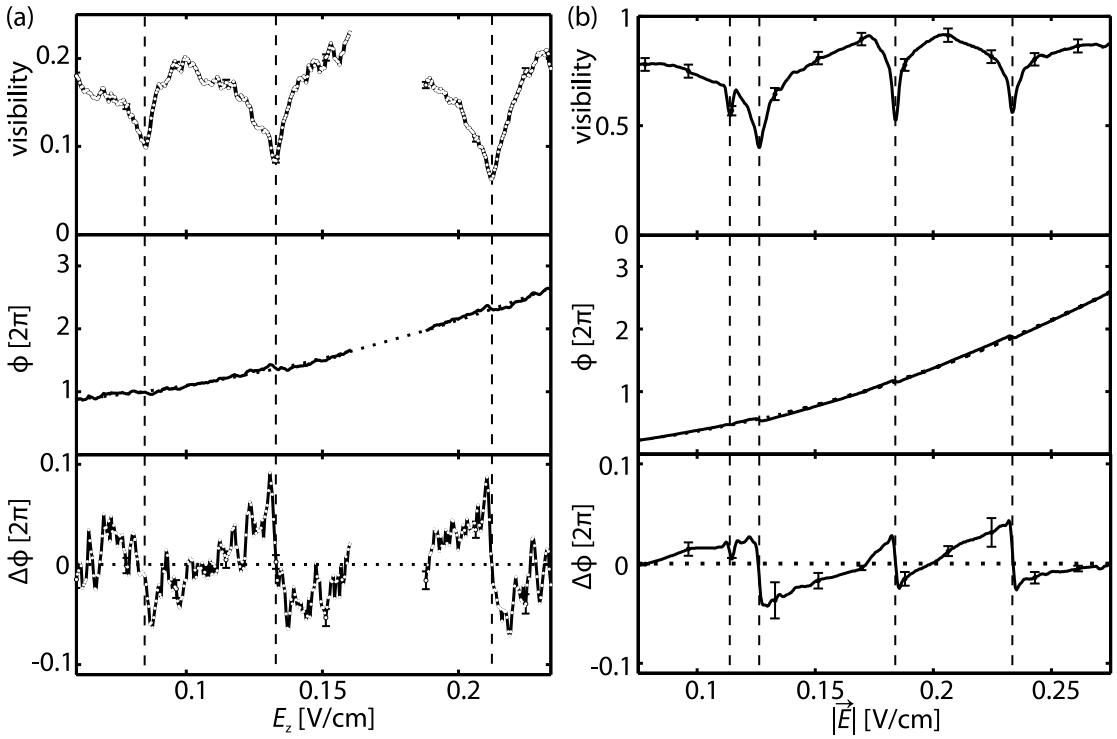

Figure 3.21: Visibility and phase obtained from fits to the measured (a) and simulated (b) Ramsey spectra versus the electric field. Note that the experimental spectra are plotted versus the calibrated component of the electric field E_z and the simulated data versus the total electric field $|\vec{E}|$. The uppermost panels show the visibility, the middle panels show the phase of the Ramsey fringes (solid line) and a quadratic fit to the data (dotted line) and the lower panels show the difference of the measured phase from the pure quadratic behavior. Some example error bars are plotted, denoting the standard deviation of the fit parameter. The vertical dashed lines indicate the positions of the resonances.

at electric fields smaller than the resonant field E_{res} to repulsive interaction above the resonance, leading to the dispersive phase signal. The dispersive signal also shows that the interaction is stronger for smaller Förster defects close to the resonance. Exactly on resonance two equally spaced states in the avoided crossing (see Figure 3.17) above and below the unperturbed states appear. Under these conditions the system is diabatically switched from the unperturbed $|dd\rangle$ state at $E = 0\,\mathrm{V/cm}$ to the perturbed states at E_{res}, generating a superposition state that does not experience interactions and no phase shift occurs.

For a first rough estimate of the amplitude of the phase shift (3.7) at an interaction strength of $2\pi \times 1\,\mathrm{MHz}$ between two Rydberg atoms and an interaction time of $0.8\,\mu\mathrm{s}$ one would expect a phase shift of the pair state of $\varphi = 0.8\pi$. The transfer function of the pair state interferometer (Figure 3.14) lowers the observed shift ϕ. This estimate agrees reasonably well with the observed shift.

Complete simulations of the pair state interferometer exhibit the same dependence of the phase on the electric field and even agree in amplitude of the phase shift (Figure 3.21 (b)). This is remarkable as the pair state model is a considerable simplification of the experimental situation, especially the assumed constant Rabi frequency and density. In a trapped cloud the ground state density is inhomogeneous and will alter the next neighbor distribution and the collective Rabi frequency. This clearly influences the populations of the coupled $|dd\rangle$ and $|pf\rangle$ states as well as the population of the $\frac{1}{\sqrt{2}}(|gd\rangle + |dg\rangle)$ state, that is interfered with $|dd\rangle$ by the light field. The measured phase of the Ramsey fringes is a non-trivial function in these populations, expressed by the transfer function, and hence strongly influenced by this inhomogeneity of the Rabi frequency.

Another simplification in the model is the assumed next neighbor distribution of the Rydberg atoms that might be influenced by the Rydberg blockade effect. Even though the blockade effect between two atoms during the excitation is included in the simulations, it is not included in the Chandrasekhar distribution function used in the model. It could be addressed by a density distribution that is zero for distances smaller than the blockade radius, effectively narrowing the Rydberg atom distribution.

Despite all these reasons the simulations agree with the experiment and show the applicability of the fully coherent pair state interferometer. It supports the fundamental understanding of the system and offers important inside into the dephasing processes that are unavoidable in an ensemble of atoms. Experiments aiming at using the coherent interaction-induced phase shift have to be considered carefully to suppress or refocus the dephasing.

4 A polar homonuclear molecule

Ultralong-range Rydberg molecules open the field of Rydberg physics towards ultracold chemistry, exhibiting versatile new and interesting properties. However, the creation of the molecules itselve is a challenge that was first met in 2010 in our group [49] by direct photoassociation in an ultracold gas of Rubidium atoms. The experimental requirements are strict. Because of the small binding energies on the order of 10 MHz ultracold temperatures are necessary. Furthermore only close-by atom pairs at the binding length of $r \approx 100\,\mathrm{nm}$ can be photoassociated to the molecular state. High atomic densities above $1 \times 10^{12}\,\mathrm{cm}^{-3}$ are necessary to generate these atom pairs.
All these requirements are perfectly met in trapped, evaporatively cooled gases. A magnetic trapping, in comparison to a dipole trap, is especially favourable as it offers a narrowband excitation and high precision spectroscopy. Therefore the experimental setup here in combination with the narrowband excitation laser system is well suited to create these unusual molecules and to study their properties.

4.1 Stark effect measurements

The ultralong-range Rydberg molecules are created via two-photon photoassociation directly to the bound molecular state and detected by field ionization and ion detection, just as in the case of Rydberg atoms explained in chapter 2.2. The molecules can be excited at slightly lower excitation frequencies than the atomic Rydberg line, where the excitation energy difference is the binding energy. Hence the molecules appear as an additional signal in the spectroscopy, some MHz red detuned to the atomic Rydberg line, which is shown in Figure 4.1 for the ${}^3\Sigma(5s-35s)$ molecules. For photoassociation of the ${}^3\Sigma(5s-35s)$ molecules a σ^+ (780 nm excitation laser) and σ^- (480 nm excitation laser) excitation scheme is used, as shown in Figure 2.3, to fulfill the angular momentum conservation in the excitation. The photoassociation pulses are typically 15 μs long with Rabi frequencies on the order of $2\pi \times 100\,\mathrm{kHz}$ for the excitation to single atom Rydberg states. The experiments are performed at a peak ground state atom density of $\rho = 10^{13}\,\mathrm{cm}^{-3}$, a temperature of 3 μK and an offset magnetic field of 1 G. Details on the photoassociation can be found in [101].
Here, the behavior of the molecules in static electric fields will be studied in spectroscopy

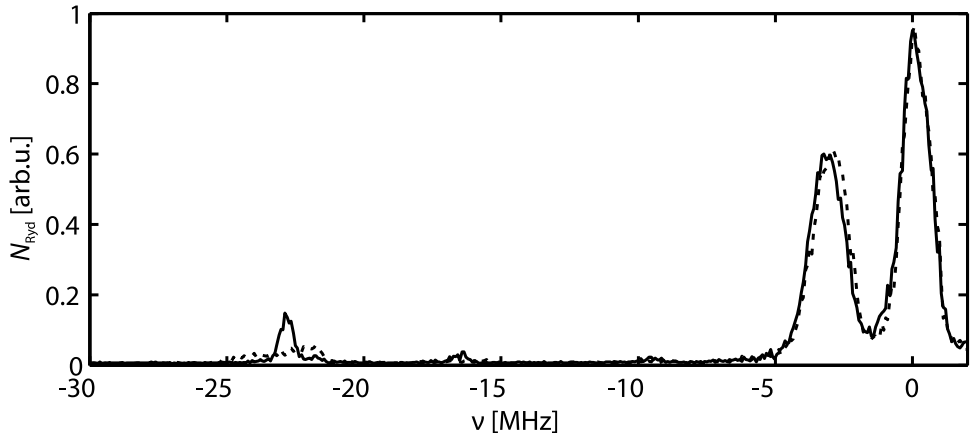

Figure 4.1: Spectroscopy close to the 35s Rydberg line at an electric field of $|\vec{E}| = 0\,\mathrm{V/cm}$ (solid line) and $|\vec{E}| = 3\,\mathrm{V/cm}$ (dashed line). The frequency axis is relativ to the atomic resonance ($35s_{1/2}$, $m_j = 1/2$ at 0 MHz) in each measurement. The additional transition at -3 MHz is the Zeeman splitted $m_j = -1/2$ Rydberg state (see Figure 2.3). The molecular ground state generates a signal at the binding energy of -23 MHz and two vibrationally excited states are at -17 MHz and -9 MHz. At the atomic resonance the ion detector is fully saturated.

experiments. Each measurement of a spectrum consists of a series of 481 sequences of excitation and detection, where the scan range is always chosen relativ to the atomic Rydberg line. Upon applying an electric field during the excitation this resonance frequency is shifted by the Stark effect of the Rydberg atoms and the scan range is simultaneously changed. These spectra are measured for 19 electric fields between -9 V/cm and +9 V/cm. Such a set of measurements is shown in Figure 4.2, displaying a clearly quadratic Stark effect as expected for the Rydberg atoms (equation (1.28)). The molecular line, at slightly smaller frequencies left to the atomic line in Figure 4.2, shows the same shift at first glance.

So far, measurements were not able to detect a deviation of the molecular Stark effect from this quadratic shift within their experimental resolution [101]. The experiments were interpreted by assuming that the molecule possesses only an induced dipole moment that arises from the polarizability of the Rydberg atom. With other words, the bound ground state atom does not perturb the wavefunction of the Rydberg electron and the molecular Stark effect is equal to the atomic Stark effect. The measurement in Figure 4.2 shows this quadratic Stark effect at electric fields of some V/cm, where the molecular Stark effect is indeed dominated by the Rydberg atom.

In order to detect small deviations due to the molecular nature the quadratic Stark effect is subtracted from the spectra. Figure 4.1 shows, besides the spectrum at $|\vec{E}| = 0\,\mathrm{V/cm}$, a shifted spectrum at $|\vec{E}| = 3\,\mathrm{V/cm}$. The frequency axis in both spectra is relativ to the atomic Rydberg line, i.e. the atomic Stark effect is subtracted. The width and the

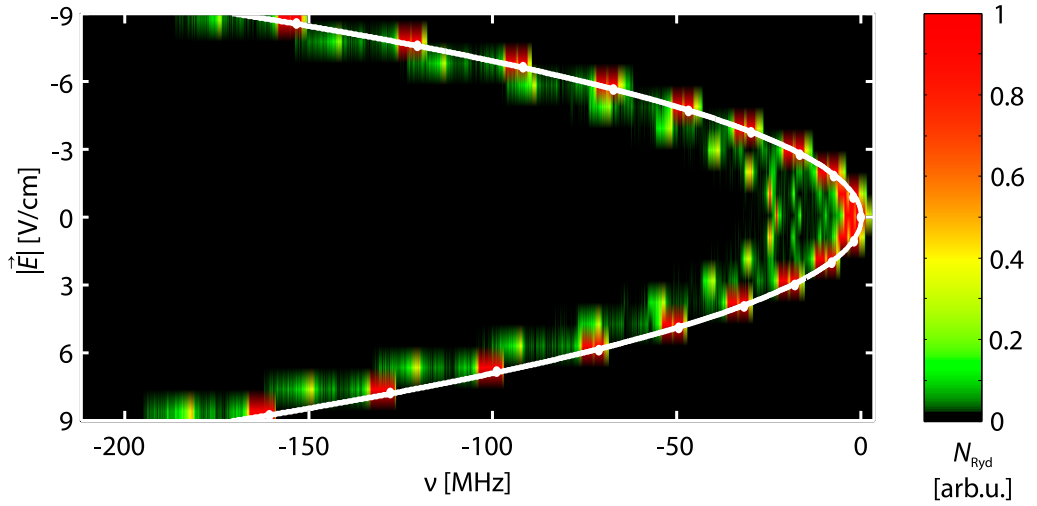

Figure 4.2: Color coded two-dimensional Stark spectrum of the atomic 35s Rydberg line (white dots) and the molecular $^3\Sigma(5s-35s)$ lines (left to the atomic line). The white line shows a quadratic fit to the atomic line.

amplitude of the atomic Rydberg line are unchanged, but the ground state molecular line clearly shows a broadening and a shift of the line center relative to the atomic Rydberg line. As the atomic Stark effect is subtracted, this additional effect is a pure molecular Stark effect due to a perturbed Rydberg electron wavefunction in the presence of the bound ground state atom. In Figure 4.3 (c) the full high resolution molecular Stark spectrum is shown, where the frequency range is chosen such that the strong and saturated atomic Rydberg line is excluded. This is the same data as in Figure 4.2, where the atomic Stark effect is subtracted. No splitting of rotational states is visible, but a continuous broadening of the molecular lines, resulting in a Stark-fan. Note that this shift is on the order of some MHz at 9 V/cm, whereas the quadratic atomic Stark shift is about 170 MHz at the same field.

Figure 4.3 also shows calculated Stark spectra of the $^3\Sigma(5s-35s)$ molecules, that were calculated at the Max-Planck-Institut für Physik komplexer Systeme in Dresden [50]. In these calculations the molecular potential is calculated by direct diagonalization of

$$H = H_A + \hat{V} + \vec{E}\vec{r}, \tag{4.1}$$

where H_A is the unperturbed Rydberg atom Hamiltonian, $\hat{V}$ the Fermi pseudopotential interaction (1.55) and $\vec{E}\vec{r}$ describes the interaction with the external electric field $\vec{E}$. This diagonalization is done for many different molecular orientations to calculate the ro-vibrational states of the molecule in this potential. A considerably reduced basis size was used to reduce the computational effort, but that also leads to an error of about 1 MHz in the binding energies of the molecules.

Figure 4.3 (a) shows the Stark shifts of the pure ro-vibrational states. Even in zero electric field the vibrational states, already shown in Figure 1.18, split in rotationally

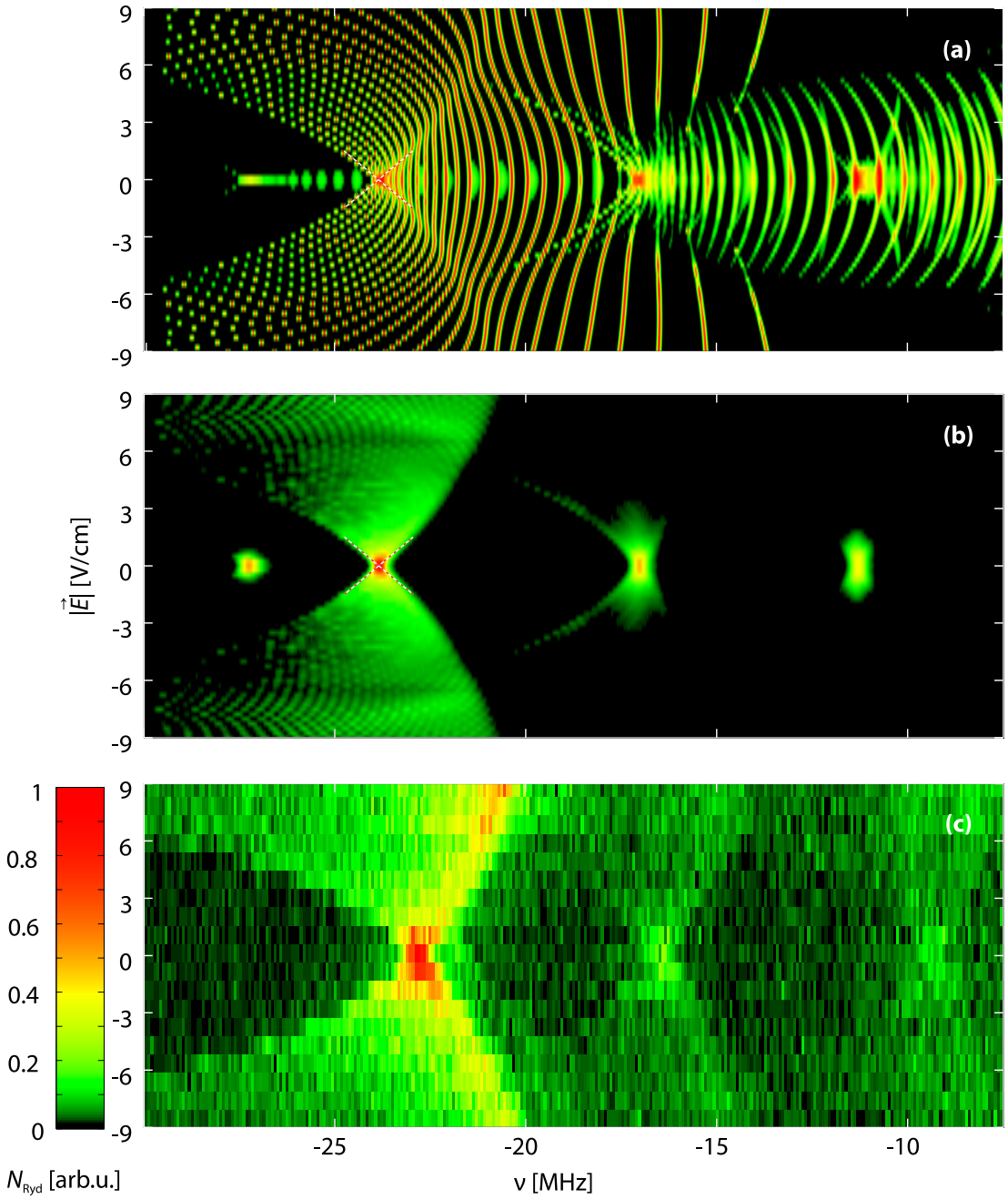

Figure 4.3: Two-dimensional Stark spectra of $^3\Sigma(5s-35s)$ molecules. The frequency axis is relative to the atomic Rydberg line in every spectrum. (a) The calculated Stark spectrum of several angular states of the ro-vibrational lines including their theoretically predicted minimum linewidth. (b) Thermal averaged theoretical photoassociation spectrum including the experimentally obtained minimal linewidth of 142 kHz. Note that many of the states shown in (a) are not present because of the vanishing angular overlap with the initial thermal gas state. (c) Measured Stark spectrum. The absolute frequency deviation of about 1 MHz to the calculated spectra is because of a reduced basis set in the calculations.

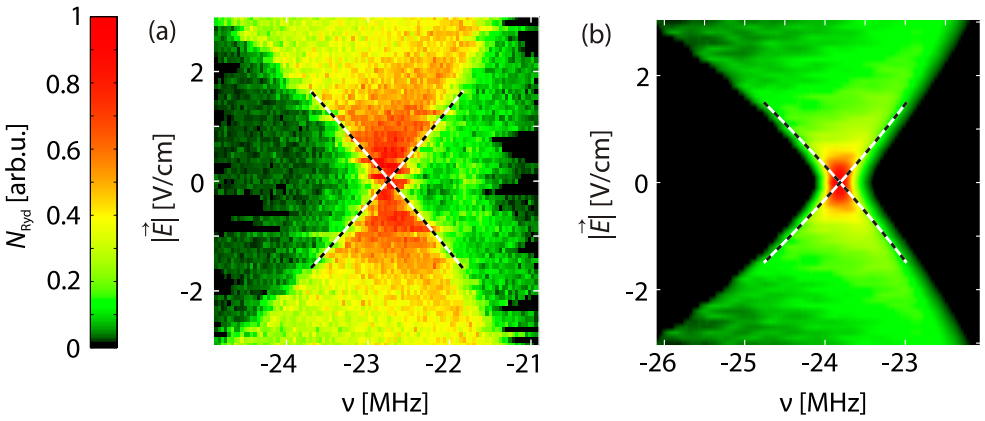

Figure 4.4: High resolution molecular Stark maps of the $^3\Sigma(5s-35s)$ molecule, where the atomic Stark effect is subtracted. (a) shows measured data and (b) shows calculations. The frequency axis is relative to the atomic Rydberg resonance. The dashed lines are results of the fits to the wings of the Stark fan to determine the dipole moment.

excited substates. These calculations include only the lifetime-limited linewidth of the molecular state, but no experimental broadening or thermal effects.
Figure 4.3 (b) includes the experimentally obtained linewidth of the molecular state of 142 kHz [93] and a thermal averaging. In photoassociation the final rotational state is determined by the initial angular momentum of the atoms before photoassociation. A thermal distribution at 3 μK defines the possible angular momenta and the Frank-Condon overlap of the initial and final states. From this overlap the strength of the respective resonance in the photoassociation spectrum can be calculated and is included in Figure 4.3 (b). Many of the ro-vibrational states are not visible here as their angular momenta do not appear in the thermal gas. This photoassociation spectrum is in remarkable agreement with the measurements (Figure 4.3 (c)) without any adjustible parameters.

4.2 Determination of the permanent dipole moment

The permanent space-fixed dipole moment, that was calculated in chapter 1.4.2, manifests itself as a linear Stark shift of the molecular line at small electric fields. In strong electric fields the induced dipole moment exceeds the permanent dipole moment and the linear Stark shift is covered by the dominating quadratic Stark effect, as visible from Figure 4.2. Therefore high precision spectroscopy of the Stark effect at small electric fields is necessary to determine the permanent dipole moment. Figure 4.4 (a) shows such a high resolution spectrum of the molecular ground state, where the quadratic Stark effect is already subtracted as in Figure 4.3 (c). For these measurements a 4 MHz wide spectrum consisting of 101 datapoints centered at the molecular resonance followed by

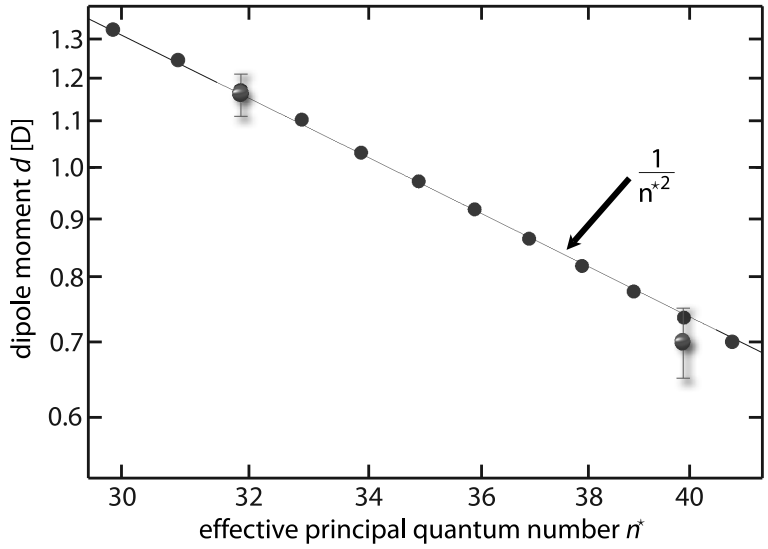

Figure 4.5: Permanent electric dipole moment d of the molecular $^3\Sigma(5s - ns)$ ground state as a function of the effective principal quantum number $n^\star$. The dots show the results of the numerical calculations and the datapoints represent the experimentally obtained dipole moments, including errorbars from the standard deviation of the fits to the experimental data. The solid line is a $(n^\star)^{-2}$ fit to the calculated data, indicating the scaling behavior.

a 20 MHz wide spectrum of 201 datapoints at the atomic resonance was measured in one atomic sample for every electric field. Thereby the molecular and the atomic Stark shift could be measured simultaneously and the atomic Stark effect could be subtracted from the molecular shift.
The origin of this continuous Stark fan can be understood quite simple. In the experiments the orientation of the molecular axis is not controlled and the molecules are created in charge-localized, randomly oriented states. The strongest and weakest Stark effects appear for molecules aligned parallel and antiparallel to the electric field. Inbetween these extrema an intermediate Stark effect emerges and a fan is visible in the electric field in Figure 4.4. The limits of the fan are given by the Stark effects $\Delta E_{\mathrm{Stark}}$ of the parallel and antiparallel orientations. The gradient at $|\vec{E}| = 0\,\mathrm{V/cm}$ of these maximal shifts corresponds to the dipole moment as

$$d = h \cdot \left.\frac{\partial(\Delta E_{\mathrm{Stark}})}{\partial|\vec{E}|}\right|_{|\vec{E}|=0\mathrm{V/cm}} . \tag{4.2}$$

To determine the permanent dipole moment from the experimental data the points at which the Rydberg signal drops to half its maximal value were found for each electric field. A fit of a second-order polynomial to these data (dashed lines in Figure 4.4) yields the permanent electric dipole moment as the gradient at zero electric field, following equation (4.2). This procedere was also applied to the numerically calculated spectra

(Figure 4.4 (b)) and an agreement with the calculated dipole moment was found within the standard deviation of the fit.
In the case of the $^3\Sigma(5s-35s)$ molecule, that is shown in Figure 4.4, the obtained value of the dipole moment is 1.16(5) Debye. A similar measurement for the $^3\Sigma(5s-43s)$ molecular state yields 0.70(5) Debye. These values are in exellent agreement with the theoretical values of 1.17 Debye and 0.75 Debye, as also visible in Figure 4.5.

This measurement of a linear Stark effect at small electric fields is the first experimental proof of a permanent space-fixed dipole moment in a homonuclear molecule. A similar but larger dipole moment was proposed in pure high-l trilobite molecules, but these states have not yet been observed. However, these experiments show that even the low-l molecules feature a considerable mixing with the trilobite state that leads to the observed permanent dipole moment. Therefore the low-l ultralong-range Rydberg molecules can also be attributed to the class of trilobite molecules. This character is explicitly apparent in the probability density of the Rydberg electron in Figure 1.19.

5 Conclusion and outlook

Conclusion

The presented work consists of two parts. In one part Stark-tuned Förster resonances between 44d states were studied using a pulsed Ramsey excitation scheme. The resolution of the Förster defect in the electric field exceeds all previous studies of this resonance thanks to the narrow linewidth laser system. The Ramsey technique forms a novel approach to study the involved pair states by measuring the total Rydberg atom number only. Previous approaches used technically more demanding state selective field ionization. Besides the spectral resolution, Ramsey spectroscopy offers to obtain information about the coherence in the system. The extension to double Ramsey experiments, where a pulsed sequence in the interaction strength is realized, even allows following the coherent time evolution of the pair state system at Förster resonance. Oscillations with the effective Rabi frequency between coupled pair states were observed and a Förster interaction-induced phase shift of the Rydberg atoms could be measured and controlled by the electric field.
Calculations of the resonant electric fields and of the angular dependence and strength of the resonances form the basis to simulate the experiments using the introduced pair state interferometer. These fully coherent many-level simulations are in very good agreement with the observations and prove the coherent evolution of the ensemble of atoms in the presence of interactions. An observed loss of visibility in the interference fringes of the Ramsey experiments in the presence of strong interactions could be reproduced in the fully coherent simulations and clearly be attributed to a dephasing within the coherent pair state system.
A second part of this work focuses on the permanent electric dipole moment of the ultralong-range Rydberg molecules. Usually, symmetry arguments do not allow for permanent dipole moments in homonuclear diatomic molecules. Here, the unusual binding mechanism, based on electron scattering, gives rise to a body-fixed dipole moment. The huge binding length originates in unusually long exchange times and a large rotational constant, which are responsible that the body-fixed dipole moment also appears as a measureable space-fixed dipole moment, effectively leading to a symmetry breaking on the timescale of the experiments.

In high-resolution spectroscopy of the molecular Stark effect a linear Stark shift was measured and the permanent dipole moment was obtained, in perfect agreement to theoretical predictions.

Outlook

Ultracold Rydberg physics is a rich field that will surely show many advances and surprising results in the future. Many proposals exist, but often the technical limitations are more restricting than the theoretical ideas. Therefore I will first discuss improvements of the current experiments before I point out additional experiments that are of interest.

Improvement of the current experiments

The presented Ramsey-like experiments at the Förster resonance are limited by several effects. One simple point is the diabatic, sudden switching of the Förster defect by the electric field pulse in the measurement of the phase shift (see Figure 3.14). In the case of adiabatic switching, where the system remains in the initial state $|rr\rangle$, no population transfer to $|r'r''\rangle$ occurs. This would have two advantages. First of all, a large phase shift directly at the resonant electric field of the Förster resonance, where so far no phase shift occured because of mixing of different states, would be observable. Secondly, the population transfer to $|r'r''\rangle$ in the case of diabatic switching leads to a loss of visibility. If the electric fields are adiabatically switched no atoms are transferred and a higher visibility is measured, making it easier to observe the phase shift. This adiabatic switching can easily be realized by ramping the electric fields close to the Förster resonance. Care has to be taken not to adiabatically transfer the atoms at resonances in lower fields ($|pf_2\rangle - |pf_4\rangle$ in Figure 1.15), similar to a Landau-Zener sweep. Therefore the electric field can either be switched diabatically to about $|\vec{E}| = 0.21\,\mathrm{V/cm}$, above $|pf_2\rangle$, and then ramped adiabatically to the resonant field, or the excitation is already done in a high electric field. Then the resonance can be addressed by ramping the electric field down.

A fundamental limitation of the coherence in these experiments is the finite excitation linewidth of 300 kHz, as nicely visible in the measurement of the maximum coherence time of 0.5 μs in chapter 3.2.2. This linewidth is generated by a magnetic field dependence of the excitation transition to the Rydberg d state and possibly by electric field inhomogeneities. Reducing this linewidth would allow to apply longer pulse sequences and enhance for example the observed phase shift.
This can be done in several ways. While improving the electric field homogeneity is only a technical challenge, the broadening by the magnetic field dependence of the excitation

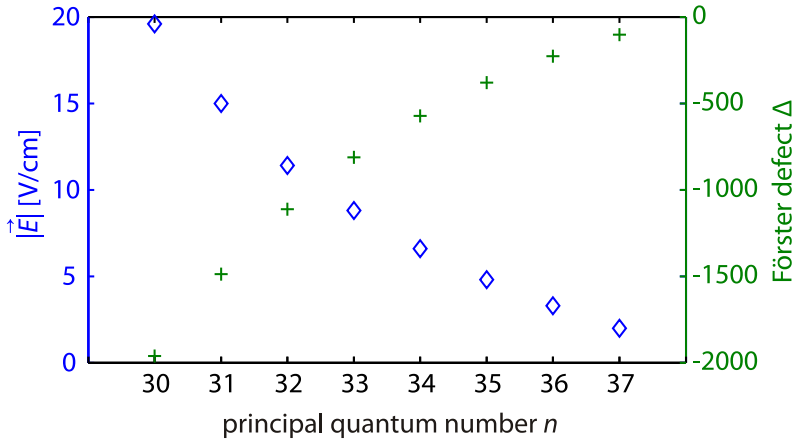

Figure 5.1: Resonant electric fields (blue diamonds and left axis) and zero-field Förster defects (green crosses and right axis) for the resonances $ns_{1/2} + (n+1)s_{1/2} \rightarrow np_{3/2} + np_{3/2}$ versus the principal quantum number n.

to the d state cannot be avoided in a magnetic trap. One possible solution is a blue detuned dipole trap, a so-called 'bottle beam' trap [138]. In these blue detuned traps the atoms are low field seekers and a local minimum in the intensity profile has to be generated, usually by interferometric methods. While usual red detuned dipole traps do not trap Rydberg atoms due to different polarizabilities of ground and Rydberg state, these bottle beam traps can operate at a magic wavelength (about 430 nm for ^{87}Rb), that simultaneously traps ground state and Rydberg atoms [139]. In these traps the magnetic field is a fully free parameter and the transition to the d state is not broadened by the inhomogeneous fields.

Another possibility to avoid the magnetic field broadening in the magnetic trap is to use an excitation to an s state, that is not magnetic field dependent (Table 1.3). Förster resonances can also be found for s states; however, two different Rydberg s states have to be addressed for the Förster resonance

$$ns_{1/2} + (n+1)s_{1/2} \rightarrow np_{3/2} + np_{3/2} \tag{5.1}$$

that is, for example, used in [24]. Figure 5.1 shows the electric fields to tune the pair states into resonance and the Förster defect at $|\vec{E}| = 0\,\mathrm{V/cm}$ versus the principal quantum number. These pair states cannot be Stark-tuned into resonance for $n > 37$. However, the resonant electric fields are magnetic field dependent (see Chapter 1.3.3) because of the Zeeman shifts between the s and the p states. The differential Zeeman shift of the pair states is $2\,\mu_B$B for the resonance including the stretched states. Hence a broadening of the Förster resonance on the order of 100 kHz, similar to the magnetic field dependent transition to the d states, is expected in the magnetic trap that reduces coherence times at resonance.

But this resonance shows another advantage. The initially excited s states split twofold

in the magnetic field, but both Zeeman states show the same Stark effect. In contrast to d states (Figure 3.3) no crossings of single-atom states appear in a combined electric and magnetic field that lead to dephasing. Therefore the experimentally accessible magnetic field range is broader.

One striking advantage of the performed Ramsey experiments with switched interactions is that the interaction strength during the delay time is not limited by the excitation linewidth. In single pulse Rydberg experiments the interaction strength between two atoms cannot exceed the laser linewidth or the Rabi frequency, whatever is bigger, because of the blockade effect. But if the interaction strength is increased after excitation this limitation can be avoided, as in the experiments presented here. Of course this depends on the range over which the interaction strength can be tuned. Best results can be obtained if the system shows a very large Förster defect (small interactions) in zero field, that can be tuned to resonance in a finite field. The resonance $2 \times 44\mathrm{d}_{5/2} \rightarrow 42\mathrm{f} + 46\mathrm{p}_{3/2}$ used in this work shows $\Delta = 63\,\mathrm{MHz}$ Förster defect. This can be increased to 300 MHz at $50d_{5/2}$ [79]. Using the resonance in equation (5.1) the Förster defect can exceed 1000 MHz (cp. Figure 5.1). This would reduce the interaction during excitation and support the tunability of the interaction and the coherent control.
A disadvantage of the resonance in equation (5.1) is a rather strong electric field to tune the pair states into resonance. This imposes bigger demands onto the electric field stability. Furthermore, these experiments are technically considerably more difficult as the excitation of two Rydberg states requires two laser systems for the upper Rydberg transition of about 480 nm.

Rydberg correlation function and interaction strength

An interesting situation occurs if the ensemble is driven into a steady state situation. Under certain parameters the ground state of the system is expected to form a crystalline structure [125, 140, 141] of the Rydberg excitation and shows a quantum phase transition. This is reached by adiabatically ramping the Rabi frequency and the detuning of the excitation lasers from the ground state of all atoms to the ground state of the system in the presence of the Rydberg excitation. Coherent control of the strongly interacting system, as shown in this thesis, is a fundamental requirement for these proposals.
Non-adiabatic switching of the excitation lasers would not create a perfect crystalline structure. Nevertheless it could lead to a locally ordered state, showing a structured Rydberg correlation function, if the system is driven into full blockade where the Rydberg-Rydberg distance is given by the blockade radius. This can be experimentally difficult due to limited Rabi frequencies or, as in the experimental setup here, because a too high Rydberg atom number saturates the detector.

However, also the detection of the structured Rydberg distribution is challenging. One possibility might be offered by the presented Ramsey experiments. In this crystalline structure the dephasing due to the inhomogeneous distribution of Rydberg atoms, that creates a band of interaction strengths, is reduced [135]. Especially in the case of short-range van der Waals interactions, where next neighbor interactions are dominant, a fully crystalline or at least locally correlated Rydberg distribution would result in a narrow distribution in the interaction strength. The coupling strength in these systems would cause oscillations with the effective Rabi frequency in the presented double Ramsey experiments at small Förster defects. Single pulse experiments (chapter 3.2.4) at Förster resonance would possibly show direct Rabi oscillations between the involved pair states. Both approaches would be a direct measure of the interaction strength, that was calculated in chapter 1.3.5, and at the same time a measure of the Rydberg-Rydberg correlation function, possibly showing a hint to the crystalline structure.
In order to measure the interaction strength this crystalline structure could also be artificially generated, if a high optical resolution below the scale of the blockade radius allows exciting spatially resolved single Rydberg atoms.
However, the measurement of the interaction strength would necessitate a very pronounced Rydberg correlation function. To measure the coupling strength by pair state oscillations the coupling strength has to be at least on the order of the Förster defect. This is also the border between van der Waals and long-range dipole-dipole interaction, where next-next neighbors might contribute and it makes the interaction strength more sensitive to inhomogeneities in the possible crystal. Also, the $1/r^3$- or even $1/r^6$-dependence of the interaction strength at resonance is very sensitive to even small variations in the Rydberg-Rydberg distance, leading to a damping of Rabi oscillations between the pair states. Therefore especially the experiments at resonance seem challenging, but there might be a range of small Förster defects that allow measuring the interaction strength and getting information about the correlation length in the oscillations between pair states.

Angular interaction dependence

Besides the interaction strength also the angular dependence of the interaction at a Förster resonance is of interest. The different Förster resonances show different angular dependencies because of couplings between oscillating dipole moments of different polarization. This dependency can be measured by rotating the electric field in a sample of reduced dimensionality. Angular dependent interaction strengths would show as angular dependent excitation numbers due to the blockade effect. In [142] this angular dependence was measured in an almost one-dimensional excitation volume at a Stark-tuned Förster resonance. In this experiment several states contributed to the observed angular dependence. Making use of the high resolution in the Förster defect as presented in

this thesis, it should be possible to resolve the different angular dependencies of several resonances, as shown in Figure 1.12.
Another, more indirect way to measure the angular dependence could be using rotary echo or Ramsey-like experiments in the interaction strength. By switching the electric field from one resonance to another resonance, showing a different angular dependence, revivals in the coherence could be observed. These revivals would depend on the differences in the angular dependence and the strength of the interaction between the resonances.

Rydberg dressing

Another topic that gained much research interest in the last years is Rydberg dressing [143, 144]. The idea is the following: Off-resonant excitation of a Bose-Einstein condensate on the ms-timescale to an interacting Rydberg state admixes a small fraction of Rydberg excitation to the ground state atoms. Due to the detuning this fraction is small to ensure long enough lifetimes of the dressed states, but it still induces interaction between the trapped atoms. This may lead to a large variety of effects like modified ground state trapping potentials [145], crystalline phases [146], solitons [147] and rotons [148].
Rydberg dressing is a prototype case for a situation, where the possibilities are clearly limited by experimental constraints and not by theoretical ideas. Especially limited Rabi frequencies and insufficient control over density, stability and purity of Bose-Einstein condensates precluded a conclusive experimental observation so far.
However, experimentally Rydberg dressing might benefit from Förster resonances. The possible tuning of the strength, the sign and the angular dependence of the interaction at resonance can offer an important tool to indicate the effects of Rydberg dressing and to differentiate between dressing and thermal effects. This would possibly also offer to measure the angular dependence of the interaction.

Energy transport processes

Energy transport processes received much attention since the experimental observation of quantum coherence in photosynthetic complexes [32, 33]. Energy transport in these quantum aggregates is driven by non-radiativ coupling of degenerate dipole transitions, so called Förster resonance energy transfer (FRET). These processes can possibly be simulated using ultracold atoms and Förster resonances between Rydberg atoms. The molecular aggregates strongly couple to the environment causing dephasing, which complicates the theoretical description and understanding. Contrary, ultracold atoms usually hardly couple to the environment, but such a dephasing can be induced by external fields. This allows adding controlled dephasing mechanisms to study influences

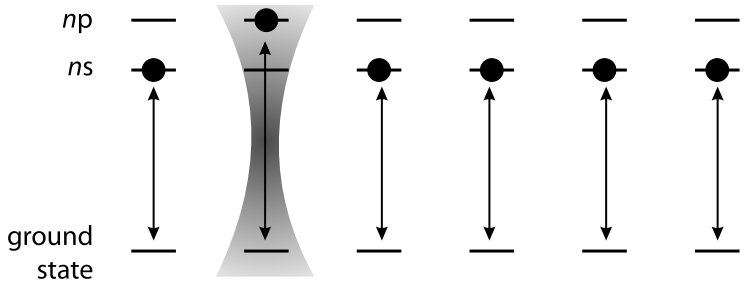

Figure 5.2: Sketch of the initial Rydberg atom distribution in the linear chain. The spatially resolvable excitation laser is indicated.

of different couplings and to test theoretical treatments in detail.
Before simulating complex quantum aggregates including dephasing, e.g. the FMO complex in photosynthesis [34], energy transfer in linear chains would be the first goal [29, 37, 149]. Therefore a linear chain of Rydberg atoms, for example in s states, has to be prepared with single Rydberg atoms as impurities in a p state (Figure 5.2). This can either happen by a chain of atomic traps in an optical lattice or micro-lens array, each holding one Rydberg excitation, or by spatially resolved excitation of the Rydberg chain in an experiment offering optical resolution below the blockade radius. Since the s and p state atoms non-radiatively couple the impurity will delocalize over the chain to form an exciton. The exciton dynamics can then be studied in the presence of an energy gradient along the chain or in the presence of noise.
Excitation of the p state demands an additional microwave field that couples the p state to the s state. As microwave fields do not offer spatial resolution, this resolution in the excitation of single p state Rydberg atoms has to be realized by electric field gradients or direct three photon excitation, where the optical transitions are spatially resolved as shown in Figure 5.2. A possible spatially resolved detection scheme relies on a Raman transition to a considerably different Rydberg state and state selective field ionization.
In order to understand more complex quantum aggregates the role of dephasing and noise due to the coupling to the environment must be studied. In an ultracold atom system this dephasing can be induced by electric field noise and inhomogeneities. If Stark-tuned Förster resonances are used even spatially different coupling strengths can be realized by spatial control of electric fields.

Single photon source

Another recent development are single photon sources based on Rydberg excitation in ultracold atoms [56], following a similar proposal from Saffman and Walker [54]. Single photon sources are an important building block for quantum communication and cryptography applications. In [56], the atoms were spatially confined in a 1D optical

lattice loaded from an optical molasses to a size smaller than the blockade sphere. The single photon source is realized by a four-wave mixing process including a high-lying Rydberg state. A two-photon excitation (795 nm and 475 nm) generates a single collective Rydberg excitation, also described by a spin wave, in the sample. Several excitations are impossible due to the Rydberg blockade. After a storage time another laser pulse at 475 nm, forming a read-out pulse, converts the spin wave into an emitted phase-matched photon at 795 nm to fulfill the four-wave mixing process. As Rydberg blockade allows only a single Rydberg excitation in the spatially confined ensemble, only a single photon is emitted, realizing a single photon source.
This idea can be expanded to ensembles bigger than the blockade sphere, as proposed in [55]. Multiple Rydberg excitations are not prevented, but instead the collective Rydberg state is dephased due to interactions during the storage time in the case of more than one Rydberg excitation. This dephasing suppresses the four-wave mixing process by destructive interference of distinct atom pair contributions and no phase-matched photons are generated. Only in the case of a single Rydberg excitation no interactions arise and the system does not dephase, resulting in the generation of a single photon.
The necessary interactions can be induced by coupling additional states with microwaves, as proposed in [55], or with Stark-tuned Förster resonances, exactly as it is done in chapter 3.2.2. The decoherence that is used in the proposed single photon source is visible as a loss of visibility in the Ramsey experiments at the Förster resonance. The realized interaction-induced coherence time of 0.7 μs at resonance is within the experimental storage times reported in [56].
In the experiments in this work always a great number of Rydberg excitations were generated in the cloud and the distances between the excitations were therefore small. This enhances the interaction and the dephasing, but for the single photon source even two excitations at the largest possible distance in the cloud have to dephase. It can only be realized if the interaction between all possible distributions of two excitations in the sample is strong enough to dephase the collective states during the storage time. This increases the dephasing times and puts some limits on the size of the sample. The experimental setup here produces thermal clouds of about 80 μm length, which corresponds to the parameters used in [55]. This reduces the interaction to some kHz at the Förster resonance used in this work and necessitates long storage times of several tens of μs that are challenging to realize. But for example in experiments offering spatial resolution of the exciting lasers the interaction volume can easily be reduced and this proposed single photon source using Rydberg interaction induced dephasing seems realistic.

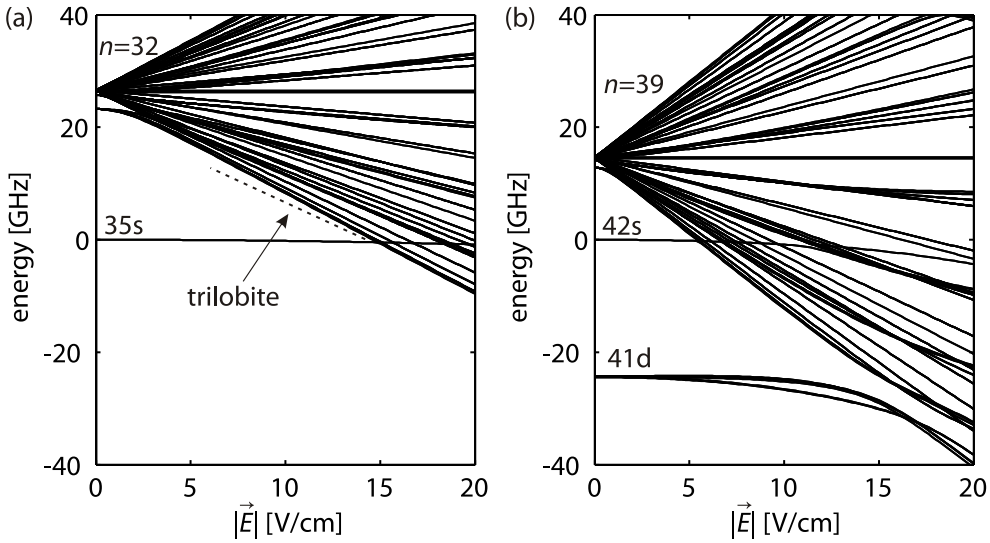

Figure 5.3: Stark spectra in the vicinity of the 35s state (a) and the 43s state (b). The manifold states cross with the s states in strong fields. The plotted trilobite line (dashed line) is only a rough indicator and no result of calculations.

Ultralong-range Rydberg molecules

Ultralong-range Rydberg molecules showed surprising properties in many fields and there are more to expect. Recent work indicates that the magnetic field dependence can be described as a coupled three spin system [150]. The Rydberg electron (spin 1/2) couples to the bound ground state atom in the s state including electron and nuclear spin. This leads to more splittings in the magnetic field compared to the atomic state and is studied by high-resolution spectroscopy in varying magnetic fields.
Another interesting molecular state arises from a Rydberg atom in a high-l state. The molecular bound states between one high-l Rydberg atom and one ground state atom, called trilobite states, show binding energies of about 15 GHz for $n = 32$. Their permanent dipole moments are on the order of 1000 Debye, three orders of magnitude larger than the observed dipole moments in this work. As no direct two-photon excitation to high-l states is possible additional microwave fields are necessary for photoassociation at zero electric field.
In strong electric fields direct two-photon excitation is possible due to a mixing of several states. For example, the 35s state forms avoided crossings with the $n = 32$ manifold at about 15 V/cm, visible in Figure 5.3 (a). At slightly smaller fields of about 11 V/cm the molecular trilobite states have about 5-10% contribution of the atomic s state, enabling direct two-photon photoassociation of the trilobites. The molecules have binding energies of 1.5 GHz in that field (indicated by the dashed line in Figure 5.3) and can spectroscopically be found on the order of 1 GHz blue detuned to the atomic s state resonance [151]. For higher principal quantum numbers the excitation might be

possible at smaller electric fields. The level spacing scales with $1/n^3$ and the necessary mixing between manifold and the s state occurs at smaller electric fields, for example for the 43s state at 5.5 V/cm 5.3 (b).
Despite the fact that this offers direct photoassociation the experimental challenge would be to find the photoassociation line of the molecules in a spectrum at GHz detuning to the atomic reference line. Furthermore, due to the large permanent dipole moment the trilobite line is very sensitive to electric fields. On the short timescales of the experiment the molecules are directly excited in charge localized but randomly oriented states, giving rise to a fan-like broadening of the excitation line similar to the observation in Figure 4.4.

References

[1] C. N. Cohen-Tannoudji and W. D. Phillips, *New Mechanisms for Laser Cooling*, Physics Today, **43**, 33 (1990).

[2] Nobelprize.org, *The Nobel Prize in Physics 1997*, http://www.nobelprize.org.

[3] Nobelprize.org, *The Nobel Prize in Physics 2001*, http://www.nobelprize.org.

[4] M. Kasevich, E. Riis, S. Chu and R. DeVoe, *rf spectroscopy in an atomic fountain*, Physical Review Letters, **63**, 612–615 (1989).

[5] G. K. Campbell and W. D. Phillips, *Ultracold atoms and precise time standards*, Philosophical Transactions of the Royal Society A: Mathematical, Physical and Engineering Sciences, **369**, 4078–4089 (2011).

[6] V. Giovannetti, S. Lloyd and L. Maccone, *Advances in quantum metrology*, Nature Photonics, **5**, 222–229 (2011).

[7] S. Dimopoulos, P. Graham, J. Hogan and M. Kasevich, *Testing General Relativity with Atom Interferometry*, Physical Review Letters, **98** (2007).

[8] R. P. Feynman, *Simulating physics with computers*, International Journal of Theoretical Physics, **21**, 467–488 (1982).

[9] I. Buluta and F. Nori, *Quantum Simulators*, Science, **326**, 108–111 (2009).

[10] I. Bloch, J. Dalibard and S. Nascimbène, *Quantum simulations with ultracold quantum gases*, Nature Physics, **8**, 267–276 (2012).

[11] J. Simon, W. S. Bakr, R. Ma, M. E. Tai, P. M. Preiss and M. Greiner, *Quantum simulation of antiferromagnetic spin chains in an optical lattice*, Nature, **472**, 307–312 (2011).

[12] L. D. Carr, D. DeMille, R. V. Krems and J. Ye, *Cold and ultracold molecules: science, technology and applications*, New Journal of Physics, **11**, 055049 (2009).

[13] H. Weimer, M. Müller, I. Lesanovsky, P. Zoller and H. P. Büchler, *A Rydberg quantum simulator*, Nature Physics, **6**, 382–388 (2010).

[14] T. F. Gallagher, *Rydberg atoms*, Cambridge University Press, Cambridge, 1 edition (1994).

[15] J. M. Raimond, G. Vitrant and S. Haroche, *Spectral line broadening due to the interaction between very excited atoms: 'the dense Rydberg gas'*, Journal of Physics B: Atomic and Molecular Physics, **14**, L655–L660 (1981).

[16] K. Safinya, J. Delpech, F. Gounand, W. Sandner and T. Gallagher, *Resonant Rydberg-Atom-Rydberg-Atom Collisions*, Physical Review Letters, **47**, 405–408

(1981).

[17] R. Kachru, N. Tran and T. Gallagher, *Microwave-Assisted Resonant Collisional Energy Transfer in Na Rydberg States*, Physical Review Letters, **49**, 191–194 (1982).

[18] S. Westermann, T. Amthor, A. L. d. Oliveira, J. Deiglmayr, M. Reetz-Lamour and M. Weidemüller, *Dynamics of resonant energy transfer in a cold Rydberg gas*, The European Physical Journal D, **40**, 37–43 (2006).

[19] R. Zanon, K. Magalhães, A. d. Oliveira and L. Marcassa, *Time-resolved study of energy-transfer collisions in a sample of cold rubidium atoms*, Physical Review A, **65** (2002).

[20] T. Vogt, M. Viteau, J. Zhao, A. Chotia, D. Comparat and P. Pillet, *Dipole Blockade at Förster Resonances in High Resolution Laser Excitation of Rydberg States of Cesium Atoms*, Physical Review Letters, **97**, 083003 (2006).

[21] K. Afrousheh, P. Bohlouli-Zanjani, D. Vagale, A. Mugford, M. Fedorov and J. Martin, *Spectroscopic Observation of Resonant Electric Dipole-Dipole Interactions between Cold Rydberg Atoms*, Physical Review Letters, **93**, 233001 (2004).

[22] I. Mourachko, W. Li and T. Gallagher, *Controlled many-body interactions in a frozen Rydberg gas*, Physical Review A, **70**, 031401 (2004).

[23] A. Reinhard, K. Younge, T. Liebisch, B. Knuffman, P. Berman and G. Raithel, *Double-Resonance Spectroscopy of Interacting Rydberg-Atom Systems*, Physical Review Letters, **100**, 233201 (2008).

[24] I. I. Ryabtsev, D. B. Tretyakov, I. I. Beterov and V. M. Entin, *Observation of the Stark-Tuned Förster Resonance between Two Rydberg Atoms*, Physical Review Letters, **104**, 073003 (2010).

[25] A. Tauschinsky, C. van Ditzhuijzen, L. Noordam and H. van den Heuvell, *Radio-frequency-driven dipole-dipole interactions in spatially separated volumes*, Physical Review A, **78**, 063409 (2008).

[26] M. Reetz-Lamour, T. Amthor, J. Deiglmayr and M. Weidemüller, *Rabi Oscillations and Excitation Trapping in the Coherent Excitation of a Mesoscopic Frozen Rydberg Gas*, Physical Review Letters, **100**, 253001 (2008).

[27] U. Raitzsch, V. Bendkowsky, R. Heidemann, B. Butscher, R. Löw and T. Pfau, *Echo Experiments in a Strongly Interacting Rydberg Gas*, Physical Review Letters, **100**, 013002 (2008).

[28] W. Anderson, M. Robinson, J. Martin and T. Gallagher, *Dephasing of resonant energy transfer in a cold Rydberg gas*, Physical Review A, **65**, 063404 (2002).

[29] R. Côté, A. Russell, E. E. Eyler and P. L. Gould, *Quantum random walk with Rydberg atoms in an optical lattice*, New Journal of Physics, **8**, 156 (2006).

[30] T. Förster, *Zwischenmolekulare Energiewanderung und Fluoreszenz*, Annalen der Physik, **437**, 55–75 (1948).

[31] T. G. Walker and M. Saffman, *Zeros of Rydberg–Rydberg Föster interactions*, Journal of Physics B: Atomic, Molecular and Optical Physics, **38**, S309–S319 (2005).

[32] G. S. Engel, T. R. Calhoun, E. L. Read, T.-K. Ahn, T. Mančal, Y.-C. Cheng, R. E. Blankenship and G. R. Fleming, *Evidence for wavelike energy transfer through quantum coherence in photosynthetic systems*, Nature, **446**, 782–786 (2007).

[33] G. Panitchayangkoon, D. Hayes, K. A. Fransted, J. R. Caram, E. Harel, J. Wen, R. E. Blankenship and G. S. Engel, *Long-lived quantum coherence in photosynthetic complexes at physiological temperature*, Proceedings of the National Academy of Sciences, **107**, 12766–12770 (2010).

[34] M. B. Plenio and S. F. Huelga, *Dephasing-assisted transport: quantum networks and biomolecules*, New Journal of Physics, **10**, 113019 (2008).

[35] C. Olbrich, T. L. C. Jansen, J. Liebers, M. Aghtar, J. Strümpfer, K. Schulten, J. Knoester and U. Kleinekathöfer, *From Atomistic Modeling to Excitation Transfer and Two-Dimensional Spectra of the FMO Light-Harvesting Complex*, The Journal of Physical Chemistry B, **115**, 8609–8621 (2011).

[36] O. Mülken, A. Blumen, T. Amthor, C. Giese, M. Reetz-Lamour and M. Weidemüller, *Survival Probabilities in Coherent Exciton Transfer with Trapping*, Physical Review Letters, **99**, 090601 (2007).

[37] S. Möbius, S. Wüster, C. Ates, A. Eisfeld and J. M. Rost, *Adiabatic entanglement transport in Rydberg aggregates*, Journal of Physics B: Atomic, Molecular and Optical Physics, **44**, 184011 (2011).

[38] R. Blatt and D. Wineland, *Entangled states of trapped atomic ions*, Nature, **453**, 1008–1015 (2008).

[39] M. Saffman, T. Walker and K. Mølmer, *Quantum information with Rydberg atoms*, Reviews of Modern Physics, **82**, 2313–2363 (2010).

[40] D. Jaksch, J. I. Cirac, P. Zoller, R. Côté and M. D. Lukin, *Fast Quantum Gates for Neutral Atoms*, Physical Review Letters, **85**, 2208–2211 (2000).

[41] M. D. Lukin, M. Fleischhauer and R. Cote, *Dipole Blockade and Quantum Information Processing in Mesoscopic Atomic Ensembles*, Physical Review Letters, **87**, 037901 (2001).

[42] A. Gaëtan, Y. Miroshnychenko, T. Wilk, A. Chotia, M. Viteau, D. Comparat, P. Pillet, A. Browaeys and P. Grangier, *Observation of collective excitation of two individual atoms in the Rydberg blockade regime*, Nature Physics, **5**, 115–118 (2009).

[43] E. Urban, T. A. Johnson, T. Henage, L. Isenhower, D. D. Yavuz, T. G. Walker and M. Saffman, *Observation of Rydberg blockade between two atoms*, Nature Physics, **5**, 110–114 (2009).

[44] L. Isenhower, E. Urban, X. L. Zhang, A. T. Gill, T. Henage, T. A. Johnson, T. G. Walker and M. Saffman, *Demonstration of a Neutral Atom Controlled-NOT Quantum Gate*, Physical Review Letters, **104** (2010).

[45] S. Ospelkaus, K.-K. Ni, D. Wang, M. H. G. d. Miranda, B. Neyenhuis, G. Quemener, P. S. Julienne, J. L. Bohn, D. S. Jin and J. Ye, *Quantum-State Controlled Chemical Reactions of Ultracold Potassium-Rubidium Molecules*, Science, **327**, 853–857 (2010).

[46] S. Jochim, M. Bartenstein, A. Altmeyer, G. Hendl, S. Riedl, C. Chin, J. Hecker Denschlag and R. Grimm, *Bose-Einstein Condensation of Molecules*, Science, **302**, 2101–2103 (2003).

[47] M. Zwierlein, C. Stan, C. Schunck, S. Raupach, S. Gupta, Z. Hadzibabic and W. Ketterle, *Observation of Bose-Einstein Condensation of Molecules*, Physical Review Letters, **91**, 250401 (2003).

[48] T. Kraemer, M. Mark, P. Waldburger, J. G. Danzl, C. Chin, B. Engeser, A. D. Lange, K. Pilch, A. Jaakkola, H.-C. Nägerl and R. Grimm, *Evidence for Efimov quantum states in an ultracold gas of caesium atoms*, Nature, **440**, 315–318 (2006).

[49] V. Bendkowsky, B. Butscher, J. Nipper, J. P. Shaffer, R. Löw and T. Pfau, *Observation of ultralong-range Rydberg molecules*, Nature, **458**, 1005–1008 (2009).

[50] W. Li, T. Pohl, J. M. Rost, S. T. Rittenhouse, H. R. Sadeghpour, J. Nipper, B. Butscher, J. B. Balewski, V. Bendkowsky, R. Low and T. Pfau, *A Homonuclear Molecule with a Permanent Electric Dipole Moment*, Science, **334**, 1110–1114 (2011).

[51] T. Ritz, A. Damjanovic and K. Schulten, *The Quantum Physics of Photosynthesis*, Chem. Phys. Chem., **3**, 243–248 (2002).

[52] C. H. Bennett and G. Brassard, *Quantum cryptography: Public key distribution and coin tossing*, Theoretical Computer Science (2011).

[53] M. D. Eisaman, J. Fan, A. Migdall and S. V. Polyakov, *Invited Review Article: Single-photon sources and detectors*, Review of Scientific Instruments, **82**, 071101

(2011).

[54] M. Saffman and T. Walker, *Creating single-atom and single-photon sources from entangled atomic ensembles*, Physical Review A, **66**, 065403 (2002).

[55] F. Bariani, Y. Dudin, T. Kennedy and A. Kuzmich, *Dephasing of Multiparticle Rydberg Excitations for Fast Entanglement Generation*, Physical Review Letters, **108**, 030501 (2012).

[56] Y. O. Dudin and A. Kuzmich, *Strongly Interacting Rydberg Excitations of a Cold Atomic Gas*, Science (2012).

[57] T. D. Ladd, F. Jelezko, R. Laflamme, Y. Nakamura, C. Monroe and J. L. O'Brien, *Quantum computers*, Nature, **464**, 45–53 (2010).

[58] D. Loss and D. P. DiVincenzo, *Quantum computation with quantum dots*, Physical Review A, **57**, 120–126 (1998).

[59] A. Fioretti, D. Comparat, A. Crubellier, O. Dulieu, F. Masnou-Seeuws and P. Pillet, *Formation of Cold Cs2 Molecules through Photoassociation*, Physical Review Letters, **80**, 4402–4405 (1998).

[60] S. D. Hogan and F. Merkt, *A New Perspective on the Binding Power of an Electron*, ChemPhysChem, **10**, 2931–2934 (2009).

[61] C. Foot, *Atomic physics*, Oxford University Press, Oxford (2003).

[62] J. J. Sakurai, *Modern quantum mechanics*, Addison-Wesley Longman, Reading, rev. edition (2010).

[63] L. Allen and J. H. Eberly, *Optical resonance and two-level atoms*, Dover, New York (1987).

[64] F. Bloch, *Nuclear Induction*, Physical Review, **70**, 460–474 (1946).

[65] J.J. Balmer, *Notiz über die Spectrallinien des Wasserstoffs*, Annalen der Physik, **261**, 80–87 (1885).

[66] N. Bohr, *On the Constitution of Atoms and Molecules: Part I*, Philosophical Magazine, **26**, 1–25 (1913).

[67] J. Millen, G. Lochead, G. R. Corbett, R. M. Potvliege and M. P. A. Jones, *Spectroscopy of a cold strontium Rydberg gas*, Journal of Physics B: Atomic, Molecular and Optical Physics, **44**, 184001 (2011).

[68] M. J. Seaton, *Quantum defect theory*, Reports on Progress in Physics, **46**, 167–257 (1983).

[69] W. Li, I. Mourachko, M. Noel and T. Gallagher, *Millimeter-wave spectroscopy of cold Rb Rydberg atoms in a magneto-optical trap: Quantum defects of the ns, np,*

and nd series, Physical Review A, **67**, 052502 (2003).

[70] J. Han, Y. Jamil, D. Norum, P. Tanner and T. Gallagher, *Rb nf quantum defects from millimeter-wave spectroscopy of cold ^{85}Rb Rydberg atoms*, Physical Review A, **74**, 054502 (2006).

[71] K. Afrousheh, P. Bohlouli-Zanjani, J. Petrus and J. Martin, *Determination of the ^{85}Rb ng-series quantum defect by electric-field-induced resonant energy transfer between cold Rydberg atoms*, Physical Review A, **74**, 062712 (2006).

[72] M. Mack, F. Karlewski, H. Hattermann, S. Höckh, F. Jessen, D. Cano and J. Fortágh, *Measurement of absolute transition frequencies of ^{87}Rb to nS and nD Rydberg states by means of electromagnetically induced transparency*, Physical Review A, **83**, 052515 (2011).

[73] B. Butscher, *A Rydberg Interferometer: From coherent formation of ultralong-range Rydberg molecules to state tomography of Rydberg atoms*, Ph.D. thesis, Universität Stuttgart, Stuttgart (2011).

[74] M. L. Zimmerman, M. G. Littman, M. M. Kash and D. Kleppner, *Stark structure of the Rydberg states of alkali-metal atoms*, Physical Review A, **20**, 2251–2275 (1979).

[75] J. M. Blatt, *Practical points concerning the solution of the Schrödinger equation*, Journal of Computational Physics, **1**, 382–396 (1967).

[76] M. O'Sullivan and B. Stoicheff, *Scalar polarizabilities and avoided crossings of high Rydberg states in Rb*, Physical Review A, **31**, 2718–2720 (1985).

[77] M. O'Sullivan and B. Stoicheff, *Scalar and tensor polarizabilities of ^2D Rydberg states in Rb*, Physical Review A, **33**, 1640–1645 (1986).

[78] Daniel A. Steck, *Rubidium 87 d line data*, http://steck.us/alkalidata/ (2010).

[79] A. Reinhard, T. Liebisch, B. Knuffman and G. Raithel, *Level shifts of rubidium Rydberg states due to binary interactions*, Physical Review A, **75**, 032712 (2007).

[80] M. R. Flannery, D. Vrinceanu and V. N. Ostrovsky, *Long-range interaction between polar Rydberg atoms*, Journal of Physics B: Atomic, Molecular and Optical Physics, **38**, S279–S293 (2005).

[81] T. Vogt, M. Viteau, A. Chotia, J. Zhao, D. Comparat and P. Pillet, *Electric-Field Induced Dipole Blockade with Rydberg Atoms*, Physical Review Letters, **99**, 073002 (2007).

[82] P. Bohlouli-Zanjani, J. Petrus and J. Martin, *Enhancement of Rydberg Atom Interactions Using ac Stark Shifts*, Physical Review Letters, **98**, 203005 (2007).

[83] D. Comparat and P. Pillet, *Dipole blockade in a cold Rydberg atomic sample [Invited]*, Journal of the Optical Society of America B, **27**, A208–A232 (2010).

[84] J. D. Jackson, *Classical electrodynamics*, Wiley, New York, 3 edition (1999).

[85] F. Robicheaux and J. Hernández, *Many-body wave function in a dipole blockade configuration*, Physical Review A, **72**, 063403 (2005).

[86] D. Tong, S. M. Farooqi, J. Stanojevic, S. Krishnan, Y. P. Zhang, R. Côté, E. E. Eyler and P. L. Gould, *Local Blockade of Rydberg Excitation in an Ultracold Gas*, Physical Review Letters, **93**, 063001 (2004).

[87] S. Chandrasekhar, *Stochastic Problems in Physics and Astronomy*, Reviews of Modern Physics, **15**, 1–89 (1943).

[88] V. Vuletic, *Quantum networks: When superatoms talk photons*, Nature Physics, **2**, 801–802 (2006).

[89] R. Heidemann, U. Raitzsch, V. Bendkowsky, B. Butscher, R. Löw, L. Santos and T. Pfau, *Evidence for Coherent Collective Rydberg Excitation in the Strong Blockade Regime*, Physical Review Letters, **99**, 163601 (2007).

[90] T. Pohl and P. Berman, *Breaking the Dipole Blockade: Nearly Resonant Dipole Interactions in Few-Atom Systems*, Physical Review Letters, **102**, 013004 (2009).

[91] C. Greene, A. Dickinson and H. Sadeghpour, *Creation of Polar and Nonpolar Ultra-Long-Range Rydberg Molecules*, Physical Review Letters, **85**, 2458–2461 (2000).

[92] V. Bendkowsky, B. Butscher, J. Nipper, J. Balewski, J. Shaffer, R. Löw, T. Pfau, W. Li, J. Stanojevic, T. Pohl and J. Rost, *Rydberg Trimers and Excited Dimers Bound by Internal Quantum Reflection*, Physical Review Letters, **105**, 163201 (2010).

[93] B. Butscher, J. Nipper, J. B. Balewski, L. Kukota, V. Bendkowsky, R. Löw and T. Pfau, *Atom–molecule coherence for ultralong-range Rydberg dimers*, Nature Physics, **6**, 970–974 (2010).

[94] B. Butscher, V. Bendkowsky, J. Nipper, J. B. Balewski, L. Kukota, R. Löw, T. Pfau, W. Li, T. Pohl and J. M. Rost, *Lifetimes of ultralong-range Rydberg molecules in vibrational ground and excited states*, Journal of Physics B: Atomic, Molecular and Optical Physics, **44**, 184004 (2011).

[95] E. Fermi, *Sopra lo Spostamento per Pressione delle Righe Elevate delle Serie Spettrali*, Il Nuovo Cimento, **11**, 157–166 (1934).

[96] A. Omont, *On the theory of collisions of atoms in rydberg states with neutral particles*, Journal de Physique, **38**, 1343–1359 (1977).

[97] T. F. O'Malley, L. Spruch and L. Rosenberg, *Modification of Effective-Range Theory in the Presence of a Long-Range (r−4) Potential*, Journal of Mathematical Physics, **2**, 491 (1961).

[98] C. Bahrim and U. Thumm, *Low-lying $^3P^o$ and $^3S^e$ states of Rb^-, Cs^-, and Fr^-*, Physical Review A, **61**, 022722 (2000).

[99] A. Khuskivadze, M. Chibisov and I. Fabrikant, *Adiabatic energy levels and electric dipole moments of Rydberg states of Rb_2 and Cs_2 dimers*, Physical Review A, **66**, 042709 (2002).

[100] I. I. Fabrikant, *Interaction of Rydberg atoms and thermal electrons with K, Rb and Cs atoms*, Journal of Physics B: Atomic and Molecular Physics, **19**, 1527–1540 (1986).

[101] V. Bendkowsky, *Ultralong-range Rydberg molecules: Investigation of a novel binding*, Ph.D. thesis, Universität Stuttgart, Stuttgart (2010).

[102] E. L. Hamilton, C. H. Greene and H. R. Sadeghpour, *Shape-resonance-induced long-range molecular Rydberg states*, Journal of Physics B: Atomic, Molecular and Optical Physics, **35**, L199–L206 (2002).

[103] J. G. Danzl, E. Haller, M. Gustavsson, M. J. Mark, R. Hart, N. Bouloufa, O. Dulieu, H. Ritsch and H.-C. Nagerl, *Quantum Gas of Deeply Bound Ground State Molecules*, Science, **321**, 1062–1066 (2008).

[104] W. Klemperer, K. K. Lehmann, J. K. G. Watson and S. C. Wofsy, *Can molecules have permanent electric dipole moments?*, The Journal of Physical Chemistry, **97**, 2413–2416 (1993).

[105] H. W. Kroto, *Molecular rotation spectra*, Dover Publications, Mineola and N.Y (2003).

[106] W. Demtröder, *Molekülphysik: Theoretische Grundlagen und experimentelle Methoden*, Oldenbourg, München (2003).

[107] K.-K. Ni, S. Ospelkaus, M. H. G. d. Miranda, A. Pe'er, B. Neyenhuis, J. J. Zirbel, S. Kotochigova, P. S. Julienne, D. S. Jin and J. Ye, *A High Phase-Space-Density Gas of Polar Molecules*, Science, **322**, 231–235 (2008).

[108] J. Deiglmayr, A. Grochola, M. Repp, K. Mörtlbauer, C. Glück, J. Lange, O. Dulieu, R. Wester and M. Weidemüller, *Formation of Ultracold Polar Molecules in the Rovibrational Ground State*, Physical Review Letters, **101**, 133004 (2008).

[109] M. S. Schoffler, J. Titze, N. Petridis, T. Jahnke, K. Cole, L. P. H. Schmidt, A. Czasch, D. Akoury, O. Jagutzki, J. B. Williams, N. A. Cherepkov, S. K. Semenov, C. W. McCurdy, T. N. Rescigno, C. L. Cocke, T. Osipov, S. Lee, M. H. Prior,

A. Belkacem, A. L. Landers, H. Schmidt-Bocking, T. Weber and R. Dorner, *Ultrafast Probing of Core Hole Localization in N2*, Science, **320**, 920–923 (2008).

[110] R. Löw, *A versatile setup for experiments with Rubidium Bose Einstein condensates: From optical lattices to Rydberg matter*, Ph.D. thesis, Universität Stuttgart, Stuttgart (2006).

[111] R. Heidemann, *Rydberg excitation of Bose-Einstein condensates, coherent collective dynamics*, Ph.D. thesis, Universität Stuttgart, Stuttgart (2008).

[112] Ulrich Raitzsch, *Aufbau einer UHV-Kammer zur Durchführung von Experimenten mit Bose-Einstein-Kondensaten in optischen Gittern: Diploma*, Universität Stuttgart, Stuttgart (2006).

[113] W. Phillips and H. Metcalf, *Laser Deceleration of an Atomic Beam*, Physical Review Letters, **48**, 596–599 (1982).

[114] T. Walker, D. Sesko and C. Wieman, *Collective behavior of optically trapped neutral atoms*, Physical Review Letters, **64**, 408–411 (1990).

[115] W. Ketterle, K. Davis, M. Joffe, A. Martin and D. Pritchard, *High densities of cold atoms in a dark spontaneous-force optical trap*, Physical Review Letters, **70**, 2253–2256 (1993).

[116] M. Anderson, W. Petrich, J. Ensher and E. Cornell, *Reduction of light-assisted collisional loss rate from a low-pressure vapor-cell trap*, Physical Review A, **50**, R3597–R3600 (1994).

[117] D. Boiron, A. Michaud, P. Lemonde, Y. Castin, C. Salomon, S. Weyers, K. Szymaniec, L. Cognet and A. Clairon, *Laser cooling of cesium atoms in gray optical molasses down to 1.1 muK*, Physical Review A, **53**, R3734–R3737 (1996).

[118] M.-O. Mewes, M. Andrews, N. van Druten, D. Kurn, D. Durfee and W. Ketterle, *Bose-Einstein Condensation in a Tightly Confining dc Magnetic Trap*, Physical Review Letters, **77**, 416–419 (1996).

[119] W. Ketterle, D. Durfee and D. Stamper-Kurn, *Making, probing and understanding Bose-Einstein condensates*, arxiv, **9904034v2** (1999).

[120] C. Zener, *Non-Adiabatic Crossing of Energy Levels*, Proceedings of the Royal Society A: Mathematical, Physical and Engineering Sciences, **137**, 696–702 (1932).

[121] U. Krohn, *Universal scaling and coherence properties of an ultracold Rydberg gas*, Ph.D. thesis, Universität Stuttgart, Stuttgart (2011).

[122] J. Balewski, *Hochauflösende Photoassoziationsspektroskopie von Rydberg-Dimeren und Trimeren: Diplomarbeit*, Universität Stuttgart, Stuttgart (2009).

[123] R. Löw, H. Weimer, J. Nipper, J. B. Balewski, B. Butscher, H. P. Büchler and T. Pfau, *An experimental and theoretical guide to strongly interacting Rydberg gases*, Journal of Physics B: Atomic, Molecular and Optical Physics, **45**, 113001 (2012).

[124] D. P. DiVincenzo, *Quantum Computation*, Science, **270**, 255–261 (1995).

[125] H. Weimer, R. Löw, T. Pfau and H. P. Büchler, *Quantum Critical Behavior in Strongly Interacting Rydberg Gases*, Physical Review Letters, **101**, 250601 (2008).

[126] I. Beterov, I. Ryabtsev, D. Tretyakov and V. Entin, *Quasiclassical calculations of blackbody-radiation-induced depopulation rates and effective lifetimes of Rydberg nS, nP, and nD alkali-metal atoms with $n \leq 80$*, Physical Review A, **79**, 052504 (2009).

[127] K. C. Younge and G. Raithel, *Rotary echo tests of coherence in Rydberg-atom excitation*, New Journal of Physics, **11**, 043006 (2009).

[128] M. Reetz-Lamour, J. Deiglmayr, T. Amthor and M. Weidemüller, *Rabi oscillations between ground and Rydberg states and van der Waals blockade in a mesoscopic frozen Rydberg gas*, New Journal of Physics, **10**, 045026 (2008).

[129] T. Johnson, E. Urban, T. Henage, L. Isenhower, D. Yavuz, T. Walker and M. Saffman, *Rabi Oscillations between Ground and Rydberg States with Dipole-Dipole Atomic Interactions*, Physical Review Letters, **100**, 113003 (2008).

[130] N. Ramsey, *A Molecular Beam Resonance Method with Separated Oscillating Fields*, Physical Review, **78**, 695–699 (1950).

[131] M. Saffman, X. L. Zhang, A. T. Gill, L. Isenhower and T. G. Walker, *Rydberg state mediated quantum gates and entanglement of pairs of neutral atoms*, Journal of Physics: Conference Series, **264**, 012023 (2011).

[132] I. I. Ryabtsev, D. B. Tretyakov and I. I. Beterov, *Stark-switching technique for fast quantum gates in Rydberg atoms*, Journal of Physics B: Atomic, Molecular and Optical Physics, **36**, 297–306 (2003).

[133] A. D. Cronin, J. Schmiedmayer and D. E. Pritchard, *Optics and interferometry with atoms and molecules*, Reviews of Modern Physics, **81**, 1051–1129 (2009).

[134] B. Butscher, *Kollektive kohaerente Anregung von ultrakalten Rydberg-Atomen*, Universität Stuttgart, Stuttgart (2007).

[135] I. Ryabtsev, D. Tretyakov, I. Beterov, V. Entin and E. Yakshina, *Stark-tuned Förster resonance and dipole blockade for two to five cold Rydberg atoms: Monte Carlo simulations for various spatial configurations*, Physical Review A, **82**, 053409 (2010).

[136] J. Gurian, P. Cheinet, P. Huillery, A. Fioretti, J. Zhao, P. Gould, D. Comparat and P. Pillet, *Observation of a Resonant Four-Body Interaction in Cold Cesium Rydberg Atoms*, Physical Review Letters, **108**, 023005 (2012).

[137] K. Younge, A. Reinhard, T. Pohl, P. Berman and G. Raithel, *Mesoscopic Rydberg ensembles: Beyond the pairwise-interaction approximation*, Physical Review A, **79**, 043420 (2009).

[138] L. Isenhower, W. Williams, A. Dally and M. Saffman, *Atom trapping in an interferometrically generated bottle beam trap*, Optics Letters, **34**, 1159 (2009).

[139] M. Saffman and T. Walker, *Analysis of a quantum logic device based on dipole-dipole interactions of optically trapped Rydberg atoms*, Physical Review A, **72**, 022347 (2005).

[140] R. M. W. van Bijnen, S. Smit, K. A. H. van Leeuwen, E. J. D. Vredenbregt and S. J. J. M. F. Kokkelmans, *Adiabatic formation of Rydberg crystals with chirped laser pulses*, Journal of Physics B: Atomic, Molecular and Optical Physics, **44**, 184008 (2011).

[141] T. Pohl, E. Demler and M. D. Lukin, *Dynamical Crystallization in the Dipole Blockade of Ultracold Atoms*, Physical Review Letters, **104**, 043002 (2010).

[142] T. Carroll, K. Claringbould, A. Goodsell, M. Lim and M. Noel, *Angular Dependence of the Dipole-Dipole Interaction in a Nearly One-Dimensional Sample of Rydberg Atoms*, Physical Review Letters, **93**, 153001 (2004).

[143] J. Johnson and S. Rolston, *Interactions between Rydberg-dressed atoms*, Physical Review A, **82**, 033412 (2010).

[144] J. Honer, H. Weimer, T. Pfau and H. Büchler, *Collective Many-Body Interaction in Rydberg Dressed Atoms*, Physical Review Letters, **105**, 160404 (2010).

[145] M. Mayle, I. Lesanovsky and P. Schmelcher, *Dressing of ultracold atoms by their Rydberg states in a Ioffe–Pritchard trap*, Journal of Physics B: Atomic, Molecular and Optical Physics, **43**, 155003 (2010).

[146] G. Pupillo, A. Micheli, M. Boninsegni, I. Lesanovsky and P. Zoller, *Strongly Correlated Gases of Rydberg-Dressed Atoms: Quantum and Classical Dynamics*, Physical Review Letters, **104**, 223002 (2010).

[147] F. Maucher, N. Henkel, M. Saffman, W. Królikowski, S. Skupin and T. Pohl, *Rydberg-Induced Solitons: Three-Dimensional Self-Trapping of Matter Waves*, Physical Review Letters, **106**, 170401 (2011).

[148] N. Henkel, R. Nath and T. Pohl, *Three-Dimensional Roton Excitations and Supersolid Formation in Rydberg-Excited Bose-Einstein Condensates*, Physical Review

Letters, **104**, 195302 (2010).

[149] S. Wüster, C. Ates, A. Eisfeld and J. Rost, *Newton's Cradle and Entanglement Transport in a Flexible Rydberg Chain*, Physical Review Letters, **105**, 053004 (2010).

[150] Ludmila Kukota, *Zeemanlinien und kohärentes Verhalten der Rydberg-Moleküle*, Universität Stuttgart, Stuttgart (2012).

[151] Seth Rittenhouse, *Private Communication* (05.04.2011).

Danksagung

Zum Abschluss möchte ich all jenen danken, ohne deren Beitrag diese Arbeit nicht möglich gewesen wäre. Allen voran Professor Tilman Pfau, nicht nur für die umfangreiche finanzielle Ausstattung und die wissenschaftlichen Ideen, sondern vor allem für die Leitung der Arbeitsgruppe in einer Art und Weise die sowohl konzentrierte, zielorientierte wissenschaftliche Arbeit ermöglichte, als auch ein freundliches Arbeitsumfeld in einem sympathischen Team bot.
Ich habe die Arbeit an meiner Promotion sehr genossen, woran das Team an unserem Experiment, Vera, Björn, Jonathan, Alexander und Robert, einen entscheidenden Anteil hatte. Björn und Vera, von euch habe ich als Frischling fachlich viel gelernt und profitiert. Ihr habt das Experiment auf die Überholspur gelenkt und in einem vielversprechenden Zustand an mich weitergegeben. Ich möchte euch auch danken dass ihr durch eure gemeinsame Entwicklung frischen Wind in die trockene Wissenschaft brachtet!
Ein sehr großer Dank gebührt Jonathan. Ich habe Dich als perfekten Kollegen kennengelernt und ich glaube wir wissen beide, dass Dein Beitrag, sowohl experimentell als auch in unseren Diskussionen, nicht unterschätzt werden kann. Ohne Dich wäre das Experiment nicht so erfolgreich. Ich hoffe das Biest, das sich Experiment schimpft, lässt sich auch von Dir melken und ich wünsche Dir dass ich recht behalte was die Zukunft angeht!
Robert, du hattest immer ein offenes Ohr für Probleme und Fragen. Ich weiß es zu schätzen dass ich auch mit den dummen Fragen zu Dir kommen konnte, ohne dass du mich ausgelacht hast.
Vielen Dank für Deine Hilfe, Alexander, ich hoffe das Experiment wird sich auch in Zukunft erfolgreich weiterentwickeln.
Sebastian, auch wenn du erst gegen Ende meiner Promotion dazugestoßen bist, so habe ich die Diskussionen mit Dir gerne gesucht und geführt. Du hast eindeutig neue Impulse durch andere Sichtweisen gegeben und neuen Spaß an der Wissenschaft geweckt. Vermutlich werde ich ewig überlegen, ob Dein Angebot nicht die bessere Wahl gewesen wäre!
Außerhalb des direkten Teams um unser Experiment möchte ich der gesamten Arbeitsgruppe des PI5, inklusive der geduldigen Administration, danken. Das positive, menschliche Umfeld ist sicherlich eines der Aushängeschilder des PI5 und entscheidend für

den Wohlfühlfaktor. Danke euch allen!
Außerdem möchte ich Professor Wrachtrup für die Korrektur der Arbeit und Professor Wunner für die Übernahme des Prüfungsvorsitzes danken.
Nicht vergessen möchte ich auch den Beitrag meiner Familie. Vera, ohne Dich wären wir nie in Stuttgart gelandet, auch Dir habe ich diese Zeit zu verdanken. Vielen Dank für deine Unterstützung und dein Verständnis.
Vielen Dank auch an meine Eltern und Emanuel. Ohne euch hätte ich den Weg bis hierher niemals geschafft, euch habe ich zu verdanken dass ich all jenen danken kann, denen ich bereits gedankt habe!